

IMPROVED QUANTITATIVE METHODS FOR MULTIPLE  
NEUROPHARMACOLOGICAL NON-INVASIVE BRAIN PET STUDIES

by

Aniket Joshi

A dissertation submitted in partial fulfillment  
of the requirements for the degree of  
Doctor of Philosophy  
(Biomedical Engineering)  
in The University of Michigan  
2008

Doctoral Committee:

Professor Robert A. Koeppe, Co-Chair  
Professor Jeffrey A. Fessler, Co-Chair  
Professor Charles R. Meyer  
Professor Douglas C. Noll  
Senior Research Scientist Neal H. Clinthorne

© Aniket Joshi

---

2008

## Table of Contents

Acknowledgements.....	iii
List of Figures.....	vii
List of Tables.....	ix
Abstract.....	x
Chapter 1 Introduction.....	1
1.1 Motivation.....	2
1.2 Thesis outline and Contribution.....	3
1.2.1 Logan plot-bias reduction using Principal Component Analysis .....	4
1.2.2 Multiple Neuropharmacological Measures from a single PET scan .....	4
1.2.2.1 Dual-measurement intervention studies.....	5
1.2.2.2 Dual-tracer studies .....	5
1.2.3 Reduction of inter-scanner PET image variability.....	6
Chapter 2 Theoretical background of tracer kinetic modeling in PET.....	7
2.1 Steps in dynamic PET imaging.....	7
2.2 PET radiotracer .....	10
2.3 Two tissue compartmental model.....	11
2.4 Reference region models.....	15
2.4.1 Two compartment ‘full reference tissue model’ (RTM).....	16
2.4.2 Simplified reference tissue model (sRTM).....	17
2.4.3 Reference region-based Logan plots.....	18
Chapter 3 Improving PET receptor binding estimates from Logan plots using principal component analysis.....	21
3.1 The cause of bias in Logan plots.....	22
3.2 Existing bias removal techniques.....	22

3.3 Principal Component Analysis (PCA) for Logan-plot bias reduction .....	23
3.4 Simulations .....	25
3.4.1 Simulation Design.....	25
3.4.2 Simulation Results .....	28
3.5 Human Studies:.....	36
3.5.1 Human Studies design.....	36
3.5.2 Human Studies Results .....	37
3.6 Discussion and Conclusion .....	38
Chapter 4 Dual-measurement Intervention Studies .....	41
4.1 Simulation studies.....	42
4.1.1 Simulation studies: Design .....	42
4.1.2 Simulation studies: Results .....	43
4.2 Human data studies.....	44
4.2.1 Human studies: Design .....	44
4.2.2 Human data: Results .....	45
4.3 Discussion and Conclusion.....	47
Chapter 5 Dual-Tracer Studies: Theory and Simulations .....	49
5.1 Theory of analysis techniques for non-invasive dual-tracer studies.....	50
5.1.1 Extrapolation Method (EM).....	52
5.1.2 Simultaneous Fitting Method (SM) .....	53
5.1.3 Using an irreversible tracer as Tracer <i>II</i> .....	54
5.2 Simulation Design.....	56
5.2.1 [ <sup>11</sup> C]FMZ - [ <sup>11</sup> C]DTBZ dual-tracer simulations.....	56
5.2.2 Simulations of assumption failures .....	58
5.2.3 [ <sup>11</sup> C]FMZ - [ <sup>11</sup> C]PMP dual-tracer simulations: .....	59
5.3 Results.....	61
5.3.1 [ <sup>11</sup> C]FMZ - [ <sup>11</sup> C]DTBZ dual-tracer simulations.....	61
5.3.2 Effects of failure of assumptions .....	64
5.3.3 [ <sup>11</sup> C]FMZ - [ <sup>11</sup> C]PMP dual-tracer simulations: .....	64

5.4 Discussion and Conclusion .....	66
Chapter 6 Dual-tracer studies: Human Studies .....	69
6.1 Radiotracers .....	70
6.2 Validation of the key assumption: .....	73
6.3 Data acquisition, reconstruction, and processing:.....	73
6.4 Robust parameter estimation.....	76
6.4.1 Adaptive smoothing .....	76
6.4.2 Population average $k_4$ in the full reference tissue model .....	77
6.4.3 Signal separation followed by estimation of binding measures.....	77
6.5 Results.....	78
6.5.1 [ $^{11}\text{C}$ ]FMZ - [ $^{11}\text{C}$ ]DTBZ studies .....	79
6.5.2 [ $^{11}\text{C}$ ]DTBZ - [ $^{11}\text{C}$ ]FMZ studies .....	82
6.5.3 [ $^{11}\text{C}$ ]FMZ - [ $^{11}\text{C}$ ]PMP studies.....	82
6.6 Discussion and Conclusion .....	83
Chapter 7 Reducing inter-scanner PET image variability .....	87
7.1 Multi-center Hoffman brain phantom scan protocol .....	89
7.2 Theory of high and low frequency corrections .....	90
7.2.1 High frequency correction .....	90
7.2.2 Low frequency correction .....	92
7.3 High frequency correction factors from phantom scans .....	93
7.4 Assessment of the validity of low frequency correction factors using simulations:94	
7.5 Application of correction factors to phantom and human image data .....	97
7.5.1 Phantom scans.....	97
7.5.2 Human scans (Control subjects) .....	99
7.6 Discussion and Conclusion .....	100
Chapter 8 Summary and Future directions .....	101
8.1 Summary of results achieved .....	102
8.2 Future directions .....	103

8.2.1 Noninvasive studies in the absence of a reference region .....	103
8.2.2 Weighted PCA for bias reduction in Logan plots.....	104
8.2.3 Improved weighting for reference region approaches .....	104
8.2.4 Further improvement of dual-tracer studies.....	105
8.2.5 Improvements in low frequency correction for inter-scanner variability reduction .....	106
References.....	108

## List of Figures

Figure 2.1 Steps in a dynamic PET imaging experiment.....	7
Figure 2.2 Authentic radiotracer blood curve from a 60 min single tracer [ <sup>11</sup> C]FMZ study .....	8
Figure 2.3: Dynamic sequence of a slice of a [ <sup>11</sup> C]FMZ study .....	9
Figure 2.4: [ <sup>11</sup> C]FMZ time-activity curves (TACs).....	9
Figure 2.5 Various possible states of [ <sup>11</sup> C]FMZ tracer molecules (dark blue): blood plasma (red), interstitial space (grey), benzodiazepine receptors on the post-synaptic side (light blue). The synaptic terminals are shown in yellow. Some other possible targets for a radiotracer are pre-synaptic binding sites (green) or pre-synaptic storage vesicles (brown). .....	11
Figure 2.6 Two tissue compartmental model.....	11
Figure 2.7 Compartmental model for reference region approaches .....	16
Figure 2.8: Logan plots for occipital cortex (DVR = 4.3), thalamus (DVR=2.6) and pons (DVR=1.0). .....	19
Figure 2.9 $R_l$ and DVR images from dynamic [ <sup>11</sup> C]FMZ. ....	19
Figure 3.1: Noiseless time activity curves (TACs) for simulated test data. ....	26
Figure 3.2: Mean vector and first 3 principal components for carfentanil-like tracer simulation studies.....	29
Figure 3.3: Box plot comparisons of DVR estimates obtained with an increasing number of principal components in single measurement simulation studies (True DVR=5).. .....	29
Figure 3.4: The mean of percent-normalized residuals between the PCA1-based curve approximations and the true tissue curves in single measurement simulation studies.. .....	30
Figure 3.5: Comparison of distribution of the DVR values estimated by each of the existing methods vs. PCA1 in single measurement simulation studies for true DVR=5.....	32
Figure 3.6: Trade-off between bias and precision for the existing and proposed bias removal methods in single measurement simulation studies.....	33
Figure 3.7: Box plot comparisons of the DVR estimates obtained using the existing bias removal methods and the proposed bias removal method for single measurement simulation studies (true DVR = 5).....	34
Figure 3.8: Box plot comparisons of the DVR estimates obtained using the existing and proposed bias removal methods for single measurement studies simulated to include a blood volume component, but analyzed ignoring the vascular contribution (true DVR=5). .....	35
Figure 4.1: Dual-measurement approach to measure the <i>in vivo</i> distribution of the radiotracer before and after perturbation of the system in a single tracer PET study. ....	41

Figure 4.2: Trade-off between bias and precision for the existing and proposed bias in simulated intervention studies.....	44
Figure 4.3: DVR images from a representative control subject estimated from data before and after 40 minutes with no intervention. ....	46
Figure 4.4: DVR images from a representative subject from scan data before and after injecting naloxone.....	46
Figure 5.1: Two tissue compartmental model for a non-invasive dual-tracer study of two reversible radiotracers.....	51
Figure 5.2: Noiseless TACs for the six simulated regions for the case where two reversible tracers mimicking [ <sup>11</sup> C]FMZ (Tracer <i>I</i> ) and [ <sup>11</sup> C]DTBZ (Tracer <i>II</i> ) are injected 20 minutes apart. ....	58
Figure 5.3: Noiseless TACs for the six simulated regions for the case where tracers mimicking reversible tracer [ <sup>11</sup> C]FMZ (Tracer <i>I</i> ) and irreversible tracer [ <sup>11</sup> C]PMP (Tracer <i>II</i> ) are injected 20 minutes apart.....	60
Figure 6.1: Dynamic dual-tracer PET image sequence for [ <sup>11</sup> C]FMZ - [ <sup>11</sup> C]DTBZ study with a 20 minute offset.. ....	71
Figure 6.2: Average dual-tracer curves for four regions from the study in Figure 6.1.....	72
Figure 6.3: Average time-activity curve (TAC) for pons, the reference tissue for [ <sup>11</sup> C]FMZ, from seven subjects that underwent a 60 min single-tracer [ <sup>11</sup> C]FMZ scan. ....	72
Figure 6.4: Parametric images obtained from a [ <sup>11</sup> C]FMZ - [ <sup>11</sup> C]DTBZ study at six brain levels. The parametric images shown are $R_I$ , equal to the ratio $K_1 / K_1^{ref}$ (rows 1 and 3), and the distribution volume ratio ( $DVR=1+BP_{ND}$ ) (rows 2 and 4) for both tracers. ....	78
Figure 6.6: Comparison of inter-subject means and standard deviations in parametric estimates obtained from single-tracer (ST) and dual-tracer studies analyzed using extrapolation method (EM) and simultaneous fitting method (SM).....	81
Figure 7.1: Low frequency correction factors for simulations with residual attenuation error alone. ....	95
Figure 7.2: Low frequency correction factors for simulations with residual scatter error alone.....	96
Figure 7.3: Low frequency correction factors for simulations with both residual scatter and attenuation errors.....	97
Figure 7.4: Application of the correction factors derived from phantom data to phantom data itself.....	99
Figure 7.5 Application of the correction factors derived from the phantom data to human normal scans.....	99



## List of Tables

Table 3.1: Kinetic parameters ranges for [ <sup>11</sup> C]carfentanil simulations .....	26
Table 3.2: Bias, given as percent of true value, and standard deviation in units of percent of true value (n = 1024). .....	35
Table 3.3: Mean DVR (mean standard deviation) in subjects imaged with the single measurement protocol (n = 12). .....	37
Table 4.1: Mean correlation coefficient and mean slope and mean intercept of the scatter plots of the early and late $BP_{ND}$ estimates in control subjects (n=4) with no intervention and in subjects with naloxone intervention (n=4). .....	47
Table 5.1: Kinetic parameters used for simulation of 6 hypothetical regions in a dual-tracer study with [ <sup>11</sup> C]FMZ-like and [ <sup>11</sup> C]DTBZ-like reversible tracers. ....	57
Table 5.2: Kinetic parameters used for simulation of 6 hypothetical regions in a dual-tracer study with [ <sup>11</sup> C]FMZ-like (reversible) and [ <sup>11</sup> C]PMP-like (irreversible) tracers. ....	59
Table 5.3: Bias and standard deviation in DVR estimates and mean % error in separated TACs for [ <sup>11</sup> C]FMZ-[ <sup>11</sup> C]DTBZ dual-tracer simulations.....	61
Table 5.4: Bias and standard deviation in parameter estimates and mean % error in separated TACs for [ <sup>11</sup> C]FMZ-[ <sup>11</sup> C]PMP dual-tracer simulations.....	65
Table 6.1: Imaging protocol details for dual-tracer studies. ....	74
Table 7.1 : Scanner models and the FWHM (in mm) of the smoothing kernels to attain a resolution of 8 mm FWHM (in-plane and axial). .....	93

## Abstract

Positron Emission Tomography (PET) is a medical imaging modality offering a powerful tool for brain research, brain ailment diagnosis and drug development. Brain-PET enables mapping of *in vivo* neurobiological functions such as blood flow, metabolism, enzyme activity, neuroreceptor binding site density and occupancy.

Quantification in brain-PET can broadly be classified into: 1) the accurate quantification of radiotracer distribution such that image values are proportional to the radiotracer concentration in tissue, and 2) the accurate quantification of the pharmacological state of the system-of-interest. This thesis addresses both of these aspects for functional neuroreceptor imaging studies of the living brain.

Traditional brain PET studies have at least two primary limitations. First, they measure only a *single* neuropharmacological aspect in isolation, which is often insufficient for characterizing a neurological condition. Second, data acquisition is accompanied by arterial blood sampling for measuring the input function to the system-of-interest, which is invasive for the subjects. The motivation for this thesis was to address both of these limitations and has led to the development of quantitative methods for *multiple* neuropharmacological PET studies performed *without* blood sampling. One such experimental design investigated was a dual-measurement intervention study where the system-of-interest is perturbed during data acquisition with the intent of changing the subject's pharmacological status and system parameters are estimated both pre- and post-intervention. Second was a dual-tracer study where two radiotracers targeting two different neuropharmacological systems were injected closely in time in the same study.

A major challenge in the data analysis of the multiple pharmacological PET studies is the statistical noise induced bias and variance in the parameter estimates. In this thesis, methods have been developed for improving accuracy of the neuropharmacological estimates reducing bias without a corresponding decrease in precision.

The thesis also addresses the issue of inter-scanner PET image variability, a major confound in multi-center studies used to investigate disease progression and in drug trials. Since various PET centers have different scanner models with different hardware and software; systematic differences exist in multi-center data. This thesis develops a framework to reduce the inter-scanner PET image variability before multi-center data is pooled for analysis.

# Chapter 1

## Introduction

Positron Emission Tomography (PET) is a medical imaging modality that offers a powerful tool for brain research as well as for clinical diagnosis of various brain ailments. Brain-PET enables the mapping of *in vivo* neurobiological functions such as blood flow, metabolism, enzyme activity, neuroreceptor binding site density or occupancy. A typical PET study involves the injection of a radiotracer (a compound labeled with a radionuclide) into the venous blood stream of a subject with the intention of studying a particular organ or biological system. In the case of brain studies, after crossing the blood brain barrier, the radiotracer might bind to neuroreceptors or transporter vesicles, or be metabolized by endogenous enzymes. An inert tracer, on the other hand, would diffuse across the blood brain barrier, free to move in and out of the brain but would not be bound or trapped. Happening in parallel to these biochemical processes, is the physical process of radioactive decay of the radioisotope. The decay of each radionucleus generates a positron which annihilates to emit diametrically opposed photons. The photons emitted from the subject are detected by the PET scanner. This emission data obtained over the duration of the scan is used to reconstruct images of the radiotracer distribution in the tissue of interest. By appropriate algorithms, including corrections for physical phenomenon such as scatter and attenuation, *quantitatively accurate* radiotracer distribution in tissue can be obtained.

Quantification of the biochemical process of interest targeted by the radiotracer is possible by analyzing the PET emission data as a function of time. PET emission data is binned into various time frames and reconstructed to obtain dynamic PET image data which represents the radiotracer distribution in tissue at specific time points throughout

the study. This temporal evolution of radiotracer concentration in individual voxels or regions of the image volume is called a time-activity curve (TAC). These TACs are useful in quantifying the physiological (e.g. blood flow) and/or pharmacological aspect (e.g. receptor binding site density, enzyme activity) of the system of interest.

Thus, quantification in dynamic PET studies can be classified into two categories: first is accurate quantification of the radiotracer distribution such that image values are proportional to the radiotracer concentration in tissue. The second aspect is the accurate quantification of the particular pharmacological or physiological aspect of the system being studied. This thesis addresses both of these aspects of PET quantification with particular application to functional neuroreceptor imaging studies of the living human brain.

## **1.1 Motivation**

Traditionally, brain PET studies have involved measurement of only a *single* neuropharmacological aspect in isolation following injection of single radiotracer. For quantification of the pharmacological parameters, dynamic PET data acquisition typically needs to be accompanied by arterial blood sampling from the subject that acts as an input function to the system of interest. This traditional approach has certain limitations. First, in some cases, investigation of only a single neuropharmacological system in isolation may be insufficient for the characterization of a subject's neurological condition. Second, measurement of the radiotracer input by drawing arterial blood samples is invasive for subjects and requires substantial work for the PET personnel. In addition, errors in arterial sampling may cause errors in quantification of the pharmacology being studied. The motivation for this thesis is to address both these limitations of traditional PET studies and has led to the development of improved methods for *multiple* pharmacological measurements from a single PET acquisition *without* blood sampling.

A major challenge in the data analysis of multiple pharmacological PET studies is the noise induced bias, or variance, or both in the parameter estimates. Noise in the TACs is primarily due to counting statistics. This noise affects parameter estimation in single-

tracer studies as well, but the effect is accentuated in multiple pharmacological studies. This problem has also been addressed in this thesis and methods have been developed for improving accuracy of the estimates where bias in estimates is reduced without an appreciable increase in variance.

Finally, the thesis addresses the specific issue of inter-scanner variability, which is a major impediment in multi-center trials. Recently there have been increasing efforts in the PET research community and the pharmaceutical industry to perform multi-center PET studies in large cohorts of subjects to investigate disease progression where data from various centers must be pooled together for analysis. Since the various PET centers have different scanner models from different vendors, each having different hardware and software, systematic differences are present in multi-center data. As a part of this doctoral work, a framework to reduce inter-scanner PET image variability in multi-center data has been developed and tested.

## 1.2 Thesis outline and Contribution

Chapter 2 of the thesis gives an overview of kinetic modeling methodology used to extract pharmacological parameters from dynamic PET studies. Principal component analysis-based approach for reducing noise-induced bias in Logan analysis for neuroreceptor density estimation is discussed in Chapter 3<sup>a</sup>. The primary thesis goal of noninvasive quantification of multiple neuropharmacological parameters is presented in Chapters 4<sup>a</sup>, 5<sup>b</sup> and 6<sup>b</sup>. Chapter 7<sup>c</sup> discusses methods to reduce inter-scanner PET image variability. Chapter 8 presents the summary of the results and lists future directions for the extension of the work in the thesis.

A brief description of the specific projects in this doctoral work is described next.

---

<sup>a</sup> This work has been published in the *Journal of Cereb Blood Flow and Metab* (April 2008)

<sup>b</sup> This work has been submitted to the *Journal of Cereb Blood Flow and Metab* (August 2008)

<sup>c</sup> This work is to be submitted to *Neuroimage* (September 2008)

### **1.2.1 Logan plot-bias reduction using Principal Component Analysis**

Logan plot methodology (see Section 2.4.3) for the estimation of the distribution volume ratio (DVR), an index of neuroreceptor binding site density, has become a standard in the field of brain PET imaging (Logan et al. 1996). Logan analysis is a simple linear method that gives robust DVR estimates. However, Logan plot-based DVR estimates are negatively biased due to the inherent noise in the PET time-activity curves (Slifstein and Laruelle 2000). Many methods to reduce the bias in Logan-based DVR estimation have been proposed for arterial sampling approach and for the first time have been applied for reference region approach in this work. These methods reduce only part of the bias or reduce bias at the expense of precision, or both. In this work, we developed a novel principal component analysis (PCA) method for reducing the Logan plot bias using without increasing the variance of the DVR estimates (Joshi et al. 2008a). The PCA-based linear model was obtained from the PET data itself. This new data-driven methodology for noise reduction in PET TACs also has application in multiple neuropharmacological PET studies described next.

### **1.2.2 Multiple Neuropharmacological Measures from a single PET scan**

The predominant portion of this thesis discusses methods developed for studying multiple neuropharmacological aspects of a subject in a single PET session without arterial sampling. Two experimental designs for obtaining multiple neuropharmacological measurements used in this work are as follows:

The first involves obtaining two measurements of the same pharmacological parameter from a single-tracer PET study where a tracer is administered, and at a given point during the acquisition a pharmacological intervention is given to perturb the system. Two separate DVR measures were obtained before and after intervention using PCA-based Logan plots.

The second multiple measurement method involves a dual-tracer experimental design, where two different radiotracers are injected closely in time in the same PET acquisition. Such a design aims to assess two different aspects of a subject's

neuropharmacological status and has the potential of better characterizing a subject's neurological condition than when using only a single radiotracer.

### **1.2.2.1 Dual-measurement intervention studies**

A standard brain PET challenge study involves two PET scans: one for a baseline measurement and one after the pharmacological or behavioral challenge. In single-scan intervention studies (or dual-measurement intervention studies as we will refer to them) described here, a tracer is administered and at some point during the PET acquisition an interventional challenge or perturbation of the system is made with the intent of changing biochemical or pharmacological status of the subject and hence the *in vivo* distribution of the radiotracer. Two distribution volume ratio (DVR) measurements are made using Logan plots once before and once after intervention. The bias and variance concerns in DVR estimation mentioned in subsection 1.2.1 are more pronounced in such studies because less data are available for parameter estimation using Logan plots compared to a single measurement case. The PCA-based Logan analysis method (Joshi et al. 2008a) was applied to reduce the bias in DVR estimates from dual-measurement intervention studies, and was compared to existing bias-reduction methods.

### **1.2.2.2 Dual-tracer studies**

Dual-tracer PET methodology provides an opportunity to characterize two different neuropharmacological aspects of a subject from a single PET acquisition. In these studies, two tracers are injected closely in time within a single PET scan with the intention of measuring two systems of interest nearly simultaneously.

Dual-tracer PET data analysis presents a formidable challenge as all positron emitting isotopes used to label PET radiotracers emit photons with 511 KeV energy and thus it is not possible to separate the signals from the two tracers using differing energy windows. Injecting two tracers simultaneously would make it impossible to separate the



two signals; hence the tracer injections in this work were staggered in time by 20 to 30 min.

The first results of dynamic dual-tracer brain PET studies in humans using  $^{11}\text{C}$  labeled tracers were reported here at the University of Michigan (Koeppel et al. 2001). These studies, however, used the arterial sampling approach. In this thesis, we extend this original work and report both simulation and human scan results of a non-invasive, dual-tracer PET approach where arterial sampling is not required (Joshi et al. 2008b; Joshi et al. 2008c).

### **1.2.3 Reduction of inter-scanner PET image variability**

This work is part of the multi-center Alzheimer's Disease Neuroimaging Initiative (ADNI) project, a longitudinal multi-site observational study of healthy controls, subjects with mild cognitive impairment (MCI), and mild Alzheimer's disease patients (Mueller et al. 2005). The project involves ~50 PET centers where [ $^{18}\text{F}$ ]fluorodeoxyglucose (FDG) PET scans have been obtained on more than 400 individuals. In spite of the standardization of the imaging protocol, systematic inter-scanner PET image differences have been observed due to differences in scanner resolution, reconstruction techniques, and different implementations of scatter and attenuation corrections on the different scanner models. Before the data from these centers is pooled together for analysis, it is important to account for the differences between the scanners. In this work we developed methods to reduce these differences using Hoffman brain phantom data acquired from the participating sites. Correction methodology was developed by comparing Hoffman brain phantom scans to a digital Hoffman phantom (i.e., the true radioactivity distribution) and was applied to both phantom data and human scans of normal subjects (Joshi et al. 2008d).

## Chapter 2

# Theoretical background of tracer kinetic modeling in PET

### 2.1 Steps in dynamic PET imaging

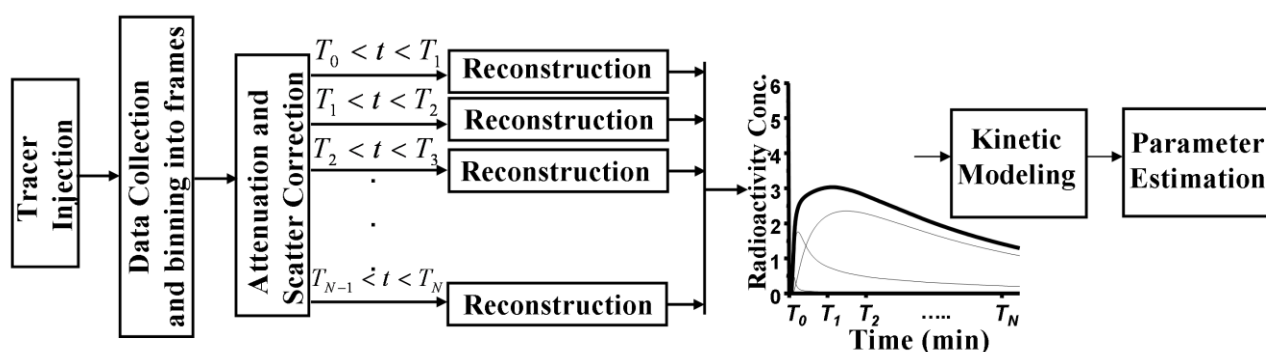
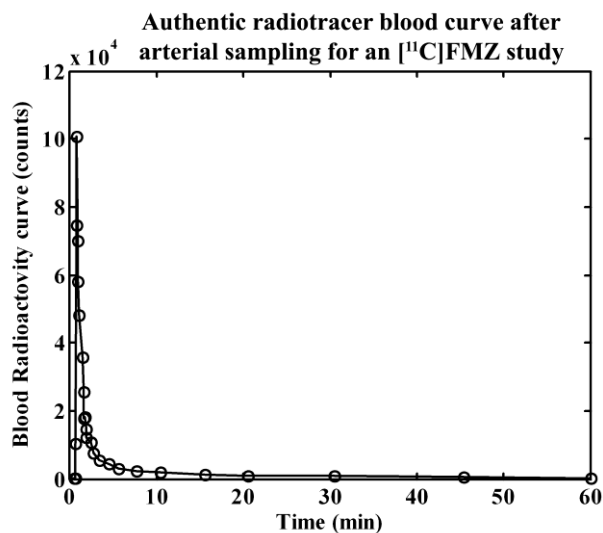


Figure 2.1 Steps in a dynamic PET imaging experiment

Figure 2.1 shows the various steps involved in a typical dynamic brain PET study. The first step is the injection of a short-lived radiotracer (a radiolabeled compound) into the venous blood stream of the subject. The tracer is delivered to the brain by the arterial flow where the tracer molecules may cross the blood-brain barrier and enter the tissue. Tracers may reversibly or irreversibly bind to receptor binding sites or may get metabolized by the enzymes in the brain. While the tracer molecule attains its biochemical fate, the radioisotope label may decay, emitting a positron that then annihilates to emit diametrically opposed 511 KeV photons. Some of the emitted photons are then collected by the detectors of a PET scanner. The photon events collected by detectors within a set timing window (6 ns – 10 ns) acquired over the duration of the scan (usually 1-2 hours) are binned into different time frames and corrected for physical effects such as attenuation and scatter. The corrected data for each time frame are

reconstructed using an analytical or iterative reconstruction algorithm to obtain an image of the radiotracer distribution in the brain over various time intervals. The radioactivity concentration in the image voxels or “targeted” region-of-interest can be traced as a function of time to obtain time-activity curves (TACs) of the tracer in the brain. In general, arterial blood sampling is also performed during data collection and the radioactivity concentration in the arterial plasma is considered as input to the system. The blood samples are obtained through an arterial puncture and are corrected for any radiotracer molecules that might have undergone metabolism (e.g., by enzymes in the plasma or the liver) to obtain an authentic radiotracer curve. Figure 2.2 shows the authentic radiotracer blood curve from a one hour study of  $^{11}\text{C}$  labeled flumazenil (abbreviated as  $^{11}\text{C}$ FMZ<sup>d</sup>). The pharmacological parameters of interest are estimated by appropriate kinetic modeling of the TACs (see Section 2.1).



**Figure 2.2** Authentic radiotracer blood curve from a 60 min single tracer  $^{11}\text{C}$ FMZ study

Figure 2.3 shows the radiotracer distribution in one brain slice from a 60 min  $^{11}\text{C}$ FMZ PET study. The data collected was binned into 15 frames of different time durations (from 0.5 min to 10 min) and each time frame was reconstructed to yield an average radioactivity distribution image for that frame. Time-activity curves (TACs) for

<sup>d</sup>  $^{11}\text{C}$ FMZ is a  $^{11}\text{C}$  labeled benzodiazepine antagonist.

three brain regions from the study in Figure 2.3 are shown in Figure 2.4. These TACs bear information about the neuroreceptor system(s) under investigation.

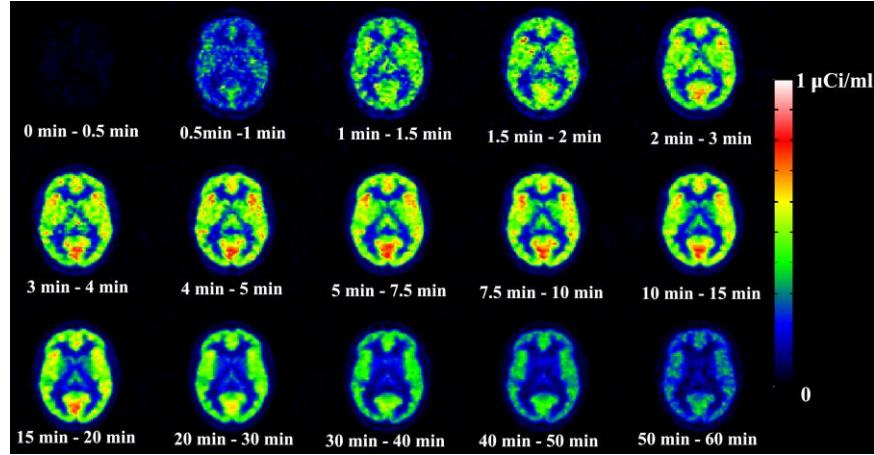


**Figure 2.3:** Dynamic sequence of a slice of a  $[^{11}\text{C}]$ FMZ study

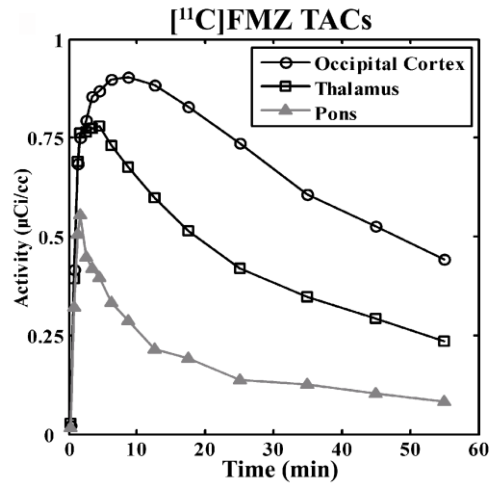


**Figure 2.4**  $[^{11}\text{C}]$ FMZ time-activity curves (TACs)

Let the measured TAC for a voxel  $i$  in the image volume be represented by the

vector  $\bar{y}_i = [y_i(T_1), y_i(T_2), \dots, y_i(T_N)]$ , where  $y_i(T_j) = \frac{1}{t_{end}^j - t_{start}^j} \int_{t_{start}^j}^{t_{end}^j} y_i(t) dt$  and  $t_{start}^j$  and

$t_{end}^j$  are the start and end times of the  $j^{\text{th}}$  frame,  $N$  is the number of frames in the study ( $N = 15$  in figures 2.3 and 2.4) and  $T_j$  is the time-point representing frame  $j$ , usually chosen to be the frame midpoint time. Mathematical modeling of these TACs is required to extract parametric estimates of brain function. For mathematical modeling of the TACs, a compartmental model for a tracer needs to be selected. This selection is based on the biochemical properties of the radiotracer which will be discussed next.

## 2.2 PET radiotracer

A PET radiotracer is a molecule labeled with a positron-emitting radionuclide. The molecule could be one that is naturally occurring (endogenous), or could be a chemical analog<sup>e</sup> of an endogenous substance, or could be a non-endogenous compound such as a drug. PET radiotracers are injected in very small quantities (nmol concentration) and are assumed not to perturb the system being studied but only ‘trace’ the process of interest. Each physical or biochemical state that the tracer attains is assumed to be homogeneous and the rates of transfer of the tracer from one state to another are assumed to be constant over the duration of the study. In other words, the state of the system being measured is assumed to be static over the scan duration.

The radiotracer is meant to target the system of interest being studied. For example, if a receptor system in the brain is of interest, the radiotracer usually would have the property of binding to the receptor of that system. For example [<sup>11</sup>C]raclopride binds to the dopamine D<sub>2</sub> receptors (Farde et al. 1989) while [<sup>11</sup>C]FMZ binds to benzodiazapine receptors (Koeppel et al. 1991). The dynamic PET signals obtained using these tracers can be used to measure their respective receptor densities. Tracers can also be used to measure the rate of enzyme action. Flurodeoxyglucose ([<sup>18</sup>F]FDG) (Huang et al. 1980) is a glucose analogue that may phosphorylate after crossing the blood brain barrier and can be used to measure the rate of glucose consumption, thus making it a very versatile biomarker for oncologic, neurologic and cardiac studies.

Figure 2.5 shows a simplified schematic of the processes taking place at the cellular level after injection of a commonly used radiotracer, [<sup>11</sup>C]FMZ. The radiotracer molecules (dark blue diamonds) cross the capillary membrane (red) and enter the free (or non-displaceable) space (grey) between the blood vessel and the neuronal terminals (yellow). The tracer is a benzodiazapine antagonist<sup>f</sup> and binds reversibly to the benzodiazepine receptors (light blue) on the post-synaptic terminal<sup>g</sup>. Other tracers may be designed to bind to pre-synaptic binding site shown in green or pre-synaptic storage

---

<sup>e</sup> an analog is a compound having properties slightly different from an endogenous substance.

<sup>f</sup> An antagonist is a molecule that has similar receptor affinity as the endogenous substance but opposite efficacy.

<sup>g</sup> Various other endogenous neurotransmitter systems and binding sites are present at any neuronal terminal but have not been shown in Figure 2.4 for simplicity.

vesicles shown as brown circles (e.g. methylphenidate ( $[^{11}\text{C}]\text{MPH}$ ) is a tracer that binds to the pre-synaptic dopamine reuptake site while dihydro-tetrabenzine ( $[^{11}\text{C}]\text{DTBZ}$ ) binds to the type 2 vesicular monoamine transporter (VMAT2) sites on the dopamine vesicles). The dynamic PET signal is a result of the interaction of the tracer with these cellular processes over time. These processes can be represented by a compartmental model such as shown in Figure 2.6 where the colors signify the same states as those in Figure 2.5.

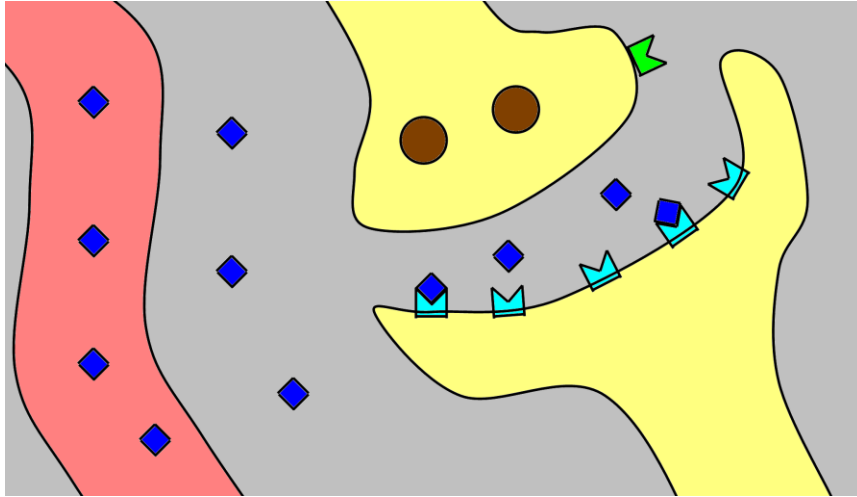


**Figure 2.5** Various possible states of  $[^{11}\text{C}]\text{FMZ}$  tracer molecules (dark blue): blood plasma (red), interstitial space (grey), benzodiazepine receptors on the post-synaptic side (light blue). The synaptic terminals are shown in yellow. Some other possible targets for a radiotracer are pre-synaptic binding sites (green) or pre-synaptic storage vesicles (brown).

### 2.3 Two tissue compartmental model

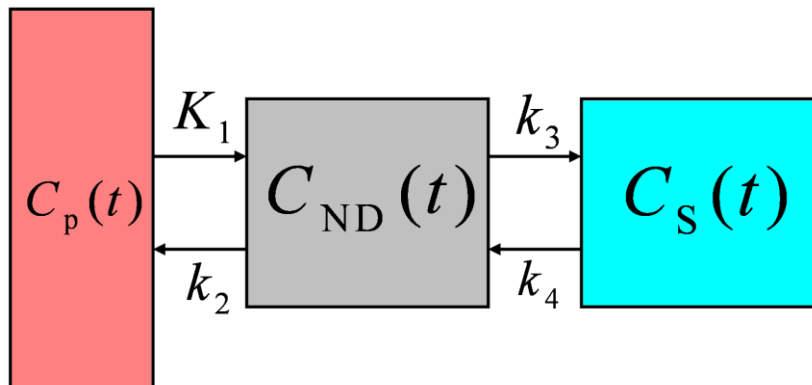


**Figure 2.6** Two tissue compartmental model

The possible states of [<sup>11</sup>C]FMZ as seen in Figure 2.5 can be represented using a two tissue compartmental model<sup>h</sup> shown in Figure 2.6 as first described for neuroreceptor PET studies by Mintun and colleagues (Mintun et al. 1984). The term  $C_p(t)$  represents the tracer concentration in blood,  $C_{ND}(t)$  represents the concentration in the non-displaceable compartment (free+non-specific) and  $C_s(t)$  represents the concentration of bound tracer in the specific (or bound) compartment. The kinetic parameters  $(K_1 - k_4)$ <sup>i</sup> represent the rates of conversion or transfer of the tracer molecules between the compartments. The ultimate goal of a PET study is the estimation of either all or at least a subset of these rate parameters which contain the important quantifiable pharmacological information of the system. For example, for benzodiazapine receptor imaging using [<sup>11</sup>C]FMZ, the parameter of interest is the non-displaceable binding potential ( $BP_{ND}$ ), a commonly used index of receptor binding site density. This is the ratio of the equilibrium concentration of specifically bound to non-displaceable radiotracer ( $BP_{ND} = \frac{C_s(t)_{equilibrium}}{C_{ND}(t)_{equilibrium}}$ ). Equilibrium

is the state at which there is no net transfer of tracer between the two compartments. The parameter of interest can also be defined in terms of the rate parameters and is given by  $BP_{ND} = \frac{k_3}{k_4}$  (Innis et al. 2007). Thus, estimation of the rate parameters of the model

enables the calculation of the parameter of interest. Another important concept in kinetic modeling is distribution volume (DV). It is the ratio of concentration between a compartment and plasma at equilibrium. For instance, the distribution volume of the non-displaceable compartment is given by  $DV_{ND} = \frac{C_{ND}(t)_{equilibrium}}{C_p(t)_{equilibrium}} = \frac{K_1}{k_2}$ . Although  $DV_{ND}$  is a

ratio (hence unitless), it is called a volume as it equals the volume of blood that contains the same activity as 1 ml of tissue (Carson 1996). Another commonly used parameter of interest is distribution volume ratio (DVR), which is an index of receptor binding site density. It is the ratio of the distribution volume of the tissue (non-displaceable and

---

<sup>h</sup> Since the plasma concentration is assumed to be known by arterial sampling, it is not classified as a compartment.

<sup>i</sup>  $K_1$  has units in ml(blood) ml<sup>-1</sup>(tissue) min<sup>-1</sup>,  $k_2 - k_4$  have units of min<sup>-1</sup>.

specific compartments together) to that of non-displaceable compartment which is given

$$\text{by } DVR = \frac{DV_{ND} + DV_S}{DV_{ND}} = \frac{\frac{K_1 + K_1 k_3}{k_2} + \frac{K_1 k_3}{k_2 k_4}}{\frac{K_1}{k_2}} = 1 + \frac{k_3}{k_4}. \text{ Thus } DVR = 1 + BP_{ND} \text{ (Innis et al. 2007).}$$

The choice of a specific model configuration is governed by various factors. First, it depends on the properties of the tracer. If the tracer is inert and does not interact with any receptor system or does not undergo any chemical change, but simply diffuses into and back out of the cells, a one tissue compartment model ( $k_3=k_4=0$ ) would be an appropriate model<sup>j</sup>. Another aspect of a radiotracer is its retention in the target tissue. Tracers like [<sup>11</sup>C]FMZ are not permanently trapped in the bound state and may convert back to the non-specific state ( $k_4 > 0$ ). However, a tracer like [<sup>11</sup>C]N-methylpeperine propionate ([<sup>11</sup>C]PMP) (Koeppel et al. 1999b) is metabolized by the enzyme acetylcholinesterase (AChE) and the metabolized state is retained in the tissue ( $k_4=0$ ). Thus, the reversibility of a tracer must be considered prior to choosing the model configuration.

Alternatively, the tracer might have additional interactions with other systems that are not of interest. For example, the tracer may bind to some non-specific site (say to a site on the pre-synaptic terminal) in addition to the specific binding site. In that case, a three compartment model would better describe the *in vivo* process.

However, biologically accurate models may not be practical. A model with higher complexity may be more accurate biologically, but may have too many parameters, and hence it would be impossible to accurately estimate all of the model parameters. Some models might work when statistical noise is low, but yield multiple solutions for high noise cases. Thus, model simplification may be required and some bias in parameter estimates will need to be allowed in order to obtain better precision. A number of configurations might have to be tested before choosing an appropriate model. For [<sup>11</sup>C]FMZ, a two tissue compartment model (Figure 2.6) has been shown to be a satisfactory model (Koeppel et al. 1991).

---

<sup>j</sup> An example of an inert tracer is [<sup>15</sup>O]H<sub>2</sub>O used for blood flow measurement.



The transfer of the tracer between the different model compartments can be mathematically represented using first-order differential equations based on the laws of mass transfer. The differential equations for the two-tissue compartment model in Figure 2.6 are shown below.

$$\frac{dC_{ND}(t)}{dt} = K_1 C_p(t) - (k_2 + k_3) C_{ND}(t) + k_4 C_S(t). \quad - 2.1$$

$$\frac{dC_S(t)}{dt} = k_3 C_{ND}(t) - k_4 C_S(t). \quad - 2.2$$

The total measured concentration of the radioligand in the tissue as a function of time is given by:

$$C_T(t) = C_{ND}(t) + C_S(t) = C_p(t) \otimes IR(t). \quad - 2.3$$

where,  $\otimes$  is the convolution operator and  $IR(t)$  is the impulse response of the compartmental model.  $IR(t)$  is a nonlinear function of the rate parameters of the two compartmental model<sup>k</sup>.

The model based TAC can be enumerated for any voxel  $i$  from Equation 2.3 as

$$\bar{C}_i = [C_{T_i}(T_1), C_{T_i}(T_2), \dots, C_{T_i}(T_N)], \quad \text{where} \quad C_{T_i}(T_j) = \frac{1}{t_{end}^j - t_{start}^j} \int_{t_{start}^j}^{t_{end}^j} C_{T_i}(t) dt \quad \text{and}$$

$t_{start}^j$  and  $t_{end}^j$  are the start and end times of the  $j^{\text{th}}$  frame,  $N$  is the number of frames in the study and  $T_j$  is the time-point representing frame  $j$ , usually chosen to be the frame midpoint. Let the parameters of the model for a given voxel  $i$  be listed in vector form as  $\bar{\theta}_i = [K_1, k_2, k_3, k_4]_i$ . The parameter vector for voxel  $i$  can be estimated by minimizing the difference between the measured time activity curve and the model predicted curve as follows:

$$\hat{\theta}_i = \arg \min_{\bar{\theta}_i} \|W(\bar{y}_i - \bar{C}_i)\|_2^2, \quad -2.4$$

where,  $W$  is the weighting matrix that takes into account the difference in variance

---

<sup>k</sup>  $IR(t) = A_1 e^{-\alpha_1 t} + A_2 e^{-\alpha_2 t}$ , with  $\alpha_1, \alpha_2, A_1$  and  $A_2$  being functions of the individual rate parameters,  $K_1$  to  $k_4$ .

between different frames of the PET scan. The normalized variance for the  $j^{\text{th}}$  frame is given as follows (Logan et al. 2001):

$$\sigma_j^2 = \frac{y_i(T_j)e^{\lambda T_j}}{t_{end}^j - t_{start}^j}, \quad - 2.5$$

where  $T_j$  is the midpoint time for the  $j^{\text{th}}$  frame and  $\lambda$  is the known tracer decay constant ( $\lambda = 0.0347 \text{ min}^{-1}$  for  $^{11}\text{C}$  tracers). The weighting matrix  $W \in \mathbb{R}^{N \times N}$  is a diagonal matrix with  $\frac{1}{\sigma_j^2}$  along the diagonal (Faraway 2004b).

Direct estimation of  $BP_{\text{ND}}$  ( $=k_3/k_4$ ) or DVR ( $= 1+BP_{\text{ND}}$ ) from equations 2.3 and 2.4 suffers from the practical difficulties of arterial blood sampling and the possible errors associated with it. The inconvenience associated with the arterial sampling approach has led to efforts in the PET community to move towards non-invasive approaches such as the reference region methods described in the following section.

## 2.4 Reference region models

Arterial sampling can be avoided if there is a region or tissue in brain that has negligible specific binding ( $k_3^{\text{ref}} = k_4^{\text{ref}} = 0, BP_{\text{ND}}^{\text{ref}} = 0$ ) also called the ‘reference region’ or ‘reference tissue’. Non-invasive reference-region-based approaches have been proposed in PET literature where the TAC of the reference region can be used as an ‘input’ instead of the arterial function for parameter estimation of the region of interest (target region) (Cunningham et al. 1991; Lammertsma et al. 1996). The two tissue compartment model for the reference region input function approach is shown in Figure 2.7.

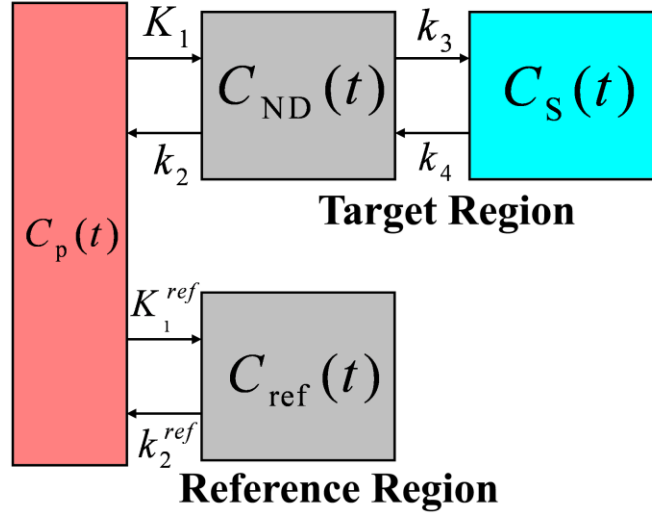


**Figure 2.7** Compartmental model for reference region approaches

The reference region approaches described here rely on two assumptions: (i) the TACs in the regions with specific binding (target regions) can be expressed as a function of the TAC of a region void of specific binding and the rate parameters and (ii) the ratio of rates of transfer of the radiotracer across the blood-brain barrier is the same throughout the brain ( $\frac{K_1^{ref}}{k_2^{ref}} = \frac{K_1}{k_2}$ ). This is equivalent to saying that the distribution volume of the non-displaceable tissue compartment ( $DV_{ND}$ ) is uniform throughout the brain.

For [ $^{11}\text{C}$ ]FMZ, the TAC of its reference region (pons) and two target regions (thalamus and occipital cortex) are shown in Figure 2.4. Three reference region approaches that have been employed in this thesis are described next.

### 2.4.1 Two compartment ‘full reference tissue model’ (RTM)

In the case of a reversible single-tracer, two-tissue compartment model, the target region concentration time courses or time-activity curves (TACs) can be expressed in terms of the model rate constants and reference region TACs using the full reference tissue input model equation shown in equation 2.6 below (Cunningham et al. 1991; Lammertsma et al. 1996):

$$y_i(t) = R_1(y_r(t) + ay_r(t) \otimes e^{-ct} + by_r(t) \otimes e^{-dt}), \quad - 2.6$$

where  $y_i(t)$  is the target region concentration time course for region or voxel  $i$ ,  $y_r(t)$  is the reference region concentration time course and  $R_I$ ,  $a$ ,  $b$ ,  $c$  and  $d$  are model parameters that are functions of the rate constants of a two tissue compartment model:  $K_1 - k_4$  and  $K_1^{ref}$ . The parameter  $R_I$  in equation 2.6 is an index of transport across the blood brain barrier ( $R_I = \frac{K_1}{K_1^{ref}}$ ). The full reference tissue model has four unknown parameters and they can be arranged in a vector form as:

$$\bar{\theta}_i = [R_1, k_2, k_3, BP_{ND}]_i \quad - 2.7$$

Thus, from equations 2.6 and 2.7 a target region TAC can be expressed in terms of the function of the reference region TAC ( $\bar{y}_r$ ) and the parameter vector ( $\bar{\theta}_i$ ) plus a residual error term ( $\bar{\varepsilon}_i$ ) as shown below:

$$\bar{y}_i = f(\bar{y}_r, \bar{\theta}_i) + \bar{\varepsilon}_i . \quad - 2.8$$

The rate parameters can be estimated by minimizing the difference between the model predicted and measured TACs, similar to the minimizing step in equation 2.4 as follows:

$$\hat{\theta}_i = \arg \min_{\theta_i} \|W\{\bar{y}_i - f(\bar{y}_r, \bar{\theta}_i)\}\|_2^2 . \quad - 2.9$$

## 2.4.2 Simplified reference tissue model (sRTM)

The four parameter model in Equation 2.6 can be further simplified and converted into a three parameter model if the equilibration between the non-displaceable and specific compartments is rapid ( $k_3, k_4 \gg 0$ ) (Lammertsma and Hume 1996). If this condition is true, the time activity curves can be expressed as a function of the reference tissue curve and the three model parameters for any voxel  $i$  as:

$$y_i(t) = R_1 y_r(t) + [k_2 - \frac{R_1 k_2}{1 + BP_{ND}}] y_r(t) \otimes e^{\frac{-k_2 t}{1 + BP_{ND}}} \quad - 2.10$$

The parameter vector per for each voxel  $i$  ( $\bar{\theta}_i = [R_1, k_2, BP_{ND}]_i$ ) can be estimated by a minimization step similar to the one in Equation 2.9.

The arterial input based model for TACs (Equation 2.3), the full reference tissue model (Equation 2.6) and simplified reference tissue model (Equation 2.10) are nonlinear functions of rate parameters and the ‘input functions’. Hence, the minimization step for the arterial sampling approach (Equation 2.4) and RTM and sRTM (Equation 2.9) requires nonlinear least squares algorithms which are computationally intensive and may not converge in the case of noisy data. Logan plot based parameter estimation, to be discussed next, is computationally efficient as it requires ordinary least squares estimation.

### 2.4.3 Reference region-based Logan plots

Logan plot analysis has been used extensively in the PET community because of its simplicity and model configuration independence. Logan plot analysis was originally developed for use with arterial sampling (Logan et al. 1990) and later adapted for the non-invasive reference region approach (Logan et al. 1996). Reference region based Logan plot analysis is a computationally efficient method where ordinary least squares (OLS) can be used to estimate the distribution volume ratio (DVR). The operational reference region-based Logan equation obtained after transformation of dynamic PET data is shown in equation 2.11.

$$\frac{\int_0^{T_i} C_T(t) dt}{C_T(T_i)} = DVR \frac{\int_0^{T_i} C_{ref}(t) dt + \frac{C_{ref}(T_i)}{k_2^{ref}}}{C_T(T_i)} + INT, \quad - 2.11$$

where,  $INT$  is an intercept term,  $T_i$  is the midpoint time of the ‘ $i$ ’th frame and  $k_2^{ref}$  is the population average value of  $k_2$  for the reference region. The plot of the dependent

variable  $\left(\frac{\int_0^{T_i} C_T(t) dt}{C_T(T_i)}\right)$  and independent variable  $\left(\frac{\int_0^{T_i} C_{ref}(t) dt + \frac{C_{ref}(T_i)}{k_2^{ref}}}{C_T(T_i)}\right)$  becomes linear

after some time  $T^*$ , and the slope of the line is DVR, the parameter of interest. The blood-

brain-barrier transport parameter,  $R_1$ , can also be calculated from the regression parameters ( $R_1 = \frac{-DVR}{INT \times k_2^{ref}}$ ) and gives the measure of the transport rate of any target region relative to the reference region. Figure 2.8 shows the Logan plots for the TACs in Figure 2.4, using pons as the reference region.

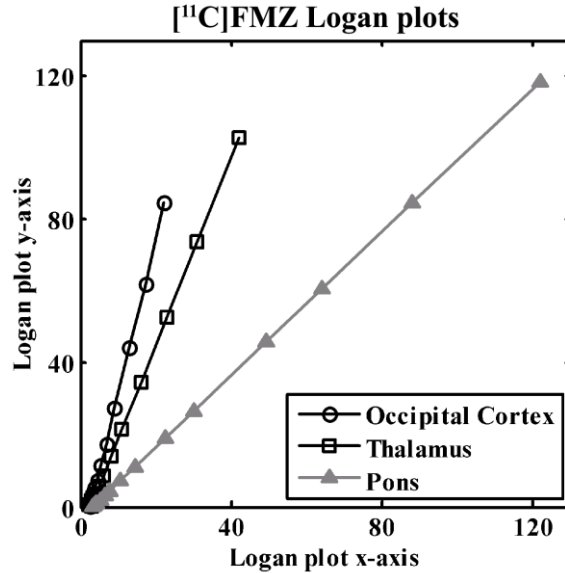


Figure 2.8: Logan plots for occipital cortex (DVR = 4.3), thalamus (DVR=2.6) and pons (DVR=1.0).

For the dynamic slice sequence shown in Figure 2.2, voxel-wise estimates of the transport and binding parameters allow creation of parametric images estimated using Logan plots as shown in Figure 2.9.

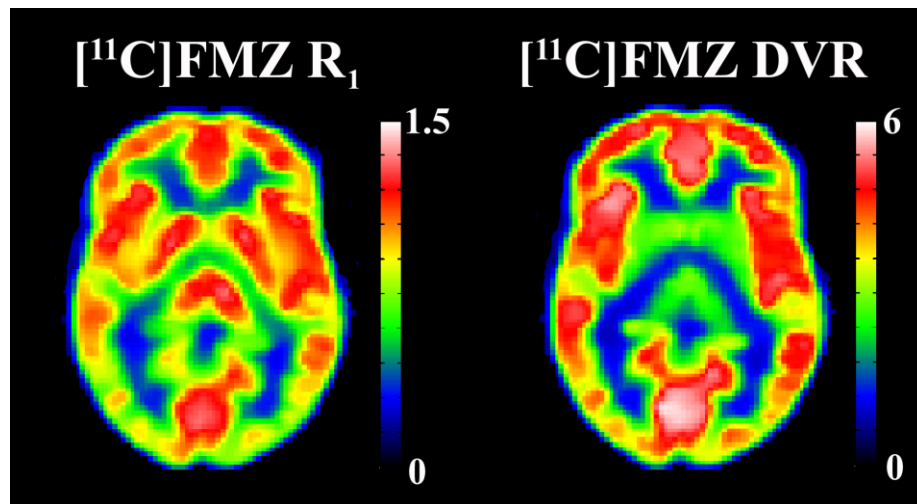


Figure 2.9  $R_1$  and DVR images from dynamic  $[^{11}\text{C}]\text{FMZ}$ .

However, the DVR estimation using Logan plots suffers from bias due to noise in the voxel TACs. Minimizing this bias while at the same time keeping the parameter variance low, is essential for the multiple neuropharmacological measurement studies. The next chapter discusses the cause of the bias in Logan plots and proposes a PCA-based Logan plot approach to reduce bias without increasing parameter variance.

## **Chapter 3**

### **Improving PET receptor binding estimates from Logan plots using principal component analysis**

This chapter introduces a novel principal component analysis (PCA) based approach for reducing bias in distribution volume ratio (DVR) estimates from Logan plots in PET. Logan plot analysis is an ordinary least squares (OLS)-based method for estimation of distribution volume ratio (DVR), an index of receptor binding site density, for reversible PET tracers (see section 2.4.3). This method is used extensively in the PET community because of its simplicity and model configuration independence. However, negative bias exists in Logan plot-based DVR estimates owing to noise present in the PET time activity curves (TACs). To reduce the bias in single measurement PET studies, various methods have been proposed previously for the arterial sampling approach and will be reviewed in Section 3.2 (Ichise et al. 2002; Logan et al. 2001; Ogden 2003; Varga and Szabo 2002). In this work, for the first time, these existing methods were applied to the reference region approach. We found that these methods either removed the bias at the expense of precision or removed only part of the bias or both.

This chapter introduces a novel method for reducing the Logan plot bias using principal component analysis (PCA) without increasing the variance of the DVR estimates. PCA is a feature extraction technique used to simplify a dataset by reducing its dimensionality while maintaining its relevant characteristics. PCA has been used extensively in nuclear imaging, including PET, in the spatial domain (Barber 1980; Pedersen et al. 1994; Razifar et al. 2006; Thireou et al. 2003) where the investigators have analyzed the images of the coefficients of individual principal components. Frequency analysis of dynamic structures (FADS), where the principal components are rotated to avoid negative values has been used in temporal domain in SPECT (Sitek et al. 1999). In the present work, we apply PCA to achieve temporal smoothing of PET TACs



to reduce the bias in DVR estimates (Section 3.3). The PCA-based Logan plot approach is compared with the existing bias removal methods in both simulation studies (Section 3.4) and human brain scans (Section 3.5).

### 3.1 The cause of bias in Logan plots

In the operational equation for reference region-based Logan analysis (Equation

2.11) the numerators in both the dependent variable  $\left(\frac{\int_0^{T_i} C_T(t) dt}{C_T(T_i)}\right)$  and the independent

variable  $\left(\frac{\int_0^{T_i} C_{ref}(t) dt + \frac{C_{ref}(T_i)}{k_2^{ref}}}{C_T(T_i)}\right)$  have integral terms and are relatively noise free as

compared to the denominators. The presence of the noisy term ( $C_T(T_i)$ ) in the denominators on both sides of Equation 2.11 is the cause of correlated errors in the dependent and independent terms of the Logan plot equation leading to negative bias in DVR estimates (Slifstein and Laruelle 2000). This bias is more pronounced in regions with high DVR values. Reduction of noise in the measured TACs will assist in reducing the correlated errors leading to a reduction in the bias. We have developed a principal component analysis (PCA) based approach to achieve this goal.

### 3.2 Existing bias removal techniques

To reduce the bias in single measurement PET studies, various methods have been proposed previously for the arterial sampling based Logan approach (Ichise et al. 2002; Logan et al. 2001; Ogden 2003; Varga and Szabo 2002). The operational Logan equations for both arterial sampling and reference region approaches have the same problem of correlated errors in the dependent and independent variables. Hence, the above mentioned methods, though developed for the arterial sampling implementation are also applicable to the reference region approach.

The OLS method accounts only for errors in the dependent variable. The TLS method (Varga and Szabo 2002) takes into account errors in both dependent and independent variables of the Logan plot to estimate DVR. This can be classified as a method using an alternate cost function. LEGA (Ogden 2003) and MA1 (Ichise et al. 2002) can be classified as methods rearranging the original Logan plot equation. In LEGA, a rearrangement of the operational Logan plot equation makes the error term additive. The problem is then solved by maximum likelihood approach. In MA1, equation (5) is rearranged to bring the noisy term to one side of the equation and DVR is estimated by taking the ratio of two regression coefficients. GLLS (Logan et al. 2001) can be classified as a temporal smoothing method. In this method each noisy TAC is separated into two segments which are individually fitted to one compartment model using Generalized Linear Least Squares (Feng et al. 1996). The smoothed segments are pieced together to get a smooth TAC which is then used to obtain Logan DVR estimates. We have found that these existing methods were either unsuccessful in removing all of the bias or removed bias at the expense of precision or both. The new PCA-based bias removal approach can also be classified as a temporal smoothing method where a PCA-based lower dimension linear model is used to reduce the noise in the tissue curves.

### **3.3 Principal Component Analysis (PCA) for Logan-plot bias reduction**

PCA is a feature extraction technique used to simplify a dataset by reducing its dimensionality while maintaining its important characteristics (Faraway 2004a). In feature extraction, data space is transformed into a 'feature' space having the same dimensions as the data set. This transformation is such that the data set can then be represented by a reduced number of dominant 'features' while retaining all the important intrinsic characteristics of the original data. Using PCA, each original data vector of dimension ' $p$ ' can be expressed as a linear combination of ' $p$ ' orthogonal basis vectors. By limiting the number of basis vectors to ' $q$ ' dominant vectors ( $q < p$ ), data can be represented with a reduced dimensionality thus reducing the noise while preserving the important features in the data. Using PCA, the noise in the PET TAC values ( $C_T(T_i)$ ) can

be reduced thus also reducing the correlated errors in equation 2.11, which are the cause of the DVR bias.

The classical model for a PET TAC is a non-linear function of rate parameters (Equation 2.3). Here we represented dynamic PET data using a PCA-based linear model. Thus, a noisy tissue curve vector for the  $j^{\text{th}}$  voxel,  $\bar{y}_j = [y_j(T_1), y_j(T_2), \dots, y_j(T_p)]' \in R^{p \times 1}$  from a PET study involving ' $p$ ' temporal frames can be expressed as:

$$\bar{y}_j = G\bar{x}_j + \bar{\varepsilon}_j, \quad - 3.1$$

where  $G \in R^{p \times q}$  is the system matrix to be constructed using PCA ( $q < p$ ),  $\bar{x}_j \in R^{q \times 1}$  is the coefficient vector and  $\bar{\varepsilon}_j \in R^{p \times 1}$  is the vector of residuals. For obtaining the system matrix, a training set is required. We used the time activity curves from all the voxels in the PET image volume as the training set.

Let the training set contain ' $d$ ' TACs from the dynamic PET data. These ' $d$ ' curves can be arranged row-wise in the matrix form as follows.

$$X = \begin{bmatrix} y_1(T_1) & \cdots & y_1(T_p) \\ \vdots & \ddots & \vdots \\ y_d(T_1) & \cdots & y_d(T_p) \end{bmatrix}. \quad - 3.2$$

Matrix  $X_0$  is obtained by subtracting the column mean vector ( $\bar{\eta}$ ) from each row of  $X$ . The principal components are the eigenvectors of the sample covariance matrix of  $X_0$  ( $S = \frac{1}{d-1} X_0 X_0^T$ ) and are obtained using singular value decomposition (SVD). The total number of principal components is equal to  $p$ , the number of frames in the PET study. These components can be ordered in the decreasing order of their eigenvalues as  $F = [\bar{f}_1 \bar{f}_2 \dots \bar{f}_p]$  where  $\bar{f}_i \in R^{p \times 1}$  and  $F \in R^{p \times p}$ . The mean vector  $\bar{\eta}$  and a subset of the principal components (depending on their eigenvalues) is chosen to construct the system matrix  $G = [\bar{\eta} \bar{f}_1 \bar{f}_2 \dots \bar{f}_q]$  ( $q < p$ ). The coefficient vector  $\bar{x}_j$  in Equation 3.1 for each noisy curve  $\bar{y}_j$  can be estimated by least squares minimization as follows.

$$\hat{\bar{x}}_j = (G'G)^{-1} G' \bar{y}_j. \quad - 3.3$$

The PCA-based fitted tissue curve can then be obtained as shown below.

$$\hat{y}_j^{PCA} = G\hat{x}_j = G(G'G)^{-1}G'\bar{y}_j. \quad 3.4$$

The process of obtaining the principal components using PCA from the training set has a closed form expression and hence is straightforward. Selection of ‘ $q$ ’ for a particular tracer is made from simulations. Training data and test data are simulated using the literature range of tracer parameter values and the expected shape of the arterial input function. The principal components are obtained from the simulated training set and ‘ $q$ ’ is selected to be the minimum number such that  $G$  ( $=[\bar{\eta} \ f_1 \ f_2 \dots \ f_q]$ ) is a valid system matrix for simulated test data.

In human studies, the training data and the test data are the same and include all the TACs in the PET image volume. Principal components for each subject are obtained from the training set and system matrix is formed using the number ‘ $q$ ’ selected from simulations. This system matrix is then used to fit the test data.

## 3.4 Simulations

### 3.4.1 Simulation Design

Simulations were performed mimicking the relatively slowly equilibrating radiotracer [ $^{11}\text{C}$ ]carfentanil (CFN), a reversible  $\mu$ -opioid agonist. A partial bolus followed by continuous infusion was simulated for tracer administration (60% bolus and 40% infusion). This was the same bolus to infusion ratio used in the human scans. The local rates of delivery of the radiotracer and clearance rate of the radiotracer to the plasma was same for the target region and the reference region ( $K_1 = K_1^{ref}$ ,  $k_2 = k_2^{ref}$ ), although this assumption is not required by the reference region method. The training set was simulated using the kinetic parameter ranges reported previously (Endres et al. 2003) as shown in Table 3.1. The training set consisted of 2496 noisy curves (all with unique kinetic parameter combinations) of a 70 minute - 16 frame scan (4 x 0.5 min, 3 x 1 min, 2 x 2.5 min, 2 x 5 min, 5 x 10 min), which is the same protocol used for human scans at our institution. The principal components were obtained from this training set.

The test data consisted of six hypothetical regions (Table 3.1, Figure 3.1): four of them with receptor binding, having true DVR values of 5, 4, 3, 2, and one without receptor binding having true DVR = 1 were sampled from the training set. It is possible

**Table 3.1:** Kinetic parameters ranges for [<sup>11</sup>C]carfentanil simulations

Parameter	Training Parameters <sup>+</sup>	Test Parameters
$K_1$ (ml g <sup>-1</sup> min <sup>-1</sup> )	[0.1: 0.02: 0.24]	0.2
$k_3$ (min <sup>-1</sup> )	[0: 0.02: 0.5]	[0.1: 0.1: 0.4], 0.7*
$k_4$ (min <sup>-1</sup> )	[0.08: 0.02: 0.14]	0.1
$V_e$ (ml/mL)	[1.32: 0.27: 1.86]	1.59

(<sup>+</sup>[a : b : c] ⇒ from a to c in steps of b. \* atypical curve)

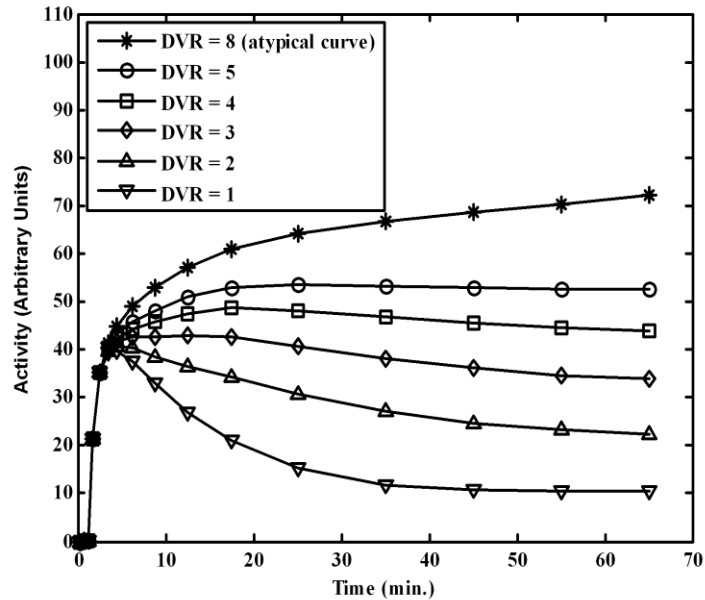


**Figure 3.1:** Noiseless time activity curves (TACs) for simulated test data. The test data comprised five hypothetical regions with receptor binding having true DVR values of 8, 5, 4, 3, and 2 and reference region with no binding (DVR = 1). The curve corresponding to DVR = 8\* is an atypical curve that is not present in the training set. Realistic voxel-level noise was added to these noiseless curves to obtain 1024 realizations for each DVR value.

for a small region of the brain to have very different kinetics from those observed elsewhere. Since the proposed PCA method is training set based, its sensitivity to a region of unusual kinetics not part of the training set needed to be evaluated. To examine

this, a sixth region with substantially greater DVR than any curve present in the training set was added to the test set (DVR = 8). Noiseless TACs for these six regions are shown in Figure 3.1. Realistic voxel-level noise was added to obtain 1024 realizations for each of these curves using the noise model in Equation 2.5. The principal components obtained from the simulated training data were used to construct the system matrix and fit the curves in the simulated test data. DVR estimates were then obtained by replacing the noisy TAC values in the denominators of Equation 2.11 with the values of the PCA-based fitted curves.  $T^*$ , the time beyond which the Logan plot is linear, was chosen to be 20 minutes based on the known characteristics of carfentanil. The integrals in the numerators of Equation 2.11 were calculated using trapezoidal approximation (Ogden 2003). The curve simulated for the region with no specific binding (DVR = 1) was used as the reference region in the Logan analysis.

It must be noted that since no blood samples are measured in reference region approaches, correction for a blood volume component (vascular contribution to the PET data) is not possible. Not correcting for blood volume will introduce a systematic bias in the DVR estimates in human scans unrelated to the noise induced bias (Logan et al. 1996). To check the magnitude of this systematic bias on the proposed and existing methods, separate simulations were also performed with a blood volume component using the following model.

$$C(t) = V_B C_B(t) + (1 - V_B) C_T(t) \quad - 3.5$$

where  $C(t)$  is the total radioligand concentration measured in a voxel,  $V_B$  is the blood volume component (chosen to be 3.5%) and  $C_B(t)$  is the blood radioligand concentration. Data was simulated including a blood volume component as in equation 3.5, but analyzed ignoring its contribution.

DVR values for the above simulations were estimated using the following six methods and the results are reported in the next subsection.

- (1) Ordinary Least Squares (OLS) (Logan et al. 1996)
- (2) Total Least Squares (TLS) (Varga and Szabo 2002)
- (3) Generalized Linear Least Squares (GLLS) (Logan et al. 2001)

- (4) Likelihood Estimation Graphical Analysis (LEGA) (Ogden 2003)
- (5) Multi-Linear Analysis - 1 (MA1) (Ichise et al. 2002)
- (6) Principal Component Analysis (PCA) (Joshi et al. 2008a)

### 3.4.2 Simulation Results

The mean vector ( $\bar{\eta}$ ) and first 3 principal components ( $\bar{f}_1, \bar{f}_2$  and  $\bar{f}_3$ ) obtained from the simulated carfentanil training data without blood volume component are shown in Figure 3.2. The first 3 components had eigenvalues of  $1.24 \times 10^3$ , 278.75 and 7.91 while the next to last and last components had eigenvalues of  $6.36 \times 10^{-32}$  and  $< 10^{-50}$ , respectively. This progression of eigenvalues (eigenvalue $_{i-1} \gg$  eigenvalue $_i$ ) indicated that the first few components are the dominant vectors and capture most of the variance in the training set.

The box plots in Figure 3.3 show the comparison of DVR estimates obtained using OLS with those estimated by increasing numbers of components for true DVR = 5 (PCAn  $\Rightarrow G = [\bar{\eta} \bar{f}_1 \bar{f}_2 \cdots \bar{f}_n]$ ). In the presented PCA approach, we fit the noisy TACs as a linear combination of the principal components (16 possible vectors) as well as the mean vector. In all, 17 PCA-based models are possible; the model with smallest degrees of freedom is PCA0 with the mean vector alone ( $G = [\bar{\eta}]$ ) and the one with largest degrees of freedom is PCA16 with mean vector and all the 16 principal components ( $G = [\bar{\eta} \bar{f}_1 \bar{f}_2 \cdots \bar{f}_{16}]$ ).

Too few components were insufficient to model the data and yielded biased estimates with high precision, as seen for PCA0 which used the scaling of only the mean vector. As the number of components was increased, the bias was reduced at the expense of precision (PCA1, PCA2, PCA3). However, as the number of components exceeded three, the bias returned, as the added components begin to fit noise in the data. Using all 16 principal components (PCA16), as expected, gave back the original noisy data and the box plot in this case is identical to the box plot for OLS. PCA16 uses 17 vectors (mean vector and 16 components) while PCA15 uses 16 vectors (mean vector and 15 components) to model the 16 frame data. The mean vector can be expressed as a linear

combination of the 16 principal components. Since only 16 independent vectors are needed for perfect description of the 16 frame data, PCA15 and PCA16 will give identical results.

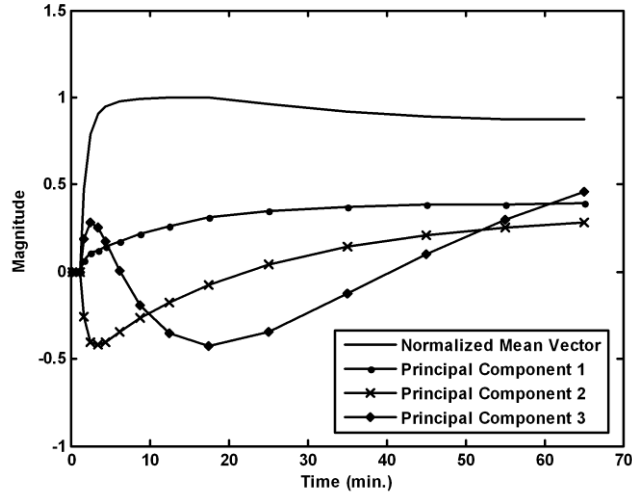


**Figure 3.2:** Mean vector and first 3 principal components for carfentanil-like tracer simulation studies. The mean vector is the mean of the entire training data while the 3 principal components are the dominant vectors obtained from the PCA with the three largest eigenvalues.

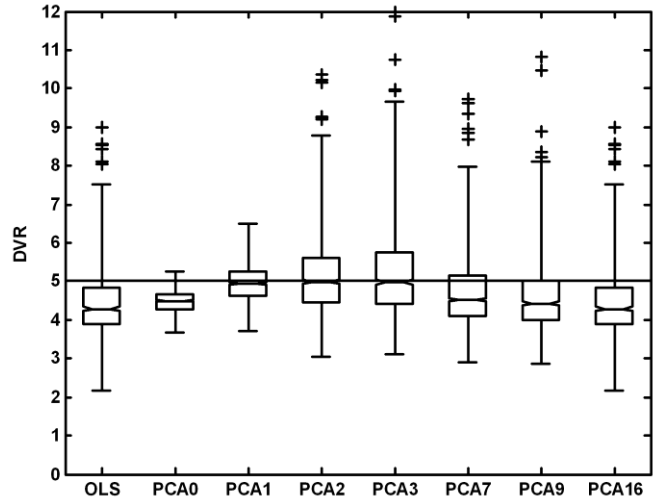


**Figure 3.3:** Box plot comparisons of DVR estimates obtained with an increasing number of principal components in single measurement simulation studies (True DVR=5). The individual boxes have lines at the lower quartile, median, and upper quartile values. The whiskers extend from the ends of the box to the most extreme value within three times the interquartile range in each direction. DVR estimates beyond the whiskers are marked as outliers (denoted by '+'). PCA $n$   $\Rightarrow$  PCA fit with first  $n$  principal components and the mean vector. When all 16 components are used (PCA16), the results are identical to the original OLS estimation.



PCA1 ( $G = [\bar{\eta} \ \bar{f}_1]$ ) provided the best bias-variance trade-off for true DVR = 5. This implied that a linear combination of only two curve shapes could sufficiently approximate the simulated test data with DVR = 5 ( $q = 2$ ). To check the validity of this finding for all the simulated TACs in the test set, we analyzed the residuals between the true noiseless TACs ( $\bar{y}_j^{true}$ ) and the PCA1-fitted TACs ( $\hat{y}_j^{PCA1}$ ,  $1 \leq j \leq 1024$ ). For the  $j$ 'th realization, the residual at  $i$ 'th frame is given by  $residual_j(T_i) = \bar{y}_j^{true}(T_i) - \hat{y}_j^{PCA1}(T_i)$  ( $1 \leq i \leq p$ , where  $p = 16$  is the number of frames in the study). These residuals were normalized by the true tissue curve values to obtain the percent-normalized residuals ( $= \frac{residual_j(T_i)}{\bar{y}_j^{true}(T_i)} \times 100$ ). For a model to be valid, the mean of these percent-normalized residuals must lie close to zero (Carson 1986). Figure 3.4 shows that for TACs with receptor binding that were part of the training set (DVR = 5, 4, 3 and 2), the mean of percent-normalized residuals was close to zero (between  $\pm 3\%$ ). For reference region

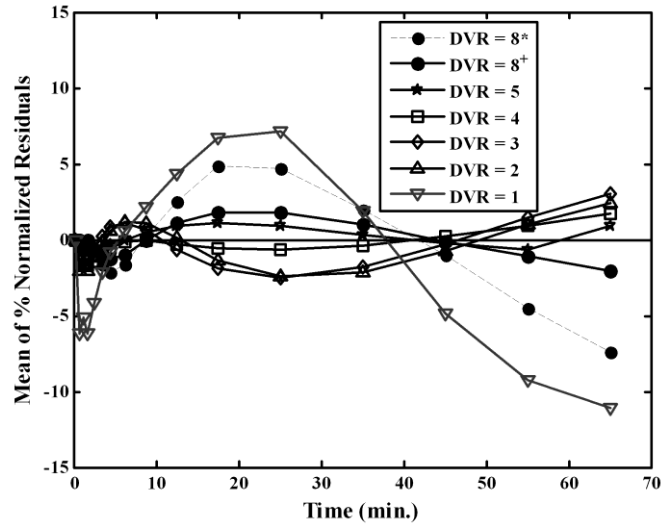


**Figure 3.4:** The mean of percent-normalized residuals between the PCA1-based curve approximations and the true tissue curves in single measurement simulation studies. The plot indicates that PCA1 model is valid for TACs with receptor binding that were part of the training set (DVR = 5, 4, 3 and 2). For reference region curve (DVR = 1) and atypical curve not part of the training set (DVR = 8), however, the model is not valid as the mean of percent-normalized residuals is significantly different than zero. Including curves similar to the atypical curve in the simulated training set (1% of the total curves) improves the fit (DVR = 8<sup>+</sup>).

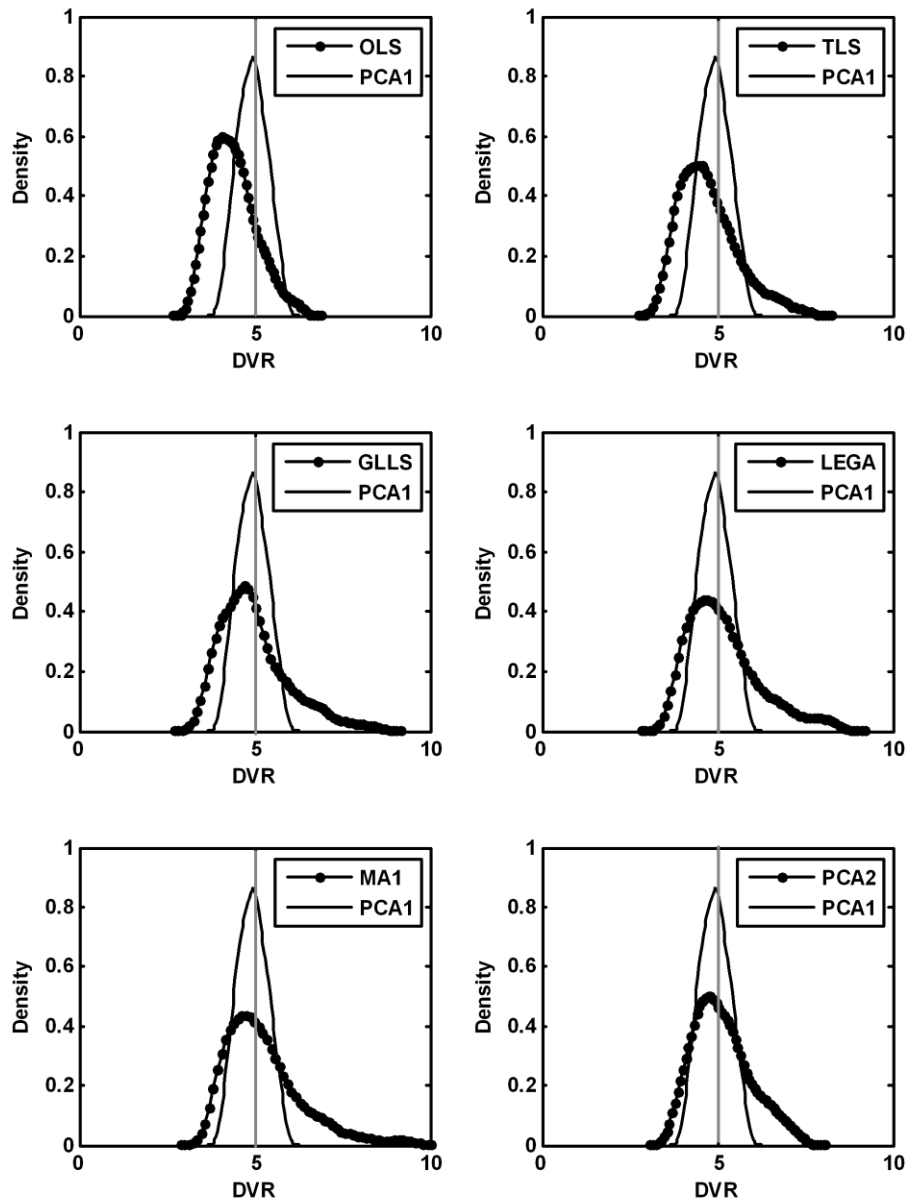
TAC (DVR = 1,  $k_3=0$ ) and for the atypical TAC not included in the training set (DVR = 8) the mean of the percent-normalized residuals was significantly different than zero

indicating that PCA1 was not a valid model for these curves. This makes intuitive sense as the reference region curve (shown in Figure 3.1,  $DVR = 1$ ) has a more complicated shape compared to the curves with receptor binding due to rapid clearing of the tracer. PCA3 (mean vector and three components) was found to be a valid model for the reference region. It should be pointed out that the actual reference region TAC used in the Logan plot calculations is not fitted using PCA, but is the raw TAC. Since the reference region is not derived from a single voxel, but is obtained from a volume-of-interest large enough to have minimal statistical noise, the raw reference region curve can be used for all DVR estimations without introduction of bias or loss of precision. Furthermore, the DVR estimates in regions of very low binding were found to be nearly unbiased even with non-zero residuals resulting for the PCA1 fit as seen in the last column of Table 3.2.

The invalidity of the PCA1 model for the atypical curve is also expected as the success of PCA-based approach depends on the diversity of the training set and if a curve shape is significantly different from any in the training set, the PCA1 model may not be adequate. However, in human studies the training set consists of all the TACs in the PET image volume. Thus, a region with unusual kinetics, if any, will contribute curves to the training set. If we include curves similar to the atypical curve in the simulated training set (1% of the total curves) the fit improves as seen in Figure 3.4 ( $DVR = 8^+$ ).

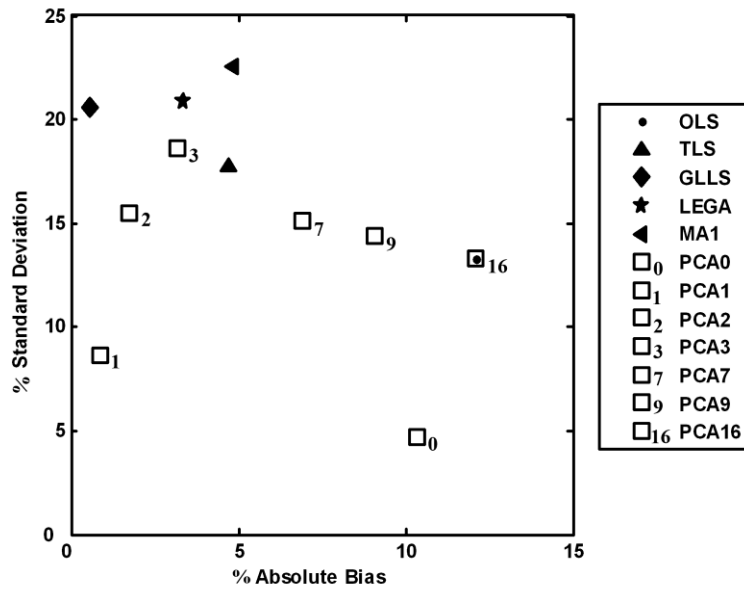
The standard deviations of the percent normalized residuals for PCA1-based TACs calculated above were approximately 50% of that for original noisy tissue curves. Thus, from this result and Figure 3.4 we could conclude that PCA1 model was valid for the curves with receptor binding that were part of the training set and provided TACs with reduced noise.

More detailed results have been presented for the curve simulated with  $DVR = 5$ . The histograms in Figure 3.5 show the distribution of the DVR values estimated by each of the existing methods vs. PCA1. A Gaussian kernel with unbounded support was used to smooth the histograms. These plots were useful for visualizing asymmetries and tails in the distribution of the estimated DVR values. The vertical line denotes the ‘true’ DVR value. The modes of the histograms of all the existing methods either lie below the true DVR value, show heavy tails, or both. PCA2 has its mode at the true value but has a heavier tail than PCA1. PCA1 was seen to be superior to all the existing methods.



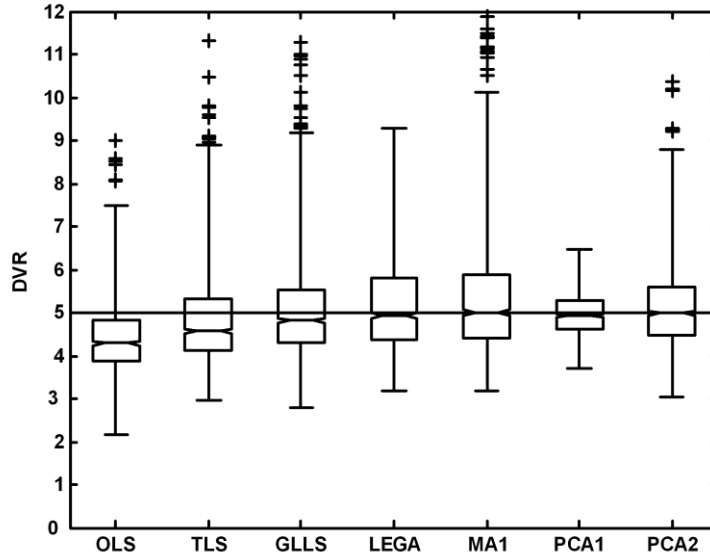
**Figure 3.5:** Comparison of distribution of the DVR values estimated by each of the existing methods vs. PCA1 in single measurement simulation studies for true DVR = 5. (discarding top and bottom 2.5 percentiles). TLS, GLLS and LEGA have modes lower than the true value but higher than that for OLS. MA1 has a heavier tail due to overestimations. PCA1 proves to be the best estimator with a narrow unbiased distribution as compared to all the methods. The distribution of DVR estimates with PCA2 has its mode at the true value but has a heavier tail than PCA1.

Figure 3.6 depicts the trade-off between precision and bias in the DVR estimates of the different approaches, again for DVR = 5.



**Figure 3.6:** Trade-off between bias and precision for the existing and proposed bias removal methods in single measurement simulation studies (discarding top and bottom 2.5 percentiles). The plot shows percent absolute bias versus percent standard deviation for true DVR = 5. The original OLS method shows high bias, which is removed at the expense of some increase in estimation variability by the existing bias removal methods. If the proposed method was under parameterized (PCA0) or over parameterized (PCA7, PCA9, PCA16), bias returned. PCA1 yielded the best compromise between bias and precision.

An ideal estimator has no bias and minimal variance and would lie near the origin. OLS (superimposed with PCA16) is on the far right denoting the bias present due to noise. TLS removes only a portion of the bias. GLLS, LEGA, MA1, PCA2 and PCA3 reduce the bias but also have poorer precision. PCA1 shows the best performance and is closest to the origin than any other method. Figure 3.7 shows box plots for DVR estimates from all methods (DVR = 5). The median and range of DVR estimates using OLS is below the true value as expected. The bias in the median is reduced only slightly using TLS with a decrease in precision. GLLS, LEGA, MA1 and PCA2 reduce the bias almost entirely but have high variance. PCA1 eliminates bias almost completely and yields the best precision estimates of any of the methods.



**Figure 3.7:** Box plot comparisons of the DVR estimates obtained using the existing bias removal methods and the proposed bias removal method for single measurement simulation studies (true DVR = 5). TLS reduces only part of the bias. GLLS, LEGA and PCA2 (with a wide inter-quartile distance) and MA1 (with large number of outliers) reduce most of the bias but at the expense of precision. PCA1 reduces bias along with an improvement in estimation precision.

Table 3.2 summarizes the means and standard deviations of the estimated DVR values in units of percent of true value for all the simulated test curves. Though the trends for  $DVR < 5$  (last four columns) are similar to those seen in Figure 3.7 ( $DVR = 5$ ), bias for OLS is lower for curves with lower DVR values as expected (Slifstein and Laruelle 2000). The first two columns show statistics for the atypical TAC with bias in the PCA1 estimate of DVR when the atypical curve is not part of the training set ( $DVR = 8$ , column 1) and reduction in bias when atypical curve shapes are included in the training set ( $DVR = 8^+$ , column 2). Inclusion of curve shapes similar to the atypical curve in the training set (1% of total curves) improves the fit but does not remove the bias completely for PCA1. The representation of atypical curve shapes in the training set was required to be at least 5% for the bias to be completely removed for PCA1. Thus, very small regions with unusually shaped TACs, if identified prior to Logan analysis, could be fitted with PCA2 where bias is removed almost completely but at the expense of precision.

Figure 3.8 shows the box plot for DVR estimates from all methods for curves simulated with but not corrected for the blood volume component ( $DVR = 5$ ). The box plots have similar bias-variance trends as in Figure 3.7 apart from the consistent bias seen

in Figure 3.8 for all methods due to uncorrected blood volume component. This bias is minimal ( $< 5\%$ ) compared to the noise induced bias in OLS ( $>10\%$ ) for  $DVR=5$  and is even smaller for lower DVR values.

**Table 3.2:** Bias, given as percent of true value, and standard deviation in units of percent of true value ( $n = 1024$ ).

	DVR = 8	DVR = 8 <sup>+</sup>	DVR = 5	DVR = 4	DVR = 3	DVR = 2	DVR = 1
<b>OLS</b>	77 (13)		87 (12)	90 (11)	92 (10)	94 (9)	97 (7)
<b>TLS</b>	93 (23)		95 (17)	94 (13)	95 (12)	96 (9)	97 (7)
<b>GLLS</b>	95 (26)		99 (20)	99 (15)	100 (13)	100 (10)	98 (8)
<b>LEGA</b>	100 (19)		105 (22)	102 (16)	102 (13)	102 (11)	101 (8)
<b>MA1</b>	107 (34)		106 (24)	103 (17)	102 (14)	102 (11)	103 (8)
<b>PCA1</b>	87 (7)	91 (9)	100 (8)	101 (8)	101 (8)	102 (8)	97 (7)
<b>PCA2</b>	98 (19)	99 (16)	102 (16)	102 (14)	102 (12)	101 (10)	98 (7)

A value of 100 represents ‘no bias’.

<sup>+</sup> PCA training set including curve shapes similar to the atypical curve (1% of total curves).

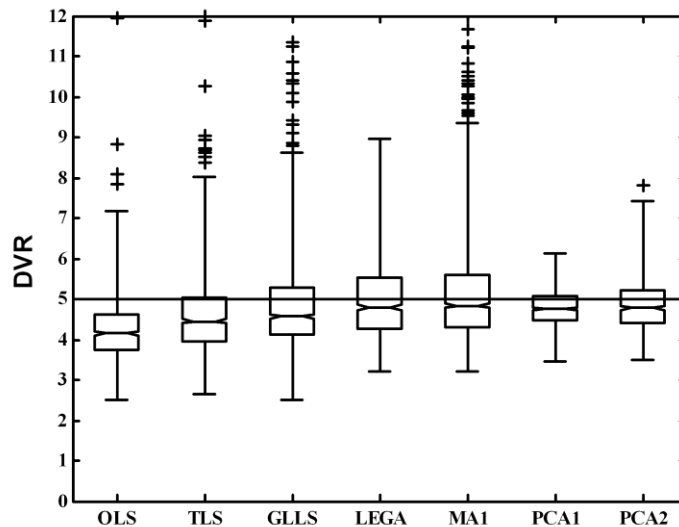


**Figure 3.8:** Box plot comparisons of the DVR estimates obtained using the existing and proposed bias removal methods for single measurement studies simulated to include a blood volume component, but analyzed ignoring the vascular contribution (true  $DVR=5$ ). The trends are similar to those seen in Figure 7 but include a consistent but minimal bias ( $< 5\%$ ) as compared to the noise induced bias in OLS ( $>10\%$ ).

Similar trends to those seen in Figures 3.3 - 3.8 were seen for simulations of different levels of noise (results not shown).

### **3.5 Human Studies:**

#### **3.5.1 Human Studies design**

To apply the proposed approach in single measurement human PET studies, 12 subjects were imaged with [ $^{11}\text{C}$ ]CFN for 70 minutes and binned into 16 frames (4 x 0.5 min, 3 x 1 min, 2 x 2.5 min, 2 x 5 min, 5 x 10 min). All scan were performed on a Siemens ECAT Exact HR+ scanner. Images were reconstruction following Fourier rebinning (FORE) using 2D-OSEM, 4 iterations 16 subsets and no post-process smoothing resulting in images with isotropic resolution of approximately 6 mm FWHM. Injected doses of [ $^{11}\text{C}$ ]CFN were 555-666 MBq (15-18 mCi) at a specific activity of >2000 Ci/mmol. CFN was administered as partial bolus followed by continuous infusion. Subject motion across frames was corrected using Neurostat (University of Michigan; (Minoshima et al. 1994; Minoshima et al. 1993). VOIs, including the occipital cortex reference region, were obtained using a standardized VOI template following reorientation and non-linear warping to the stereotactic Talairach atlas (Talairach and Tournoux 1988) using Neurostat routines. DVR parametric images were obtained by the proposed and all existing methods. The PCA training set consisted of TACs from all the individual voxels in the brain volume and was used to obtain the principal components for each subject. The system matrix was then constructed using the first ' $q$ ' principal components (' $q$ ' selected from simulations). All individual voxel TACs in the image volume were then fitted to the system matrix to obtain smooth TACs with reduced noise. DVR values were estimated by substituting these smoothed TACs values in place of the noisy TACs values in the denominators of Equation 2.11. DVR estimates were also obtained employing the existing bias removal methods and compared with the proposed PCA approach.

### 3.5.2 Human Studies Results

For the 12 human scans in the single-measurement case, 8 regions of interest (ROIs) were placed on the estimated DVR images of each subject obtained from all methods. The means of DVR values and means of the standard deviations within these regions from 12 subjects are reported in Table 3.3. The top 50 percentile pixels in these ROIs were used to obtain the statistics. The performance of the methods in the human data was seen to match closely with the performance in simulation studies. TLS estimates are higher but quite close to that of OLS for all regions. The estimates of GLLS, LEGA, PCA1, PCA2 and PCA3 are higher than OLS as seen in single measurement simulation studies indicating reduction in bias. Mean values for MA1 are higher than the other methods due to the presence of outliers. The means of the standard deviations (across-subject means of the within-region standard deviations) also follow the same trend as seen in simulations with PCA1 having the lowest and MA1 having the highest variance compared to the other methods. It is important to note that in general the PCA method yields the smallest standard deviations, which is a strength of the approach.

**Table 3.3:** Mean DVR (mean standard deviation) in subjects imaged with the single measurement protocol (n = 12).

	Thalamus	Dorsal Caudate	Ventral Caudate	Amygdala	Anterior Cingulate	Cortex	Cerebrum	Occipital Cortex
<b>OLS</b>	2.68 (0.23)	2.51 (0.48)	2.82 (0.42)	2.56 (0.53)	1.79 (0.54)	1.52 (0.22)	1.68 (0.18)	1.10 (0.22)
<b>TLS</b>	2.74 (0.26)	2.55 (0.63)	2.92 (0.47)	2.70 (0.69)	1.81 (0.71)	1.53 (0.25)	1.69 (0.20)	1.10 (0.23)
<b>GLLS</b>	2.83 (0.24)	2.62 (0.43)	3.05 (0.39)	2.85 (0.45)	1.85 (0.39)	1.56 (0.22)	1.73 (0.19)	1.12 (0.22)
<b>LEGA</b>	2.90 (0.37)	2.68 (0.68)	3.18 (0.59)	2.98 (0.85)	1.89 (0.83)	1.61 (0.34)	1.78 (0.34)	1.17 (0.31)
<b>MA1</b>	3.13 (1.33)	3.44 (2.95)	3.25 (2.27)	3.15 (3.54)	1.92 (3.69)	1.67 (1.43)	1.78 (1.28)	1.24 (1.10)
<b>PCA0</b>	2.64 (0.17)	2.49 (0.21)	2.71 (0.17)	2.39 (0.24)	1.86 (0.14)	1.54 (0.17)	1.78 (0.11)	1.07 (0.16)
<b>PCA1</b>	3.03 (0.22)	2.77 (0.35)	3.30 (0.31)	3.16 (0.38)	1.89 (0.31)	1.59 (0.20)	1.77 (0.16)	1.11 (0.23)
<b>PCA2</b>	2.87 (0.24)	2.64 (0.43)	3.06 (0.38)	2.83 (0.45)	1.88 (0.44)	1.58 (0.22)	1.75 (0.19)	1.12 (0.23)
<b>PCA3</b>	2.87 (0.26)	2.63 (0.51)	3.06 (0.45)	2.83 (0.59)	1.88 (0.55)	1.58 (0.24)	1.75 (0.21)	1.12 (0.23)

Mean standard deviation is the across-subject mean of the within-region standard deviation.



### 3.6 Discussion and Conclusion

The negative bias in the DVR estimates from Logan plots is due to the noise in the PET TACs that propagates as correlated errors in dependent and independent variables of the Logan plot equation. While several methods for reducing this bias have been proposed, these methods either remove only a portion of the bias, or reduce bias at the expense of precision. Parameter estimation by TLS removes only a portion of the bias. The GLLS, LEGA and MA1 methods are quite effective in removing bias, but demonstrate poorer precision, especially for intervention studies where two DVR estimates are required as will be seen in the next chapter. In the proposed approach, fitting the dynamic PET data to a low-dimension PCA-based linear model maintains the appropriate kinetic shape of the TACs while removing noise and hence the source of the correlated errors in the Logan plot equation. This provides DVR estimates with minimal bias and reduced variance. In single measurement simulation studies, the linear combination of just two curve shapes (the mean vector and first principal component) was successful in modeling the simulated test data curves sampled from the training set and reduced bias and variance associated with their DVR estimates. If a test data curve was not part of the training set, PCA1 was insufficient to model it leading to bias in DVR estimates as seen for the atypical curve ( $\text{DVR} = 8$ ). In human studies, however, TACs from all the voxels in the image volume are used as training data to obtain the PCA-based linear model. A region of unusual kinetics, if present, will contribute to the total TACs in the training data. Thus, a region of unusual kinetics contributing as few as 1% of the total TACs to the training data was simulated. By including curve shapes similar to the one with  $\text{DVR} = 8$  in the training set (1% of total curves), the bias in DVR estimates was reduced but not completely removed. Small regions with atypical TACs, if identified prior to DVR estimation, could be fitted with PCA2 where bias will be removed at the expense of precision.

Adding another component to the PCA1 model (PCA2) also removed bias, but increased the variance of the DVR estimates to a level comparable to OLS. Though the increase in variance between PCA1 and PCA2 is expected due to an increase in degrees of freedom, the magnitude of this increase will vary from tracer to tracer and will depend

upon the particular curve shapes under consideration, and thus needs to be evaluated for each radiotracer application.

Another source of bias, unrelated to the noise-induced bias, exists for reference region approaches due to lack of accounting for the blood-borne component of the PET signal. This was observed to cause a small but consistent bias in all the methods, but was minor compared to the noise induced bias in OLS.

It should be pointed out that in both the simulation studies and the human scans, we used a partial bolus followed by continuous infusion for administration of the radiotracer. This may reduce the kinetic complexity of the TACs compared to bolus injection studies, and hence limit the number of principal components required to describe the shape of the TACs. When applying the PCA approach to other PET ligands or radiotracer administration protocols, the optimal number of components for describing the TAC shapes needs to be reevaluated. However in our experience, the mean vector plus at most two principal components seem sufficient for modeling standard single-measurement PET studies for most radiotracers, while the mean vector plus at most three components are sufficient for interventional PET studies described in Chapter 4 that may have more complex kinetic behavior.

Obtaining the components from training data has a closed form solution and hence is not computationally expensive. While the simulation studies are a necessary step in the validation of any new proposed approach, the final evaluation must involve real data. Results in Tables 3.3 clearly demonstrate the utility of the PCA approach in human data.

The proposed PCA method is simple to implement and computationally fast. For relatively slowly equilibrating tracer like [ $^{11}\text{C}$ ]CFN, PCA1 produced DVR images which had less bias, lower variance, or both compared to existing bias removal methods.

The motivation for this thesis is the measurement of multiple neuropharmacological aspects of the brain. The noise induced bias in TACs accentuates the bias problem in the dual-Logan intervention studies since a limited number of data points are available for DVR measurement. The improvement in Logan plot analysis shown in this chapter provides the performance necessary for application to dual-measurement studies. In the next chapter, we see how the proposed and existing methods

perform in case of dual-measurement intervention studies where pre- and post-challenge DVR estimates are required.

## Chapter 4

### Dual-measurement Intervention Studies

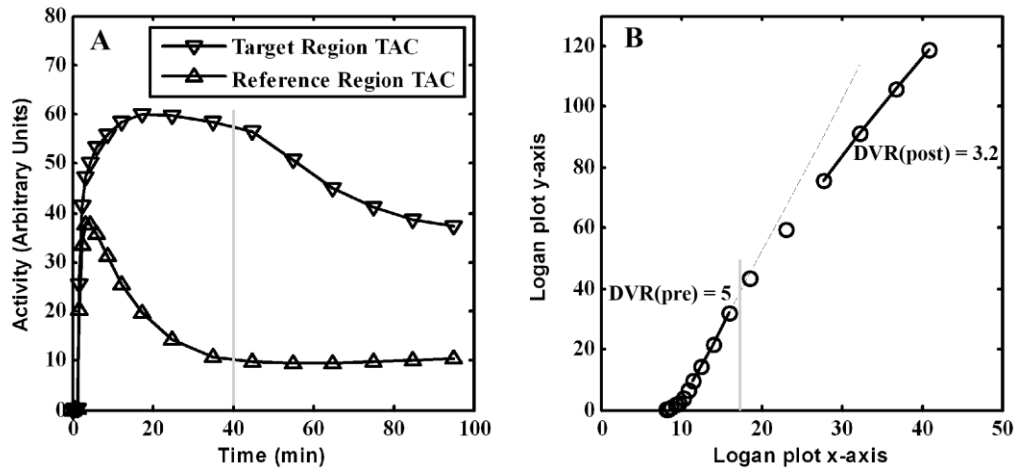


**Figure 4.1:** Dual-measurement approach to measure the *in vivo* distribution of the radiotracer before and after perturbation of the system in a single tracer PET study. In the schematic shown in panel A, perturbation of the system is made 40 min after the tracer administration decreasing the binding potential of the target region by 50% (noiseless case). Logan plots are used to estimate DVR both before and after the intervention. The grey lines indicate the point at which the perturbation occurs.

PET intervention studies are used to investigate the effect of a pharmacological or behavioral challenge on the biological system of interest. In a traditional PET intervention study protocol, the baseline pharmacological or behavioral measure of interest is first obtained from a single-tracer PET scan. The baseline scan is followed by the intervention and then another PET scan is acquired with the intention of measuring the effect of the intervention. Typically, each study would also involve invasive arterial sampling.

In this chapter we propose a single-scan intervention study without the need for arterial sampling. In this protocol, the tracer is administered and at some point during the same acquisition a perturbation of the system is made with the intent of changing *in vivo*

distribution of the radiotracer (Figure 4.1, panel A). Reference region based Logan plots are used to estimate DVR before and after intervention (Figure 4.1, panel B).

We have found that the noise induced bias in DVR (discussed in Chapter 3) is more pronounced in dual-measurement studies resulting in higher bias and variance than in single-tracer PET studies due to the restricted temporal range of data available for DVR estimation. Application of the existing bias removal techniques to such intervention studies has not been reported in the literature. Except for the temporal range of data used, the procedure for estimating DVR in dual-measurement intervention and single measurement studies is the same. The Logan plots for dual-measurement studies have the same noise induced bias associated with them as in single measurement studies. Thus, though the existing methods have been proposed for single measurement studies, they are applicable to the dual Logan case without any modifications.

In this chapter we apply the PCA-based approach as well as existing bias reduction methods (see chapter 3) to dual-measurement PET for both simulation studies (Section 4.1) and human scans (Section 4.2).

## **4.1 Simulation studies**

### **4.1.1 Simulation studies: Design**

Intervention studies were simulated using the same input function and rate parameters as in Section 3.2.1 (Table 3.1), but with a naloxone intervention simulated 40 minutes after initiation of the scan. The simulated data consisted of 100 minutes - 19 frames scan (4 x 0.5 min, 3 x 1 min, 2 x 2.5 min, 2 x 5 min, 8 x 10 min.), which is the same protocol as used for the human intervention scans. The training set consisted of TACs with a linear drop in  $k_3$  to 40%, 50%, and 60% of the initial  $k_3$  value over the 10 minute period after the intervention to model the loss in available binding sites following naloxone intervention. The test set was simulated with 50% drop in  $k_3$ . DVR values were estimated from Logan plots using ‘early’ data from 20 – 40 min for pre-intervention DVR ( $DVR_{pre}$ ) and ‘late’ data from 60 min until end of scan data for post-intervention DVR ( $DVR_{post}$ ) as shown in Figure 4.1, panel B (noiseless case).  $DVR_{pre}$  is estimated

from 20 – 40 min when the Logan plot has become linear. The perturbation at 40 min (denoted by the vertical grey line) increases receptor occupancy causing the Logan plot to bend (40 – 60 min), before becoming linear again around 60 min. The 60 – 100 min period can be used to estimate  $DVR_{post}$ . For both  $DVR_{pre}$  and  $DVR_{post}$  estimations, the integral terms in the numerators of Equation 2.11 are calculated from the beginning of the scan.

As mentioned before, the existing methods, though proposed for single measurement studies are also applicable to dual-measurement intervention studies. Though this is true for GLLS as well, some practical difficulties exist. To apply the GLLS method as proposed in Logan et. al, 2001 to the dual-measurement case, temporal segments of the TAC before and after intervention may have to be further cleaved into 2 parts each. This, though possible, is not practical due to a limited number of points in the TACs (11 pre-intervention and 6 post-intervention). Thus, we implemented GLLS without dividing the segments before and after intervention any further. It should be noted that in order to fairly compare this method to the others, the segments before and after intervention may need to be separated further (work not done).

#### **4.1.2 Simulation studies: Results**

Similar analyses as shown in Figures 3.3 – 3.8 were performed for intervention studies to determine the appropriate number of principal components for fitting the noisy data. Figure 4.2 shows percent absolute bias versus percent standard deviation in the DVR estimates for both pre-intervention ('true'  $DVR_{pre} = 5$ ; filled symbols) and post-intervention ('true'  $DVR_{post} = 3$ ; open symbols) data. Since the bias in the estimated DVR values is higher for larger DVR values, in general the bias is higher in  $DVR_{pre}$  than  $DVR_{post}$ . It can be seen that PCA1(pre) and PCA3(post) provide the best bias-variance trade-off (by virtue of their proximity to the origin) than all the other methods. In fact DVR estimates using all PCA-based approaches tested (PCA1, PCA2 and PCA3) cluster close to the origin, reducing bias while maintaining good precision. All the existing bias removal methods reduce bias at the expense of precision. Thus, as for single-tracer studies, the PCA approach appears to be the method of choice for dual-measurement

simulation studies as well. Next, we validate the method in human dual-measurement studies.

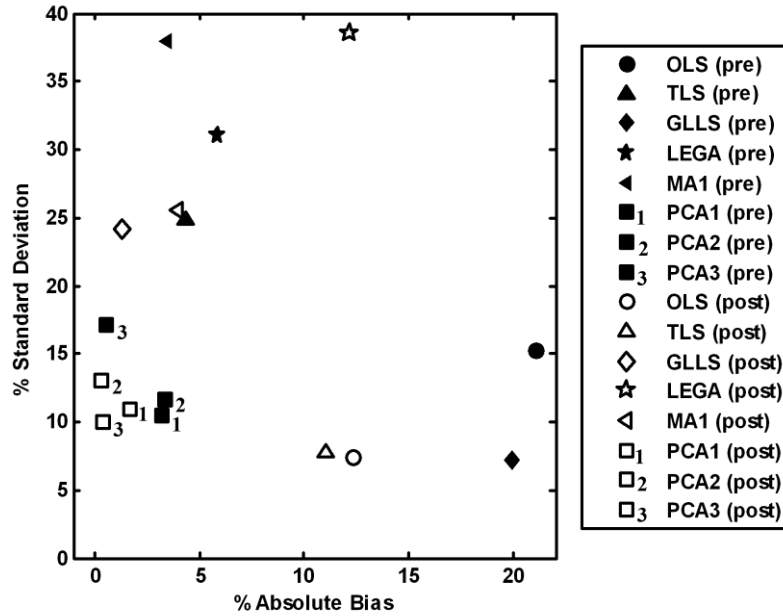


**Figure 4.2:** Trade-off between bias and precision for the existing and proposed bias in simulated intervention studies (discarding top and bottom 2.5 percentiles). The figure shows the percent standard deviation versus percent absolute bias in  $DVR_{pre}$  (filled symbols) and  $DVR_{post}$  (open symbols) for the simulation studies where the binding density was decreased by 50% post-intervention. ‘True’ DVR pre-intervention and post-intervention was 5 and 3 respectively. OLS showed the maximum bias as was seen in the single measurement studies. All the PCA-based methods (PCA1, PCA2 and PCA3) cluster close to the origin and reduce bias while maintaining good precision. The existing bias removal techniques reduced the bias at the expense of increase in variance.

## 4.2 Human data studies

### 4.2.1 Human studies: Design

To apply the proposed approach in dual-measurement intervention studies, scans were performed in four human subjects using  $[^{11}C]CFN$  with a naloxone dose given starting 40 minutes after CFN administration to block tracer binding. Naloxone was administered as a 0.004 mg/Kg bolus followed by 0.00004 mg/Kg/min for the remainder of the study, a dose designed to block approximately 50% of the specific binding sites. Four control subjects were also imaged where no intervention was given during the scan, and thus no change in binding was expected between ‘early’ and ‘late’ DVR estimates.

Data for these 8 subjects were collected as for the single-measurement studies except that scans were acquired for 100 minutes and binned into 19 frames (4 x 0.5 min, 3 x 1 min, 2 x 2.5 min, 2 x 5 min, 8 x 10 min). Except for the temporal range of data used, the procedure for estimating DVR using the proposed and existing methods in intervention studies is same as that for single measurement studies as explained above.

#### 4.2.2 Human data: Results

Figure 4.3 shows DVR images obtained from data before and after 40 minutes of scanning in one of the control subjects where no intervention was given, hence  $DVR_{pre}$  and  $DVR_{post}$  images should be identical. The OLS, TLS and GLLS methods showed a decrease in global DVR though no receptor blocking was present. The LEGA and MA1 methods yielded noisy DVR images, especially for the ‘late’ measure, and hence should not be used to create parametric images in intervention studies. PCA1 images showed little to no change between ‘pre’ and ‘post’ images and did not exhibit any bad fits. PCA2 and PCA3 images exhibited higher variance, but showed little to no change between early and late DVR images.

To quantify these effects, scatter plots of pre and post binding potential estimates for voxels with receptor binding ( $DVR > 1$ ) were made for all subjects and the mean values of correlation coefficient, slope and intercept reported in Table 4.1 ( $n = 4$  for both groups). Since errors exist in both abscissa and ordinate, the regression slopes and intercepts were estimated using total least squares optimization. For the control cases, the ideal estimator will have correlation coefficient = 1 and slope = 1 with intercept at the origin indicating no variance and no change in occupancy. PCA1 behaves closest to the ideal estimator for the control case. The other methods show lower correlations and slopes less than 1 indicating higher variance and an apparent change in occupancy due to higher bias in ‘late’ than in ‘early’ DVR estimates.

Figure 4.4 shows DVR images before and after intervention in one of the subjects who received naloxone. Noise properties of DVR images are similar to those in the no intervention case. OLS, TLS and GLLS show the expected decrease but are noisier. Similar to the results in the control study, LEGA and MA1 images are much noisier and



would have limited utility for intervention studies. PCA1 images show the lowest variance and exhibit the expected decrease in DVR values. PCA2 and PCA3 again have higher variance, but show the expected effects of naloxone on DVR estimates. The results for scatter plots in the naloxone intervention cases are summarized in Table 4.1 (right columns). The PCA-based methods have higher correlations than the other methods and the mean slope for PCA1 = 0.54 corresponds well with the expected ~50% occupancy of receptor sites at the chosen naloxone dose.

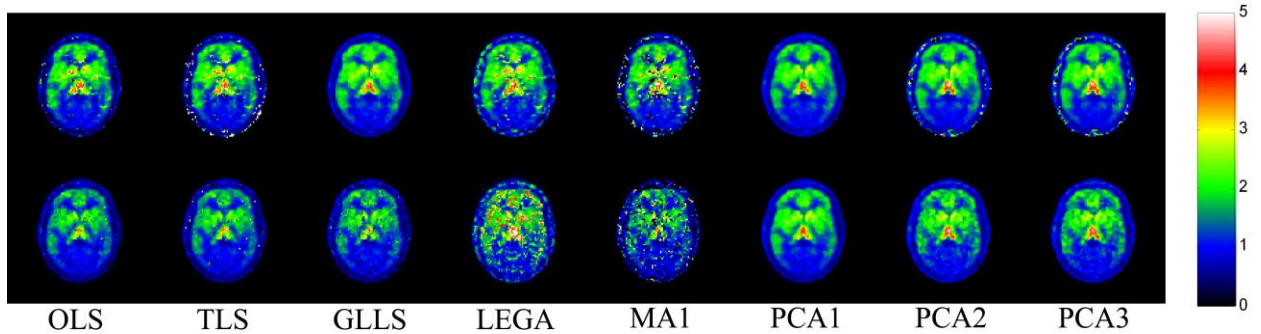


**Figure 4.3:** DVR images from a representative control subject estimated from data before and after 40 minutes with no intervention. OLS, TLS and GLLS show a decrease in global DVR values despite there being no intervention. LEGA and MA1 give very noisy results. PCA1 yields images with high precision for both ‘pre’ and ‘post’ estimation periods with no noticeable difference in binding magnitudes between the two estimations.

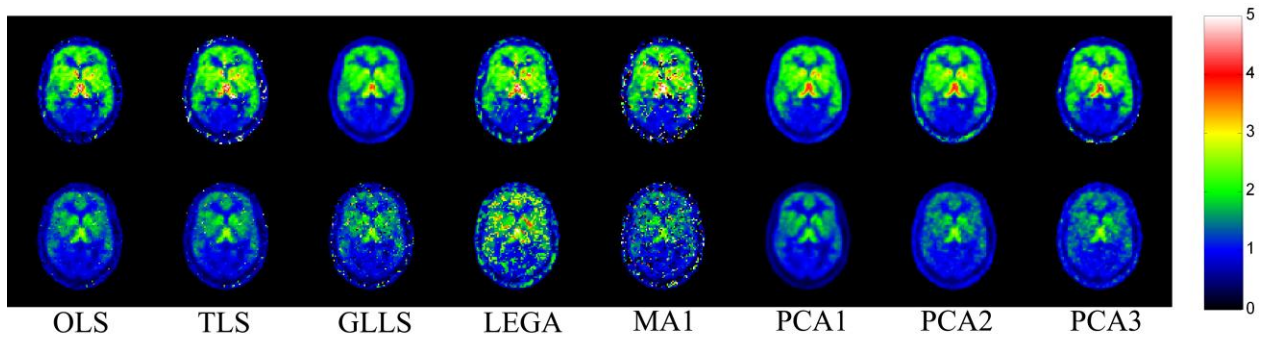


**Figure 4.4:** DVR images from a representative subject from scan data before and after injecting naloxone (40 minutes after the beginning of radiotracer administration). OLS, TLS and GLLS show the expected decrease in global DVR values but lack precision in voxel-wise estimates. As in the control study, LEGA and MA1 yield images that are very noisy. PCA1 produces high precision images for both early and late data and showed the expected decreases in binding values due to naloxone.

The performance of each method varied little from subject to subject as seen by the small across subject standard deviation values for the mean statistics as reported in

Table 4.1. The performance of all methods depends primarily on the noise level in the TACs (higher bias and variance with higher noise). Since all the subjects were imaged with the same PET scanner; the noise level in all scans was similar and hence, so was the performance of each method from subject to subject.

**Table 4.1:** Mean correlation coefficient and mean slope and mean intercept of the scatter plots of the early and late  $BP_{ND}$  estimates in control subjects (n=4) with no intervention and in subjects with naloxone intervention (n=4).

	No Intervention (Control)			With Naloxone Intervention		
	Correlation Coefficient	Slope	Intercept	Correlation Coefficient	Slope	Intercept
<b>OLS</b>	0.83 (0.02)	0.82 (0.06)	-0.01 (0.02)	0.75 (0.04)	0.44 (0.03)	0.05 (0.03)
<b>TLS</b>	0.80 (0.02)	0.81 (0.08)	-0.01 (0.03)	0.73 (0.04)	0.41 (0.03)	0.06 (0.03)
<b>GLLS</b>	0.84 (0.01)	0.99 (0.08)	-0.12 (0.03)	0.84 (0.03)	0.66 (0.02)	-0.08 (0.01)
<b>LEGA</b>	0.57 (0.07)	1.41 (0.25)	-0.33 (0.17)	0.44 (0.05)	1.01 (0.54)	-0.38 (0.43)
<b>MA1</b>	0.28 (0.04)	2.18 (0.74)	-0.96 (0.59)	0.13 (0.05)	0.30 (0.24)	0.22 (0.25)
<b>PCA1</b>	0.99 (0.00)	0.96 (0.04)	-0.02 (0.01)	0.93 (0.03)	0.54 (0.04)	-0.15 (0.04)
<b>PCA2</b>	0.91 (0.06)	0.96 (0.04)	-0.04 (0.02)	0.84 (0.09)	0.51 (0.03)	0.08 (0.01)
<b>PCA3</b>	0.89 (0.04)	0.93 (0.06)	-0.03 (0.02)	0.80 (0.09)	0.43 (0.04)	-0.00 (0.04)

The values in the brackets are standard deviations for the reported statistics. A total least squares optimization was used to calculate the regression slope and intercept since errors exist in both abscissa and ordinate measures.

### 4.3 Discussion and Conclusion

Dual-measurement intervention studies discussed in this chapter make it possible to measure both baseline and post-intervention binding site densities in a subject from a *single* PET acquisition, and *without* the need for arterial sampling. The negative bias in

the DVR estimates using Logan plots due to the noise in the PET TACs is seen to a greater extent in dual-measurement studies. While several methods for reducing this bias have been proposed, these methods (as with single measurement studies) either remove only a portion of the bias, or reduce bias at the expense of precision. PCA-based linear models reduce bias without increasing variance also similar to the single-tracer case shown in Chapter 3.

Results presented in Table 4.1 and in figures 4.3 and 4.4 clearly demonstrate the utility of the PCA for intervention studies as PCA is the only approach that produced voxel-by-voxel parametric images with acceptable noise levels and with little observable bias. Figure 4.3 shows that for the no ‘intervention’ case, only PCA1 yielded ‘early’ and ‘late’ DVR values that were of the same magnitude and of the same statistical quality. A similar advantage of PCA1 over the other methods for the ‘intervention’ case is seen in Fig. 4.4, with the expected naloxone-induced decrease in DVR. Scatter plots of pre- vs. post-intervention binding potential estimates show that PCA-based methods yield the highest correlation and have closer to the expected slopes compared to the other methods (Table 4.1). These results show both the sensitivity and specificity of the PCA-based approach. PCA1 produced unchanged ‘early’ and ‘late’ measures when no intervention was given, and also demonstrated the ability to detect intervention induced changes when present. PCA1, however, might not have the necessary degrees of freedom to model very large displacements. PCA2 or PCA3 will capture these larger displacements, but at the expense of higher variance.

Thus, advantages of the PCA approach were seen not only for standard single measurement PET studies in Chapter 3, but were especially impressive when applied to dual measurement intervention studies where pre- and post-challenge DVR estimates are required.

## Chapter 5

### Dual-Tracer Studies: Theory and Simulations

Another multiple neuropharmacological measurement protocol undertaken in this work is the dual-tracer study protocol where, two tracers are injected in the same scan separated closely in time. This and the next chapter discuss development of improved methods for noninvasive parameter estimation in dual-tracer studies and their application in simulation studies and human scans acquired without arterial sampling.

A single neurochemical marker is often insufficient to fully characterize a neurological disease and information on multiple neuropharmacological systems is of interest. By studying two different aspects of a subject's neuropharmacology with a dual-tracer PET scan, we may be able to have a better understanding of a disease. However, since PET is based on measuring the 511 KeV photons emitted by positron annihilations, there is no direct way to separate the signals from the two tracers using differing energy windows. The radiotracer signals must be separated based on characteristics such as half-life, tracer kinetics, or the measurements of the first tracer (Tracer *I*) prior to the injection of the second tracer (Tracer *II*). Very early work on dual-tracer PET studies in phantoms by Huang et al. (1982) described a technique for separating tracers with different half lives. Koeppe et al. (2001) reported the first results of dynamic dual-tracer studies in humans using  $^{11}\text{C}$ -labeled tracers. In that work, a parallel-model, simultaneous-fitting approach was applied to estimate the parameters of both tracers using metabolite-corrected arterial plasma input functions. It was shown that under many conditions the statistical quality of the parameter estimates were nearly as good for dual-tracer as for single-tracer scans. Kadrmas and Rust (2005) examined the degree of overlap of information in dual-tracer TACs in a simulation study using principal component analysis (PCA). They applied a parallel fitting approach similar to that in (Koeppe et al. 2001)

using both arterial input function models and PCA-based models. These rapid dual-tracer methods were explored in simulation studies for measuring hypoxia and blood flow (Rust and Kadmas 2006) and for tumor characterization using  $^{62}\text{Cu}$ -PTSM and  $^{62}\text{Cu}$ -ATSM in dogs with spontaneously-occurring tumors (Black et al. 2008). This existing body of work on dynamic dual-tracer PET described above requires arterial blood sampling and thus has various practical difficulties as mentioned earlier, such as requiring metabolite corrections of the arterial blood samples and being more invasive for the subject.

The possibility of analysis of dual-tracer studies without arterial sampling was first explored by Koeppe et al. 2004. In this work, we have extended these original efforts, reporting two methods to separate the individual tracer signals and estimate parameters of interest using reference region approaches. The pharmacological indices of interest estimated by applying the two methods to simulated dual-tracer TACs were DVR for reversible tracers, and  $k_3$  (the trapping constant), for irreversible tracers.

## 5.1 Theory of analysis techniques for non-invasive dual-tracer studies

The proposed reference tissue-based dual-tracer approach is applicable to cases where the first tracer injected has a tissue or a region with negligible receptor binding or trapping. We first describe the methods for the case where both injected radiotracers bind reversibly and then extend it to the case where the first tracer has reversible binding and the second tracer has irreversible trapping.

Figure 5.1 shows the compartmental model for a dual-tracer study of two reversible radiotracers consisting of two tissue compartments for each tracer (Tracer *I* and *II*). Each tracer has a unique reference tissue that has a negligible density of specific binding sites and is assumed to have the same equilibrium distribution volume as the non-displaceable compartment of all other regions. In the case of a reversible single-tracer two-tissue compartment model, the target region concentration time courses or time-activity curves (TACs) can be expressed in terms of the model rate constants and reference region concentration time course using the full reference tissue input model (RTM) (Equation 2.6).

The equations (2.6 – 2.9) are for the single tracer case. In a dual-tracer study, two tracers are injected; Tracer *II* injected at time  $t = T'$  after Tracer *I*. The dual-tracer TAC ( $\bar{y}_i$ ) can be represented as:

$$\bar{y}_i = \bar{y}_i^I + \bar{y}_i^{II} + \bar{\varepsilon}_i, \quad - 5.1$$

where  $\bar{y}_i^I$  and  $\bar{y}_i^{II}$  are the constituent individual tracer signals and  $\bar{\varepsilon}_i$  is the noise vector.

The present work investigated two methods to estimate the individual tracer curves ( $\bar{y}_i^I$  and  $\bar{y}_i^{II}$ ) and their parameter vectors ( $\bar{\theta}_i^I$  and  $\bar{\theta}_i^{II}$ ) from the dual-tracer signal  $\bar{y}_i$ : an extrapolation method (EM) and a simultaneous fitting method (SM).

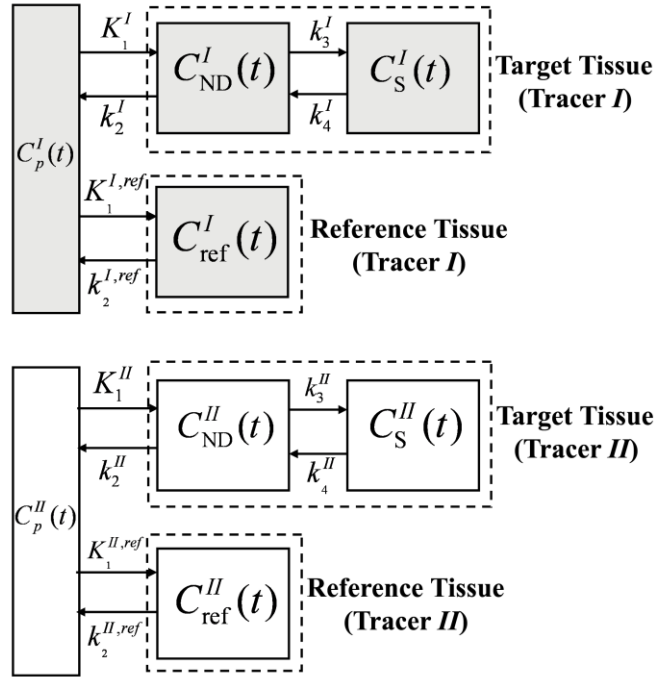


**Figure 5.1:** Two tissue compartmental model for a non-invasive dual-tracer study of two reversible radiotracers (tracers *I* and *II*). Each tracer has a unique reference tissue that has a negligible density of specific binding sites and is assumed to have the same equilibrium distribution volume as the non-displaceable compartment of all other tissues.

The primary assumption in both approaches is that the injection protocol for Tracer *I* brings its reference region ( $\bar{y}_r^I$ ) to steady-state prior to the injection of Tracer *II*. Simply put, the fate of the reference region for Tracer *I* is assumed to be known (and constant) from the injection time of Tracer *II* through the end of the scan despite

“contamination” by the second tracer (Koeppel et al. 2004). The more rapidly reversible Tracer *I* is, the more likely for this key assumption to hold true.

### 5.1.1 Extrapolation Method (EM)

The extrapolation method is based on the original approach reported in Koeppel et al. (2004), where the simplified reference tissue model (sRTM, section 2.4.2) was used to extrapolate the first tracer. It was seen that the simplifying assumption for sRTM (rapid equilibration of free and bound components;  $k_3 \gg 0$  and  $k_4 \gg 0$ ) resulted in biases in the extrapolated tissue curves. Hence, in this work we have used the full reference tissue model (RTM, section 2.4.1) which is a more appropriate model for the tracers used here. Data exclusive to Tracer *I* is known for  $t < T'$ ; the injection time of Tracer *II*. Using this early data, Tracer *I* parameter vector for each voxel  $i$  ( $\bar{\theta}_i^I$ ) could be estimated by minimizing the cost function shown below using a nonlinear estimation algorithm (similar to equation 2.9).

$$\hat{\theta}_i^I = \arg \min_{\bar{\theta}_i^I} \left\| W \{ \bar{y}_i^I - f(\bar{y}_r^I, \bar{\theta}_i^I) \} \right\|_2^2 \quad - 5.2$$

However, this minimization requires nonlinear estimation of four parameters from just 20 min of data which gave noisy estimates. To counter this problem, the parameter-of-interest (DVR) for Tracer *I*, was first estimated by the PCA-based Logan analysis (Joshi et al. 2008a) from the early data ( $0 < t < T'$ ). Additionally, the  $k_4$  parameter for Tracer *I* was fixed to the population average to improve the precision of the estimates. Using the fixed  $k_4$  and Logan-based  $BP_{ND}$  estimate ( $BP_{ND} = DVR - 1$ ),  $k_3$  can be calculated ( $k_3 = k_4 BP_{ND}$ ). The remaining two unknown elements of the parameter vector  $\bar{\theta}_i^I$  ( $R_1, k_2$ ) were estimated using nonlinear least squares from Equation 5.2. Using this parameter vector and the reference region TAC for Tracer *I*, Tracer *I* TACs were extrapolated to the end of scan using the full reference tissue model ( $\hat{y}_i^I = f(\bar{y}_r^I, \hat{\theta}_i^I)$ ). The Tracer *II* component was isolated by subtracting the extrapolated Tracer *I* signal from the dual-tracer TAC for all regions or voxels  $i$  ( $\hat{y}_i^{II} = \bar{y}_i - \hat{y}_i^I$ ). The isolated Tracer *II* curves ( $\hat{y}_i^{II}$ )

also include the reference region curve for Tracer *II* ( $\hat{y}_r^{II}$ ) and hence, all the information to estimate the parameter vector ( $\hat{\theta}_i^{II}$ ) for Tracer *II* using reference region approaches has been obtained. The parameter-of-interest for Tracer *II* (DVR), was estimated by PCA-based Logan analysis.

### 5.1.2 Simultaneous Fitting Method (SM)

A potential drawback of the two-step extrapolation method approach described above is that errors in parameter estimation of Tracer *I* from limited early data propagate into parameter estimates of Tracer *II*. There may be cases where error in Tracer *I* estimates could propagate in such a way as to give physiologically improbable parameter values for Tracer *II*. Thus, as an alternative to the two-step extrapolation method, we also explored a one step approach where the parameters of both tracers were estimated at the same time by fitting the dual tracer TACs simultaneously to the reference tissue models of both tracers.

This simultaneous fitting method (SM) attempts to estimate the model parameters for both tracers using one minimization operation. We first applied the extrapolation method to the dual-tracer curve of Tracer *II* reference region alone, to isolate Tracer *II* reference region curve ( $\hat{y}_r^{II}$ ). The tracer *I* reference region TAC ( $\bar{y}_r^I$ ) is known by virtue of the primary assumption. Using the reference region curves for both tracers, the voxel-wise parameter vectors for both the tracers can be estimated simultaneously by minimizing the following cost function:

$$(\hat{\theta}_i^I, \hat{\theta}_i^{II}) = \arg \min_{(\theta_i^I, \theta_i^{II})} \left\| W \{ \bar{y}_i - f(\bar{y}_r^I, \bar{\theta}_i^I) - f(\hat{y}_r^{II}, \bar{\theta}_i^{II}) \} \right\|_2^2. \quad - 5.3$$

The primary parameter-of-interest (DVR) for both tracers can now be calculated directly from the estimated parameter vectors  $\hat{\theta}_i^I$  and  $\hat{\theta}_i^{II}$ .

However, direct simultaneous estimation of eight model parameters from Equation 5.3 (four for each tracer) was plagued by noise in the dual-tracer TACs, as well as by non-convergence associated with nonlinear algorithms, leading to low precision in the binding estimates. To improve the precision, the number of parameters was reduced



to six by fixing the  $k_4$  parameter for both tracers to the population average. Furthermore, instead of calculating DVR directly from the estimated model parameters, the individual TACs for both tracers were separated by substituting the estimated parameters vectors  $(\hat{\theta}_i^I, \hat{\theta}_i^{II})$  and reference region curves  $(\bar{y}_r^I, \hat{y}_r^{II})$  into the model equation  $(\hat{y}_i^I = f(\bar{y}_r^I, \hat{\theta}_i^I), \hat{y}_i^{II} = f(\hat{y}_r^{II}, \hat{\theta}_i^{II}))$  and DVR was estimated by applying the robust reference-region based Logan analysis to these separated signals.

### 5.1.3 Using an irreversible tracer as Tracer II

The methods described above were for the case where both the tracers injected bind reversibly, though they can easily be extended to the case where Tracer II has irreversible kinetics. However in the case of an irreversible tracer, the reference region-based model equations for the TACs will be different from that for a reversible tracer (Equation 2.6).

The differential equations for an irreversible two-tissue compartment model are given below ( $k_4^{II} = 0$  in Figure 5.1):

$$\frac{dC_{ND}(t)}{dt} = K_1 C_p(t) - (k_2 + k_3) C_{ND}(t), \quad - 5.4$$

$$\frac{dC_S(t)}{dt} = k_3 C_{ND}(t), \quad - 5.5$$

where  $C_p(t)$  is the arterial plasma input,  $C_{ND}(t)$  is the radioligand concentration in the non-displaceable compartment,  $C_S(t)$  is the radioligand concentration in the specific compartment, and  $K_1$ ,  $k_2$ , and  $k_3$  are the kinetic parameters of the model with  $k_3$ , the trapping constant, being the parameter of interest to be estimated from the dynamic data. In case of the arterial sampling approach, the solution for total tracer concentration in tissue ( $y_i(t) = C_{ND}(t) + C_S(t)$ ) is given below (Herholz et al. 2001):

$$y_i(t) = \frac{K_1 k_2}{k_2 + k_3} \int_0^t C_p(\tau) e^{-(k_2 + k_3)(t-\tau)} d\tau + \frac{K_1 k_3}{k_2 + k_3} \int_0^t C_p(\tau) d\tau, \quad - 5.6$$

where  $C_p(\tau)$  denotes the arterial input function. For the case of an irreversible tracer like [ $^{11}\text{C}$ ]PMP, a different type of reference region approach is needed compared to that used for reversible tracers. The irreversible tracer TAC from a region with an extremely high  $k_3$  value (e.g. striatum for [ $^{11}\text{C}$ ]PMP) is assumed to equal the time integral of the arterial input function multiplied by the transport rate constant of the reference region,  $K_1^{ref}$  (Herholz et al. 2001; Nagatsuka et al. 2001; Nagatsuka Si et al. 2001):

$$y_r(t) = K_1^{ref} \int_0^t C_p(\tau) d\tau. \quad - 5.7$$

Equation 5.7 was rearranged to get an expression for the arterial input function in terms of the reference region curve as shown below:

$$C_p(t) = \frac{1}{K_1^{ref}} \frac{dy_r(t)}{dt}. \quad - 5.8$$

The differentiation operation in equation 5.8 was performed by interpolating the reference region curve on a fine grid followed by numerical differentiation. Substituting the expression for  $C_p(t)$  obtained from equation 5.8 in equation 5.6 yielded:

$$y_i(t) = \left(\frac{K_1}{K_1^{ref}}\right) \frac{k_2}{k_2 + k_3} \int_0^t \frac{dy_r(\tau)}{d\tau} e^{-(k_2+k_3)(t-\tau)} d\tau + \left(\frac{K_1}{K_1^{ref}}\right) \frac{k_3}{k_2 + k_3} y_r(t), \quad - 5.9$$

which expresses the target tissue curve in terms of the reference tissue curve and the rate parameters for irreversible tracers and is equivalent to equation 2.6 for reversible tracers.

Using the notation derived for reversible tracers, the TAC for an irreversible tracer can be expressed as  $\bar{y}_i = f(\bar{y}_r, \bar{\theta}_i) + \bar{\varepsilon}_i$ , where  $\bar{y}_i$  is the tissue TAC,  $\bar{y}_r$  is the reference region curve,  $\bar{\theta}_i = [R_1, k_2, k_3]_i$  is the parameter vector for irreversible tracers and the function  $f$  is reference tissue model of equation 5.9.

After signal separation, the parameter of interest for the irreversible tracer ( $k_3$ ) was estimated by the reference-region based linear least squares method (RLS) (Nagatsuka et al. 2001). The operational equation of RLS is shown below.

$$\bar{y}_i(T) = \rho_1 \bar{y}_r(T) + \rho_2 \int_0^T \bar{y}_r(\tau) d\tau + \rho_3 \int_0^T \bar{y}_i(\tau) d\tau, \quad - 5.10$$

where  $\rho_1, \rho_2$  and  $\rho_3$  are the coefficients of the linear model above and  $k_3 = \rho_2 / \rho_1$ .

Next, we will apply the noninvasive dual-tracer analysis methods described above to dual-tracer simulation studies.

## 5.2 Simulation Design

Model parameters for the simulation studies were selected to mimic PET radiotracers already well characterized at our institution: [ $^{11}\text{C}$ ]flumazenil ([ $^{11}\text{C}$ ]FMZ), a benzodiazepine receptor antagonist (Holthoff et al. 1991; Koeppe et al. 1991), [ $^{11}\text{C}$ ]dihydrotetrabenazine ([ $^{11}\text{C}$ ]DTBZ), a ligand for the VMAT2 binding site (Koeppe et al. 1999a; Koeppe et al. 1996) and [ $^{11}\text{C}$ ]N-methylpiperidinyl propionate ([ $^{11}\text{C}$ ]PMP), a substrate for acetylcholine esterase (Koeppe et al. 1999b). Two types of simulation experiments were undertaken; i) dual-tracer scans mimicking [ $^{11}\text{C}$ ]FMZ and [ $^{11}\text{C}$ ]DTBZ-like tracers where both the tracers injected were reversible and ii) dual-tracer scans mimicking [ $^{11}\text{C}$ ]FMZ and [ $^{11}\text{C}$ ]PMP-like tracers where the second tracer injected was irreversible.

### 5.2.1 [ $^{11}\text{C}$ ]FMZ - [ $^{11}\text{C}$ ]DTBZ dual-tracer simulations

In this study an 80 min scan was simulated where a [ $^{11}\text{C}$ ]FMZ-like radiotracer (Tracer *I*) was injected 20 minutes prior to a [ $^{11}\text{C}$ ]DTBZ-like radiotracer (Tracer *II*). Six hypothetical regions were simulated with kinetic parameters shown in Table 5.1. Region 6 with pons-like kinetics and Region 3 with occipital cortex-like kinetics act as reference regions for Tracer *I* and Tracer *II* respectively (DVR = 1; regions underlined in Table 5.1).

Using the full reference tissue model (equation 2.6) and [ $^{11}\text{C}$ ]FMZ and [ $^{11}\text{C}$ ]DTBZ reference tissue curves from single-tracer human scans; 80 min noise-free single-tracer curves were simulated on a 0.1 min interval for the six regions in Table 5.1. These curves were then binned into 26 frames (4 x 0.5 min, 3 x 1 min, 2 x 2.5 min, 2 x 5

min, 4 x 0.5 min, 3 x 1 min, 2 x 2.5 min, 2 x 5 min, 4 x 10 min) as shown in Figure 5.2 to match dual-tracer acquisitions performed in human studies. All the curves in Figure 5.2 are displayed with decay correction to the start of the experiment. Thus Tracer *II*, which is injected with a 20 min delay (one  $^{11}\text{C}$  half life) after the start of the experiment, has TACs with twice the apparent magnitude relative to the case where Tracer *II* was injected without delay. As required by the main assumption of the methods, it can be seen that the reference tissue for Tracer *I* ( $\text{DVR}_1 = 1$ , Region 6) reaches steady-state prior to injection of the second tracer.

**Table 5.1:** Kinetic parameters used for simulation of 6 hypothetical regions in a dual-tracer study with [ $^{11}\text{C}$ ]FMZ-like and [ $^{11}\text{C}$ ]DTBZ-like reversible tracers.

	Region 1		Region 2		<u>Region 3</u>		Region 4		Region 5		<u>Region 6</u>	
Tracer	<i>I</i>	<i>II</i>	<i>I</i>	<i>II</i>	<i>I</i>	<u><i>II</i></u>	<i>I</i>	<i>II</i>	<i>I</i>	<i>II</i>	<u><i>I</i></u>	<i>II</i>
<b>DVR</b>	<b>6.0</b>	<b>2.0</b>	<b>6.0</b>	<b>4.0</b>	<b>6.0</b>	<u><b>1.0</b></u>	<b>2.5</b>	<b>2.0</b>	<b>1.5</b>	<b>4.0</b>	<u><b>1.0</b></u>	<b>1.5</b>
$\frac{K_1}{K_1^{ref}}$	1.0	1.0	1.0	1.0	1.0	1.0	1.0	1.0	1.0	1.0	1.0	1.0
<b>k<sub>2</sub></b>	0.30	0.133	0.30	0.133	0.30	0.133	0.30	0.133	0.30	0.133	0.30	0.133
<b>k<sub>3</sub></b>	0.75	0.10	0.75	0.30	0.75	0.0	0.30	0.10	0.225	0.30	0.0	0.05
<b>k<sub>4</sub></b>	0.15	0.10	0.15	0.10	0.15	0.0	0.15	0.10	0.15	0.10	0.0	0.10

Regions 6 and 3 are the reference regions for Tracer *I* and Tracer *II* respectively. Parameters-of-interest are shown in bold and reference regions are underlined.

The time-activity curves for Tracers *I* and *II* shown in Figure 5.2 were summed for each of the six regions to obtain noiseless dual-tracer curves. Voxel-level noise was then added to the dual-tracer curves to obtain 1024 noisy realizations. Noisy realizations of single-tracer curves for Tracer *I* and *II* were also simulated to provide a “gold standard” for comparison with results obtained from the proposed dual-tracer estimation methods.

For both extrapolation and simultaneous fitting methods, nonlinear parameter estimation was achieved using MATLAB’s ‘fmincon’ function (Maximum iterations =

100, Function Tolerance =  $10^{-7}$ , Maximum Function evaluations = 1000). The physiologically relevant box constraints used for the nonlinear estimation are:  $\frac{K_1}{K_1^{ref}} \in [0, 3]$ ,  $k_2 \in [0, 1]$  and  $k_3 \in [0, 2]$ . The  $k_4$  parameter was fixed for each tracer to the population average (true value in this case) to make the fit robust by reducing the number of model parameters to be estimated ( $k_4=0.15$  for  $[^{11}\text{C}]\text{FMZ}$ -like tracer and  $k_4=0.10$  for  $[^{11}\text{C}]\text{DTBZ}$ -like tracer).

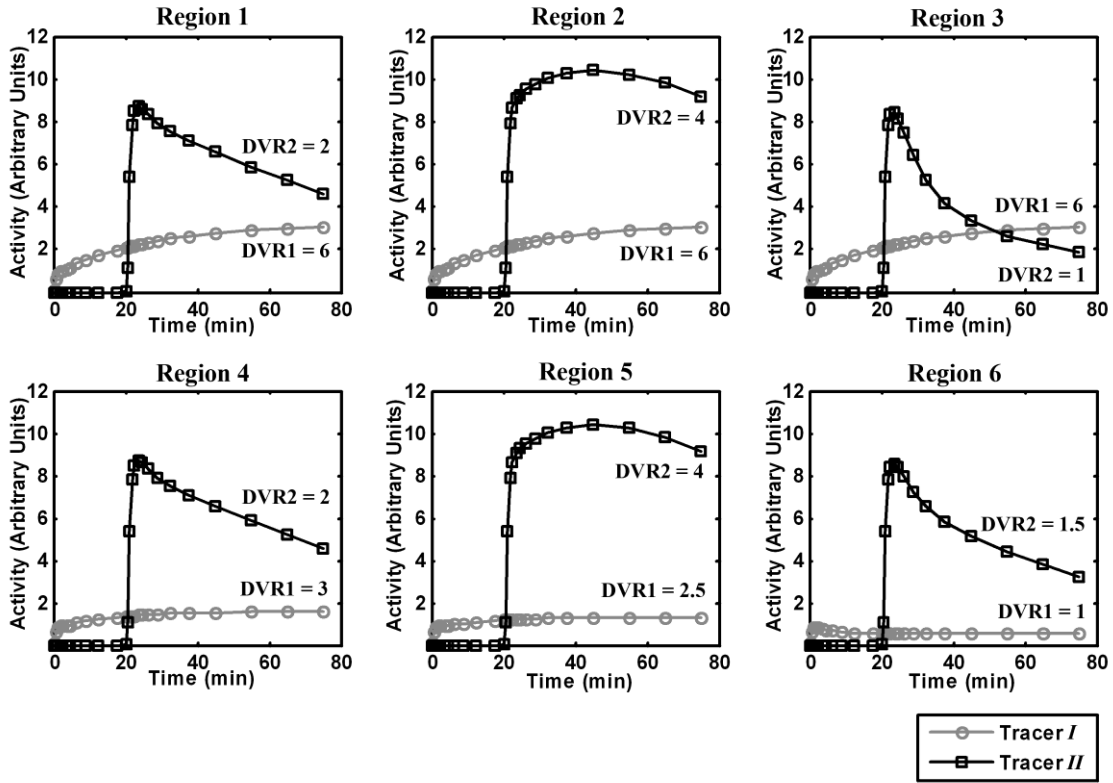


**Figure 5.2:** Noiseless TACs for the six simulated regions for the case where two reversible tracers mimicking  $[^{11}\text{C}]\text{FMZ}$  (Tracer *I*) and  $[^{11}\text{C}]\text{DTBZ}$  (Tracer *II*) are injected 20 minutes apart. The curves shown here have been corrected for radioactive decay from the start of the experiment. Regions 6 and 3 are the reference regions for tracers *I* and *II* respectively.

## 5.2.2 Simulations of assumption failures

The primary requirement for the success of the non-invasive dual-tracer approach is that the Tracer *I* reference region TAC must reach equilibrium before Tracer *II* is

injected. Single-tracer human scans showed that it is possible to attain such equilibrium by appropriate administration protocol (Joshi et al. 2008c). Still, it is important to see how the results will be altered if this assumption is not satisfied. Additional simulations were performed where the reference region TAC of Tracer *I* did not reach steady state by 20 min, but linearly increased or decreased by 20% between 20 min and the end of the scan. The signal separation and parameter estimation was performed assuming that the reference region had in fact reached steady-state and the magnitude of the induced error was calculated.

Another simplification in the methods was fixing the value of  $k_4$  to its population average value during the nonlinear estimation procedure. To check the effect of an incorrect  $k_4$  value on signal separation and parameter estimates, fitting was also performed by fixing  $k_4$  to values  $\pm 20\%$  different than the true  $k_4$  value.

### 5.2.3 [<sup>11</sup>C]FMZ - [<sup>11</sup>C]PMP dual-tracer simulations:

**Table 5.2:** Kinetic parameters used for simulation of 6 hypothetical regions in a dual-tracer study with [<sup>11</sup>C]FMZ-like (reversible) and [<sup>11</sup>C]PMP-like (irreversible) tracers.

	<b>Region 1</b>		<b>Region 2</b>		<b>Region 3</b>		<u><b>Region 4</b></u>		<b>Region 5</b>		<u><b>Region 6</b></u>	
<b>Tracer</b>	<i>I</i>	<i>II</i>	<i>I</i>	<i>II</i>	<i>I</i>	<i>II</i>	<u><i>I</i></u>	<u><i>II</i></u>	<i>I</i>	<i>II</i>	<i>I</i>	<u><i>II</i></u>
<b>DVR</b>	<b>6.0</b>	-	<b>3.0</b>	-	<b>6.0</b>	-	<u><b>1.0</b></u>	-	<b>2.5</b>	-	<b>3.0</b>	-
$R_1$	1.0	1.0	1.0	1.0	1.0	1.0	1.0	1.0	1.0	1.0	1.0	1.0
$k_2$	0.30	0.15	0.30	0.15	0.30	0.15	0.30	0.15	0.30	0.15	0.30	0.15
$k_3$	0.75	<b>0.03</b>	0.30	<b>0.06</b>	0.75	<b>0.10</b>	0.00	<b>0.15</b>	0.225	<b>0.25</b>	0.30	<u><b>2.0</b></u>
$k_4$	0.15	0.0	0.15	0.0	0.15	0.0	0.15	0.0	0.15	0.0	0.15	0.0

Regions 4 and 6 are the reference regions for Tracer *I* and Tracer *II* respectively. Parameters-of-interest are shown in bold and reference regions are underlined.

For [<sup>11</sup>C]FMZ – [<sup>11</sup>C]PMP dual-tracer simulations, six hypothetical regions were simulated having kinetic parameters shown in Table 5.2.

Noiseless curves for  $[^{11}\text{C}]\text{FMZ}$ -like tracer were obtained as described for the  $[^{11}\text{C}]\text{FMZ} - [^{11}\text{C}]\text{DTBZ}$  simulations. For the  $[^{11}\text{C}]\text{PMP}$ -like tracer, noiseless curves were simulated using a true arterial input function from a  $[^{11}\text{C}]\text{PMP}$  human single-tracer scan, the parameters listed in Table 5.2, and equation 5.6. The noiseless TACs for the six simulated regions for each tracer are shown in Figure 5.3.

The procedure to obtain the noisy dual-tracer curves and to separate the dual-tracer signals was identical to that for the  $[^{11}\text{C}]\text{FMZ} - [^{11}\text{C}]\text{DTBZ}$  simulations described earlier. The physiologically relevant box constraints for Tracer *I* ( $[^{11}\text{C}]\text{FMZ}$ -like tracer) are same as those described earlier. The constraints for Tracer *II* ( $[^{11}\text{C}]\text{PMP}$ -like tracer) are:  $R_1 \in [0, 3]$ ,  $k_2 \in [0, 1]$  and  $k_3 \in [0, 3]$  ( $k_4 = 0$  for irreversible  $[^{11}\text{C}]\text{PMP}$ -like tracer). Along with dual-tracer simulations, single-tracer simulations were also performed to provide a “gold-standard” for comparison of dual-tracer results.

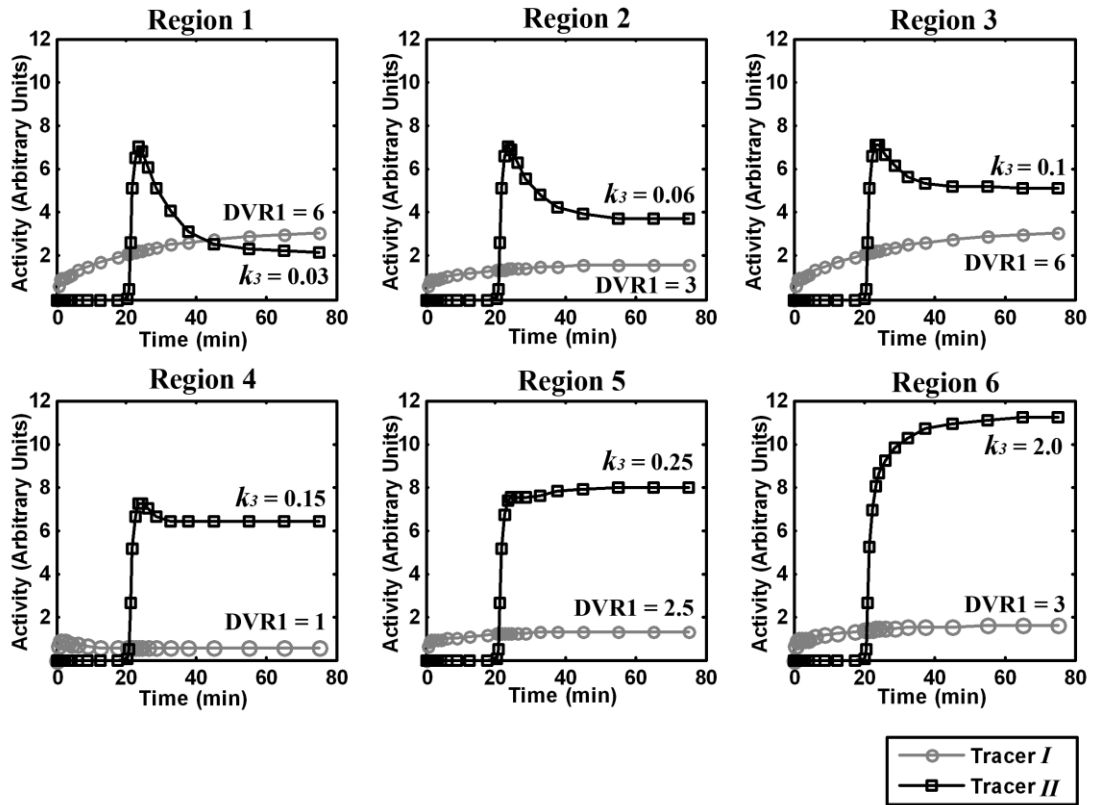


**Figure 5.3:** Noiseless TACs for the six simulated regions for the case where tracers mimicking reversible tracer  $[^{11}\text{C}]\text{FMZ}$  (Tracer *I*) and irreversible tracer  $[^{11}\text{C}]\text{PMP}$  (Tracer *II*) are injected 20 minutes apart. The curves shown here have been corrected for radioactive decay from the start of the experiment. Regions 4 and 6 are the reference regions for tracers *I* and *II* respectively.

## 5.3 Results

### 5.3.1 [<sup>11</sup>C]FMZ - [<sup>11</sup>C]DTBZ dual-tracer simulations

The top portion of Table 5.3 summarizes the results for [<sup>11</sup>C]FMZ - [<sup>11</sup>C]DTBZ simulations where the mean and standard deviation of estimated DVR values for tracers *I* and *II* are reported as percent of true value. The value of 100 (0) denotes no bias and no variance. Row 1 shows the average bias (difference from 100) and standard deviation of Logan-based DVR estimates obtained using ordinary least squares (OLS) for single-tracer simulations (Logan *et al* 1996) which is biased as seen in Chapter 3. To reduce this bias, PCA-based smoothing approach was used (Joshi et al. 2008a).

**Table 5.3:** Bias and standard deviation in DVR estimates and mean % error in separated TACs for [<sup>11</sup>C]FMZ-[<sup>11</sup>C]DTBZ dual-tracer simulations.

	Tracer DVR	Region 1		Region 2		<u>Region 3</u>		Region 4		Region 5		<u>Region 6</u>	
		<i>I</i> 6.0	<i>II</i> 2.0	<i>I</i> 6.0	<i>II</i> 4.0	<i>I</i> 6.0	<i>II</i> <u>1.0</u>	<i>I</i> 2.5	<i>II</i> 2.0	<i>I</i> 1.5	<i>II</i> 4.0	<u><i>I</i></u> <u>1.0</u>	<i>II</i> 1.5
Bias and SD in DVR estimates	OLS (single-tracer)	88 (10)	97 (5)	88 (10)	95 (7)	88 (10)	99 (5)	94 (9)	97 (5)	96 (10)	96 (7)	99 (9)	98 (5)
	PCA (single-tracer)	100 (5)	102 (5)	98 (6)	100 (5)	99 (5)	100 (5)	100 (8)	97 (5)	101 (9)	101 (5)	103 (9)	101 (5)
	EM	68 (23)	113 (13)	68 (21)	107 (9)	67 (22)	126 (20)	81 (17)	102 (6)	85 (15)	98 (6)	99 (10)	98 (6)
	SM	98 (27)	91 (11)	102 (28)	88 (10)	85 (25)	100 (21)	107 (28)	88 (7)	106 (26)	86 (6)	100 (15)	91 (5)
Mean % error in TACs	EM	-29	16	-29	9	-30	40	-17	5	-13	2	1	0
	SM	-1	1	4	-1	-8	11	12	-3	14	-2	9	0

Bias and standard deviation in DVR estimates: a value of 100 denotes no bias. Regions 6 and 3 are the reference regions for Tracer *I* and Tracer *II* respectively (DVR=1; underlined).

Mean % error in TACs: A positive (negative) value indicates a positive (negative) systematic bias in the last 8 frames of the TACs.

The bias present in the OLS Logan analysis (Row 1) was almost completely removed by PCA-based Logan analysis along with an improvement in precision (Row 2). This PCA-based Logan analysis of single-tracer simulations can be used as ‘gold



standard' for comparing the results from dual-tracer studies. Rows 3 and 4 show the statistics for DVR estimation using Logan analysis for the dual-tracer simulations using the extrapolation (EM) and simultaneous fitting (SM) methods. Though PCA-based smoothing was required for EM, it was not required for SM, since the smoothing was achieved by fitting the dual-tracer curves to the reference tissue models. There was high negative bias in DVR values estimated for Tracer *I* using EM, since 20 minutes of data was insufficient to accurately estimate DVR. This negative bias in Tracer *I* then propagated as a positive bias in Tracer *II* DVR estimates. In case of SM, direct parameter estimation and DVR calculation (without using Logan analysis) gave estimates that had lower bias than EM but prohibitively high variance (results not shown). However, estimation of six parameters from 80 min of noisy data would be expected to give noisy estimates. The variance in DVR estimates from SM was reduced by first separating the signals using the estimated parameters and then estimating DVR using standard Logan plot analysis. The results from this approach are shown in Table 5.3 (row 4). The SM approach gave DVR estimates with reduced bias but without an appreciable decrease in precision compared to EM.

The accuracy of the estimated DVR values depends strongly on the accuracy of the estimated target and reference region TACs ( $\hat{y}_i^I$  and  $\bar{y}_r^I$  for Tracer *I*;  $\hat{y}_i^{II}$  and  $\bar{y}_r^{II}$  for Tracer *II*). From the operational Logan plot equation, we know that systematic positive (negative) bias in a target region TACs would cause a positive (negative) bias in DVR. Similarly, systematic positive (negative) bias in the reference region TAC would cause a negative (positive) bias in DVR. Thus, in order to assess the cause of bias in DVR estimates seen in Table 5.3, the systematic error in the separated individual tracer curves must be analyzed.

The TACs separated from the noisy dual-tracer simulations were compared to the 'true' noise-free signals shown in Figure 5.2 as follows. The error at the  $j^{\text{th}}$  frame for the  $i^{\text{th}}$  realization of Tracer *I*, for example, was calculated as:  $error_j^I(T_i) = \bar{y}_i^{I,true}(T_j) - \hat{y}_i^I(T_j)$  ( $1 \leq j \leq p$ , where  $p = 26$  is the number of frames in the simulated PET study). These error values for each frame were normalized by the true

TAC value for that frame and averaged over the number of realizations ( $N = 1024$ ) to obtain mean percent error for each frame  $j$ :

$$mean \% error_j = \frac{1}{N} \sum_{i=1}^N \left( \frac{error_i(T_j)}{\bar{y}_i^{I,true}(T_j)} \times 100 \right). \quad - 5.11$$

The average of the mean percent errors for the last 8 eight frames ( $19 \leq j \leq 26$ ) was used as an index of systematic bias in the individual TACs for Tracers *I* and *II*.

The values of this statistic have been shown in the last two rows of Table 5.3. For noisy single-tracer TACs, this statistic was ~0% in all regions, since the noise in single-tracer TACs canceled out when averaged over the 1024 realizations (not shown in Table 5.3). The single-tracer TACs extracted from noisy dual-tracer TACs showed some systematic bias for most regions. A positive (negative) systematic bias in Tracer *I* TACs was seen to correspond to a negative (positive) bias in Tracer *II* TACs. This was expected since errors in Tracer *I* and Tracer *II* TACs need to be in opposite directions for the sum of the individual TACs to fit the dual-tracer curve. Overall, SM separated the signals more accurately than EM.

For all regions except Region 3, most of the contribution to the dual-tracer signal was from Tracer *II* (see Figure 5.2). Hence for these regions, a large mean percent error in Tracer *I* estimation translated into a comparatively small error in Tracer *II*. In Region 3, however, since both tracers have substantial contribution to the dual-tracer signal, mean percent error is of similar magnitude for Tracer *I* and Tracer *II* (-30% and 40% for EM; -8% and 11% for SM).

For EM, the negatively biased DVR values for Tracer *I* estimated from limited 20 min of data (Table 5.3, row 3, Tracer *I*) caused a large negative systematic bias in Tracer *I* TACs (Table 5.3, row 5, Tracer *I*). This negative bias in the Tracer *I* TACs ( $\hat{y}_i^I$ ) propagated as a positive systematic bias in Tracer *II* TACs ( $\hat{y}_i^{II} = \bar{y}_i - \hat{y}_i^I$ ) as seen in Table 5.3, row 5, Tracer *II*. This in turn caused positive bias in DVR estimation for Tracer *II* for most of the target regions (Table 5.3, row 3, Tracer *II*). In the simultaneous fitting approach, on the other hand, although the errors in TACs and biases in DVR estimates are still negatively correlated as seen by the opposite signs for the two tracers,

there is no causal relationship between them since parameters for both the tracers were estimated simultaneously.

For SM, since reference regions are recalculated after the simultaneous fitting step, there was no bias in their DVR estimates in spite of the systematic bias in their TACs (Table 5.3, row 4, reference regions underlined). The negative bias in DVR estimation for Tracer *II* using SM can be attributed primarily to the positive systematic bias in Tracer *II* reference region (Table 5.3, SM, Region 3; Mean % error = 11%).

### 5.3.2 Effects of failure of assumptions

For simulations where the Tracer *I* reference region did not reach equilibrium by 20 minutes, but rose or fell by 20% between the injection of Tracer *II* and the end of the study, we found that the results changed by less than 5% compared to those in Table 5.3. This indicates that noise-induced bias is more significant than bias caused by inability to bring the reference region to equilibrium early in the study. The precision of the DVR estimates remained unchanged and was found to be independent of the validity of the steady-state assumption.

Fixing  $k_4$  to incorrect values of up to  $\pm 20\%$ , however, caused a maximum difference of 10% in the estimated DVR values compared to those estimated by fixing the  $k_4$  parameters to their true values. Not fixing  $k_4$ , on the other hand caused prohibitively high variability in the curve fits for tracer separation as well as in the DVR estimates (results not shown). Thus, fixing the  $k_4$  values to the population average was a compromise between bias and precision in the DVR estimates. Again, the precision of the DVR estimates was found to be independent of the actual value that  $k_4$  was fixed to.

### 5.3.3 [ $^{11}\text{C}$ ]FMZ - [ $^{11}\text{C}$ ]PMP dual-tracer simulations:

The parameters of interest for the simulated [ $^{11}\text{C}$ ]FMZ-[ $^{11}\text{C}$ ]PMP dual-tracer TACs were DVR for Tracer *I* estimated using Logan analysis and  $k_3$  for Tracer *II* estimated using the reference-region based linear least squares (RLS). The top portion of Table 5.4 reports the statistics of the estimated parameters in terms of percent of true

value. DVR estimation for single-tracer simulations of Tracer *I* was performed using PCA-based Logan analysis, which yields unbiased binding estimates (row 1). For the single tracer simulations of Tracer *II*, RLS method caused a bias of greater than 20% for true  $k_3 > 0.1 \text{ min}^{-1}$  even for the single-tracer case (row 1). This is because for high  $k_3$  values, the two integral terms on the right hand side of equation 5.10 approach linear dependence ( $\bar{y}_i(\tau) \rightarrow \bar{y}_r(\tau)$ ). This makes the linear problem in equation 5.10 ill-conditioned leading to negative bias in  $k_3$  estimates. However, it must be noted that [ $^{11}\text{C}$ ]PMP target regions (e.g. cortex, thalamus) seldom have  $k_3$  values greater than  $0.1 \text{ min}^{-1}$  and hence the bias seen here is not a major impediment to the applicability of RLS method.

**Table 5.4:** Bias and standard deviation in parameter estimates and mean % error in separated TACs for [ $^{11}\text{C}$ ]FMZ-[ $^{11}\text{C}$ ]PMP dual-tracer simulations

	Tracer	Region 1		Region 2		Region 3		<u>Region 4</u>		Region 5		<u>Region 6</u>	
		<i>I</i>	<i>II</i>	<i>I</i>	<i>II</i>	<i>I</i>	<i>II</i>	<u><i>I</i></u>	<u><i>II</i></u>	<i>I</i>	<i>II</i>	<i>I</i>	<u><i>II</i></u>
	DVR	6.0	-	3.0	-	6.0	-	<u>1.0</u>	-	2.5	-	3.0	-
	$k_3$	-	0.03	-	0.06	-	0.1	-	0.15	-	0.25	-	2.00
Bias and SD in parameter estimates	Single-tracer	100 (6)	93 (16)	100 (6)	91 (17)	99 (6)	87 (18)	100 (9)	79 (21)	101 (9)	49 (21)	103 (13)	- (-)
	EM	71 (19)	126 (31)	82 (14)	94 (18)	69 (18)	104 (25)	98 (8)	76 (20)	84 (13)	47 (22)	89 (13)	- (-)
	SM	91 (19)	89 (35)	94 (14)	80 (23)	91 (20)	90 (35)	101 (8)	80 (32)	94 (14)	52 (31)	93 (15)	- (-)
Mean % error in TACs	EM	-25	17	-17	7	-30	17	-1	0	-15	3	-18	3
	SM	-6	7	8	-3	-3	2	6	1	10	0	12	-1

Bias and standard deviation in DVR estimates: a value of 100 denotes no bias. Region 4 (DVR=1.0) and region 6 ( $k_3=2.0$ ) are the reference regions for Tracer *I* and Tracer *II* respectively (underlined).

Mean % error in TACs: A positive (negative) value indicates a positive (negative) systematic bias in the last 8 frames of the TACs.

Row 2 reports the results for EM dual-tracer analysis. As seen in the [ $^{11}\text{C}$ ]FMZ-[ $^{11}\text{C}$ ]DTBZ case, EM gave negatively biased DVR estimates due to limited data available

for DVR estimation for Tracer *I*; especially for regions 1 and 3. This bias is reduced but not completely removed by SM (row 3) with a slight precision penalty. For Tracer *II*; estimation using EM shows lower bias and variability for  $k_3$  estimation than SM for regions 2 and 3; but this advantage is nullified by the bias in Tracer *I* DVR estimates.

The bottom two rows of Table 5.4 show the mean % error values, an index of the systematic bias in the estimated TACs  $\hat{y}_i'$  and  $\hat{y}_i''$  towards the end of the scan (last 8 frames) in all of the six simulated regions. These mean percent error values explain the trends in DVR and  $k_3$  estimates seen in the top portion of the same table.

## 5.4 Discussion and Conclusion

This chapter investigated two methods for non-invasive signal separation and parameter estimation in simulated dual-tracer dynamic PET scans where two tracers are injected with a delay of 20 min. Dual-tracer studies in human brain using arterial sampling approach have been performed in the past (Koeppel et al 2001). Recently there has been much interest in utilizing rapid dual-tracer PET for various applications such hypoxia and blood flow (Rust and Kadrmas 2006) and for tumor characterization (Black et al. 2008); all of which utilize arterial blood sampling. However, the discomfort of arterial sampling to the subject and the work load on PET technicians for metabolite correction of two tracers make the non-invasive reference-region based dual-tracer approach very desirable. The proposed methodology is based on the key assumption that Tracer *I* can be appropriately administered using a bolus followed by a constant infusion protocol to bring a region with no specific binding or trapping to steady state before the second tracer is injected. The ability to design such an administration protocol for human studies is discussed in the next chapter (dual-tracer human studies). For the tracers discussed in this work, only the reversible tracers ( $[^{11}\text{C}]\text{FMZ}$ ,  $[^{11}\text{C}]\text{DTBZ}$ ) satisfy this condition and have been evaluated as first tracers. The irreversible tracer ( $[^{11}\text{C}]\text{PMP}$ ), which does not satisfy this criterion, has been tested only as the second tracer. The second tracer, however, can be either reversible or irreversible and there is no constraint on its administration protocol. In this simulation work, we found that small errors due to inability to bring the reference region of Tracer *I* to steady state do not cause appreciable

bias in the estimated binding parameters, and furthermore do not adversely effect precision of these estimates.

The first approach explored for dual-tracer analysis was the extrapolation method (EM) where the knowledge of Tracer *I* prior to the injection of Tracer *II* was used to extrapolate the Tracer *I* signal until the end of the scan. This approach, though intuitive, introduced negative bias in Tracer *I* DVR estimates as 20 min of data before Tracer *II* injection was insufficient for accurate estimation of Tracer *I* DVR. A potential drawback of the two-step EM is that errors in parameter estimation of Tracer *I* from limited early data propagate into parameter estimates for Tracer *II*. As an alternative to EM, we also explored a one step parameter estimation approach to avoid the error propagation seen in EM. In this simultaneous fitting method (SM), where the parameters of both the tracers were estimated simultaneously by fitting the dual tracer TACs to the reference tissue models of both tracers, an improvement over EM in terms of bias in estimated parameters was achieved, but with a slight decrease in precision.

From the operational Logan plot equation it can be inferred that a systematic bias in the target region or reference region TACs would cause bias in the DVR estimates. Thus, mean percent error in the extracted TACs was calculated to assess the origin and effect of the parameter bias. It was seen that the SM extracted TACs from dual-tracer curves that were closer to the true TACs compared to the EM.

To improve the robustness of the fits using EM and SM, one of the parameters ( $k_4$ ) for both tracers was fixed to its population average. The simulations showed that incorrect assumption of this parameter caused some bias, but reduced variance in the estimated parameters. The precision of the parameters-of-interest was further improved by first extracting single-tracer TACs from dual-tracer TACs, and then estimating the parameters-of-interest by robust linear estimation techniques like Logan plots for reversible tracers (Logan et al. 1996) and reference-region based linear least squares method (RLS) for the irreversible tracer (Nagatsuka et al. 2001).

For noisy reversible single-tracer TACs, the bias seen in higher DVR estimates in reversible tracers using Logan plots was reduced using PCA-based Logan analysis (Joshi et al. 2008a). Though PCA-based smoothing was required for EM, it was not necessary for SM, since the required smoothing was achieved by fitting the dual-tracer curves to the

parallel reference tissue models. For irreversible tracers, we found that bias seen in the  $k_3$  estimation using RLS was due to the ill-conditioned nature of the operational RLS equation at high  $k_3$  values and not the dual-tracer method itself. Since high  $k_3$  regions are seldom regions-of-interest for irreversible tracers, this bias is not an impediment to the applicability of RLS.

It is important to note that non-invasive dual-tracer methodology is especially useful in ‘challenge’ studies where the simultaneous effect of a physiological challenge on two different neuropharmacological systems is of interest. Using a standard single-tracer approach, four scans would be required to perform such an experiment (two ‘baseline’ scans and ‘two’ challenge’ scans), which would practically be very difficult. The dual-tracer approach could achieve this goal by requiring just two scans (one ‘baseline’ and one ‘challenge’).

In conclusion, this chapter it was demonstrated that single tracer information can be extracted from non-invasive dual-tracer PET studies, and that such studies bear promise in situations where a single neurochemical marker is insufficient to characterize a neurological condition. In the next chapter the methods developed here will be applied to human dual-tracer data and validity of the methods will be tested.

## Chapter 6

### Dual-tracer studies: Human Studies

This chapter reports the first results from non-invasive dual-tracer PET in humans where two radiotracers were injected closely in time within the same scan and data is acquired *without* arterial sampling. These studies yield near simultaneous information on two different neuropharmacological systems, providing better characterization of a subject's neurological condition. Two approaches for separating the contributions of the two tracers, an extrapolation method and a simultaneous fitting method, have been validated in simulation studies (Chapter 5) and were applied to the human dual-tracer studies reported in this chapter. Combinations of two reversible tracers ( $[^{11}\text{C}]$ flumazenil and  $[^{11}\text{C}]$ dihydrotetrabenazine) or one reversible and one irreversible tracer ( $[^{11}\text{C}]$ N-methylpiperidinyl propionate) were used. Physiological indices estimated from the studies were the blood brain barrier transport parameter ( $R_f$ ), the distribution volume ratio (DVR) for the reversible tracers and the trapping constant ( $k_3$ ) for the irreversible tracer. Following each dual-tracer scan, a 'gold standard' single-tracer scan was obtained using one of the two tracers for comparison of the dual-tracer results. Both approaches provided parameter estimates with inter-subject regions-of-interest means typically within 10% of those obtained from single-tracer scans and without any appreciable increase in variance.

In this work we investigated a non-invasive (reference tissue-based) approach for analysis of dual-tracer human studies, which, in addition to being convenient for the subjects since it avoids arterial sampling and multiple scans, is also advantageous as it eliminates the need for plasma metabolite analysis for the two tracers. Dual-tracer methodology brings promise to 'challenge' studies, where the effect of a pharmacological or behavioral challenge on two different systems is of interest. Such studies normally



would require four single-tracer scans (two ‘baseline’ and two ‘challenge’ scans), but would require only two dual-tracer scans (one ‘baseline’ and one ‘challenge’).

The key assumption in non-invasive dual-tracer PET as mentioned in Chapter 5 is that the first radiotracer injected must have a region with negligible density of binding or trapping sites that by appropriate tracer administration, can be made to achieve (and then maintain) steady-state concentration levels prior to injection of the second radiotracer. With this assumption, the radioactivity in the reference tissue is known from the time of injection of the second tracer through to the end of scan. Two methods for non-invasive dual-tracer analysis based on this assumption are detailed in the Chapter 5. They are: i) an extrapolation method (EM) where first tracer’s time-activity curves (TACs) were extrapolated over scan duration followed by subtraction from dual-tracer TACs and ii) a simultaneous fitting method (SM) where reference tissue models for both tracers are fitted simultaneously to the dual-tracer TACs.

Direct voxel-wise parameter estimation in a dual-tracer study suffers from poor precision due to noise in the PET TACs (Joshi et al. 2008b). In this work, we have attempted to minimize the variance in the parametric images by implementing the following three steps: a) noise reduction in TACs by an adaptive smoothing approach, b) reduction in the number of parameters to be fitted by fixing the  $k_4$  parameter for both tracers to their population average in the full reference tissue model for reversible tracers (RTM), and c) application of robust linear estimation techniques to single-tracer curves extracted from dual-tracer data. Each of these steps is described in detail in Section 6.4.

## 6.1 Radiotracers

The radiotracers used in this study have been well characterized for traditional single-tracer PET scans at our institution: flumazenil ( $[^{11}\text{C}]\text{FMZ}$ ), a benzodiazepine receptor antagonist (Holthoff et al. 1991; Koeppe et al. 1991); dihydrotetrabenazine ( $[^{11}\text{C}]\text{DTBZ}$ ), a ligand for the VMAT2 binding site (Koeppe et al. 1999a; Koeppe et al. 1997; Koeppe et al. 1996); and N-methylpiperidiny propionate ( $[^{11}\text{C}]\text{PMP}$ ), a substrate for hydrolysis by the enzyme acetylcholinesterase (AChE) (Koeppe et al. 1999b). Both  $[^{11}\text{C}]\text{FMZ}$  and  $[^{11}\text{C}]\text{DTBZ}$  can be classified as reversible tracers and have been analyzed

successfully using both bolus and bolus+continuous infusion protocols. [ $^{11}\text{C}$ ]PMP can be classified as an irreversible tracer because the hydrolyzed product cannot be converted back to authentic PMP and cannot cross the blood–brain barrier (BBB).

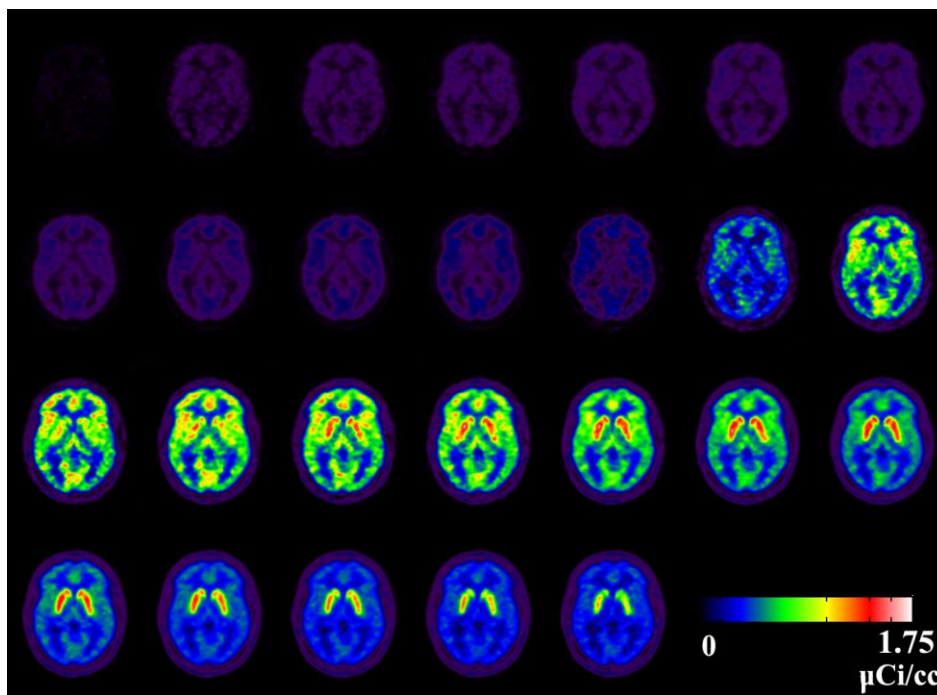


**Figure 6.1:** Dynamic dual-tracer PET image sequence for [ $^{11}\text{C}$ ]FMZ - [ $^{11}\text{C}$ ]DTBZ study with a 20 minute offset. The frame sequence for the 80 min scan was four  $\times$  0.5 min, three  $\times$  1.0 min, two  $\times$  2.5 min, two  $\times$  5.0 min, (second tracer injected at 20 min), four  $\times$  0.5 min, three  $\times$  1.0 min, two  $\times$  2.5 min, two  $\times$  5 min, and four  $\times$  10 min frames. The second tracer is injected just before the 12<sup>th</sup> frame. Note that the much large apparent signal of [ $^{11}\text{C}$ ]DTBZ is in part due to displaying decay corrected data. Hence, the injection of the same dose of [ $^{11}\text{C}$ ]DTBZ at 20 min appeared twice as high relative to the [ $^{11}\text{C}$ ]FMZ in the early frames.

Figure 6.1 shows the dynamic image sequence from a [ $^{11}\text{C}$ ]FMZ-[ $^{11}\text{C}$ ]DTBZ study where [ $^{11}\text{C}$ ]DTBZ was injected as a bolus 20 minutes after [ $^{11}\text{C}$ ]FMZ. The second tracer is injected at the start of the 12<sup>th</sup> frame. The [ $^{11}\text{C}$ ]DTBZ signal is the dominant of the two tracers seen by higher magnitude of the frames after [ $^{11}\text{C}$ ]DTBZ injection, but one should note that part of this higher magnitude is due to the decay-correction which makes the counts for DTBZ appear approximately twice as high due to the half-life of  $^{11}\text{C}$ . Figure 6.2 shows dual tracer curves for four regions from the study shown in Figure 6.1.

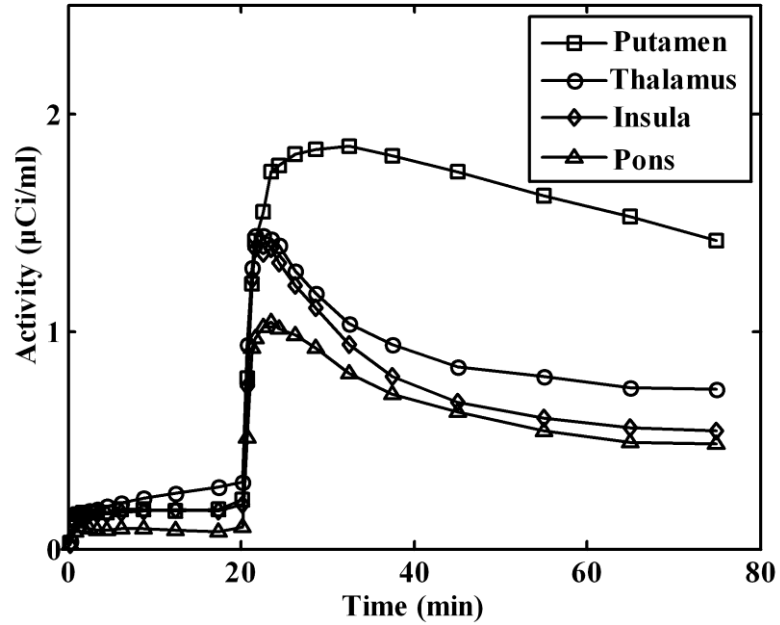


Figure 6.2: Average dual-tracer curves for four regions from the study in Figure 6.1.

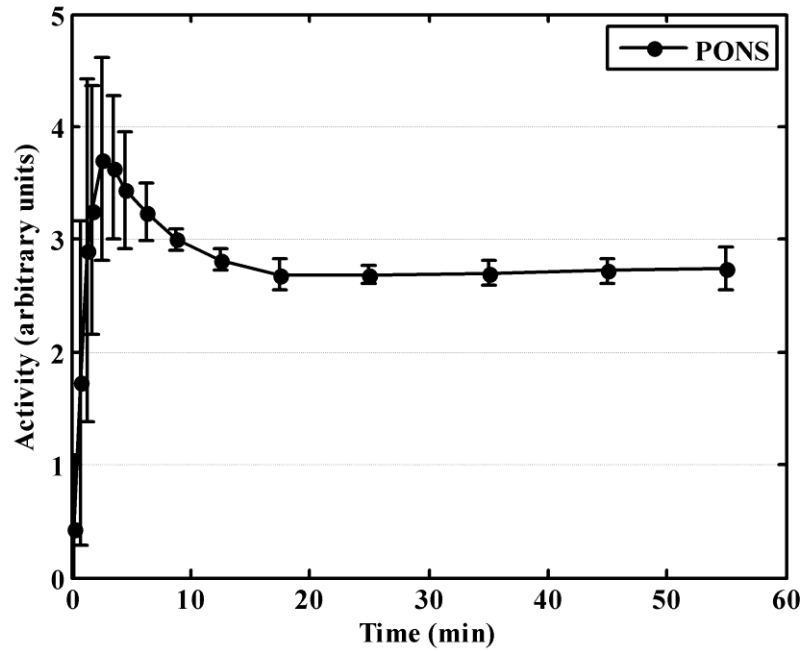


Figure 6.3: Average time-activity curve (TAC) for pons, the reference tissue for  $[^{11}\text{C}]\text{FMZ}$ , from seven subjects that underwent a 60 min single-tracer  $[^{11}\text{C}]\text{FMZ}$  scan. TACs have been scaled such that the area under the curve is the same for all subjects to account for differences in absolute radioactivity levels. Error bars give the standard deviation of the TACs for the seven subjects and indicate the degree of variability in maintaining steady-state conditions.

## 6.2 Validation of the key assumption:

The key assumption of achieving steady-state in the first tracer's reference tissue prior to injection of the second tracer needs to hold for the implementation of both EM and SM approaches. Of the tracers used in this study, only [ $^{11}\text{C}$ ]FMZ and [ $^{11}\text{C}$ ]DTBZ have regions with negligible specific binding; pons and occipital cortex, respectively. The irreversible tracer [ $^{11}\text{C}$ ]PMP, however, has no region of negligible trapping; thus, only [ $^{11}\text{C}$ ]FMZ and [ $^{11}\text{C}$ ]DTBZ were used as the first tracers in this work, while [ $^{11}\text{C}$ ]PMP was used exclusively as a second tracer.

Figure 6.3 shows the average TAC for pons, (the reference region for [ $^{11}\text{C}$ ]FMZ) from seven subjects that underwent a 60 min single-tracer [ $^{11}\text{C}$ ]FMZ scan. The pons TAC for each individual subject has been normalized such that the area under the curve is the same for all subjects. These scans showed that it was possible to achieve steady-state in the pons by 20 min into the study and maintain the radiotracer concentration at this level after the second tracer has been administered throughout the remainder of the study. The infusion protocol (35% bolus-65% infusion) was designed such that steady state was achieved by 20 min while at the same time reasonable counts were obtained from early frames. Giving even less as a bolus would allow steady-state conditions to be reached even sooner; however, this decreases the statistical quality of the early data. The error bars indicate standard deviations of the tissue curve values across subjects. A slightly larger standard deviation was seen towards the end of the 60 min scan, indicating that some subject's reference tissue TAC may have deviated from steady-state, either increasing or decreasing slightly over time. However, computer simulations (Joshi et al. 2008b) have showed that the small deviations from steady-state as seen in Figure 6.3 are not expected to cause appreciable errors in the estimated parameters.

## 6.3 Data acquisition, reconstruction, and processing:

Dual-tracer studies were performed on 37 healthy subjects using the following two tracer pairs: (1) [ $^{11}\text{C}$ ]FMZ and [ $^{11}\text{C}$ ]DTBZ, or (2) [ $^{11}\text{C}$ ]FMZ and [ $^{11}\text{C}$ ]PMP. Table 6.1 summarizes the details of the studies such as order in which the tracers were injected,

the time difference between tracer injections, the tracer administration protocol, and the single-tracer scan that followed the dual-tracer scan.

For [ $^{11}\text{C}$ ]FMZ and [ $^{11}\text{C}$ ]DTBZ tracer combinations, since both tracers have regions with negligible specific binding sites, studies were performed using either as the first tracer. For studies in which [ $^{11}\text{C}$ ]FMZ was injected first, studies were performed with two delay windows between tracer injections (20 and 30 min) to assess the improvement in results with an increase in separation between the tracers. It was not possible to reliably achieve steady-state in the occipital cortex, the reference tissue for [ $^{11}\text{C}$ ]DTBZ, by 20 minutes. Hence studies where [ $^{11}\text{C}$ ]DTBZ was injected first were performed with a 30 min injection offset.

**Table 6.1:** Imaging protocol details for dual-tracer studies.

Dual-tracer Scans <sup>a</sup>	Time Difference between tracer injections	Injection protocol <sup>b</sup>	Single-tracer scan following the dual-tracer scan	Number of subjects
[ $^{11}\text{C}$ ]FMZ/[ $^{11}\text{C}$ ]DTBZ	20	Infusion/Bolus	FMZ	2
		Infusion/Infusion	DTBZ	2
	30	Infusion/Bolus	FMZ	1
		Infusion/Infusion	DTBZ	1
[ $^{11}\text{C}$ ]DTBZ/[ $^{11}\text{C}$ ]FMZ	30	Infusion/Bolus	FMZ	2
		Infusion/Infusion	DTBZ	2
	30	Infusion/Bolus	FMZ	1
		Infusion/Infusion	DTBZ	1
[ $^{11}\text{C}$ ]FMZ/[ $^{11}\text{C}$ ]PMP	20	Infusion/Bolus	FMZ	5
			PMP	5
	30	Infusion/Bolus	FMZ	4
			PMP	5

<sup>a</sup> injection order

<sup>b</sup> administration protocol for first tracer and second tracer respectively

The injected radioactivities were approximately the same for both tracers, with twelve mCi (444 MBq)  $\pm 10\%$  of each tracer administered. Scan data was acquired for 80 min as a dynamic sequence of 26 or 27 frames for 20 or 30 min offsets, respectively. The framing protocol consisted of shorter duration frames when there was a rapid change in the tissue radioactivity concentration (after each tracer injection) and longer duration frames when there was gradual or little change in the activity. The protocol with 20 min delay between tracer injections was four  $\times$  0.5 min, three  $\times$  1.0 min, two  $\times$  2.5 min, two  $\times$  5.0 min, (second tracer injected at 20 min), four  $\times$  0.5 min, three  $\times$  1.0 min, two  $\times$  2.5 min, two  $\times$  5 min, and four  $\times$  10 min frames (26 frames in all). The protocol with 30 minute delay was four  $\times$  0.5 min, three  $\times$  1.0 min, two  $\times$  2.5 min, four  $\times$  5.0 min, (second tracer injected at 30 min), four  $\times$  0.5 min, three  $\times$  1.0 min, two  $\times$  2.5 min, two  $\times$  5 min, and three  $\times$  10 min frames (27 frames in all). The dual-tracer studies were followed by a 60 min single-tracer scan using one of the tracers used in the dual-tracer study, with framing the same as the final 60 min of the 20 min delay protocol. Each single-tracer scan provided a 'gold standard' for comparison with one of the tracers from the dual-tracer scan. Single tracer studies were not performed for both the dual-scan tracers due to time and radiation dosimetry constraints. The single-tracer scans were also used to assess the validity of the key assumption that the first tracer's reference tissue reaches steady-state before the second tracer is administered (see Figure 6.3).

All PET scans were performed in 3-D acquisition mode on an ECAT EXACT HR+ tomograph (Siemens Medical Systems, Inc., Knoxville, TN, USA). Measured attenuation correction with segmentation and re-projection were performed from 5-minute duration 2-D transmission scans. Images were reconstructed using Fourier rebinning (FORE) (Defrise M et al. 1997) of the 3-D data into 2-D sinograms and ordered subsets expectation maximization (OSEM) (Hudson and Larkin 1994; Comtat et al. 1998) using 4 iterations and 16 subsets. No post-reconstruction smoothing was applied resulting in reconstructed images of approximately 5.0-5.5 mm full-width and half-maximum (FWHM) both in-plane and axially. Subject motion across frames was corrected using Neurostat, initially developed at the University of Michigan (Minoshima et al. 1994; Minoshima et al. 1993). All scans were oriented, including non-linear warping, to the stereotactic Talairach atlas (Talairach and Tournoux 1988) using

Neurostat routines. All modeling estimations were performed voxel-by-voxel, creating parametric images of the BBB transport parameter ( $R_1$ ), the distribution volume ratio ( $DVR = 1 + BP_{ND}$ ; (Innis et al. 2007)) for the reversible tracers, and a ‘trapping rate’ parameter ( $k_3$ ) for the irreversible tracer. Volumes-of-interest (VOIs) were obtained using a standardized VOI template defined in Talairach atlas space.

## 6.4 Robust parameter estimation

To improve the robustness of the parameter estimates of interest, following three steps were implemented.

### 6.4.1 Adaptive smoothing

In this step, a spatially dependent smoothing protocol was implemented to reduce noise in TACs prior to the signal separation and parameter estimation steps. The neighborhood of the voxel’s TAC under consideration ( $y_i$ ) was searched to identify those TACs that had shapes similar to that of  $y_i$ . An average of the TAC under consideration and the qualifying neighboring TACs yielded a TAC with reduced noise. This approach resulted in little smoothing in regions with kinetically distinct voxels, thus preserving spatial resolution. The procedure is mathematically represented below:

A set of voxel indices  $N_i$  was selected for the voxel  $i$  under consideration such that:

$$N_i = \{j : \|y_i - y_j\|_2 < T\}, \quad - 6.1$$

where  $y_j$  is the TAC of a neighboring voxel  $j$ ,  $\|y_i - y_j\|_2$  is the  $L_2$ -norm of the difference vector between  $y_i$  and  $y_j$ , and  $T$  is the threshold for the  $L_2$ -norm and was chosen to be 10% of  $\|y_i\|_2$ . This search was performed in a 3 x 3 x 3 neighborhood (~0.3 ml) of voxel  $i$ .

Once the set of TACs was determined, an average TAC was calculated ( $y_i^{AVG}$ ) which has less noise than the original dual-tracer TAC ( $y_i$ ) and was used for curve separation and parameter estimation.

### 6.4.2 Population average $k_4$ in the full reference tissue model

Another step used to improve precision in the separation of the individual tracer components and hence the estimated neuropharmacological parameters was reducing the complexity of the full reference tissue model by fixing the  $k_4$  parameter for each tracer to its respective population average value. The rationale for this step is as follows. Our overall goal was the estimation of DVR ( $=1+BP_{ND}$ ) for each tracer. Since  $BP_{ND}$  is equal to the ratio of  $k_3/k_4$ , it may seem that using the simplified reference tissue model (sRTM; Section 2.4.2)(Lammertsma and Hume 1996) where only  $BP_{ND}$  is estimated instead of  $k_3$  and  $k_4$  separately, would accomplish the same goal. However, the simplifying assumption in sRTM is instantaneous equilibration between free and specific compartments, which implies very high values for both  $k_3$  and  $k_4$ . This assumption may bias the shapes of the individual tissue curves for the tracers used in this work. By fixing the  $k_4$  values to their respective population averages, we reduce the complexity of the full reference tissue model, as in sRTM, but constrain the individual tracer TACs to more closely approximate their true shapes. This simplification reduces parameter variance though with the possible introduction of some bias. However, the magnitude of this bias would be less compared to that if sRTM was used.

### 6.4.3 Signal separation followed by estimation of binding measures

In case of SM, the pharmacological parameters of interest, such as DVR, could be calculated directly from the individual model parameters of the  $k_4$ -constrained full reference tissue model. However, direct calculations of DVR from the individual estimated rate constants still lacked precision despite the adaptive smoothing and  $k_4$  constraint. Instead, the reference tissue model fits to the dual-tracer curves were used only to extract the voxel-wise TAC components for each of the two radiotracers (as elaborated in section 5.1.2). Each tracers' voxel-wise TACs and their corresponding reference tissue curves were then used with robust linear estimation methods to obtain final parametric images (Logan graphical analysis for DVR estimation in reversible



tracers (Logan et al. 1996) and reference-region based linear least squares (RLS) for  $k_3$  estimation in irreversible tracers (Nagatsuka et al. 2001)).

For single-tracer studies of reversible tracers, the parameters of interest were estimated using PCA-based Logan plot analysis (Joshi et al. 2008a). For the irreversible tracer, the parameter-of-interest ( $k_3$ ) was estimated using the RLS method. The adaptive smoothing approach described earlier was applied to single tracer data as well, prior to voxel-wise parametric estimation.

## 6.5 Results

Figure 6.4 shows the parametric images estimated using EM from a [ $^{11}\text{C}$ ]FMZ-[ $^{11}\text{C}$ ]DTBZ dual-tracer study obtained with the same protocol as shown in Figure 6.1. The parametric images for both FMZ (top two rows) and DTBZ (bottom two rows) are shown for the relative blood brain barrier (BBB) transport rate,  $R_l$  ( $= \frac{K_1}{K_1^{ref}}$ ; rows 1 and 3) and the distribution volume ratio, DVR ( $=1+BP_{ND}$ ; rows 2 and 4). Image quality for all measured parameters is good.

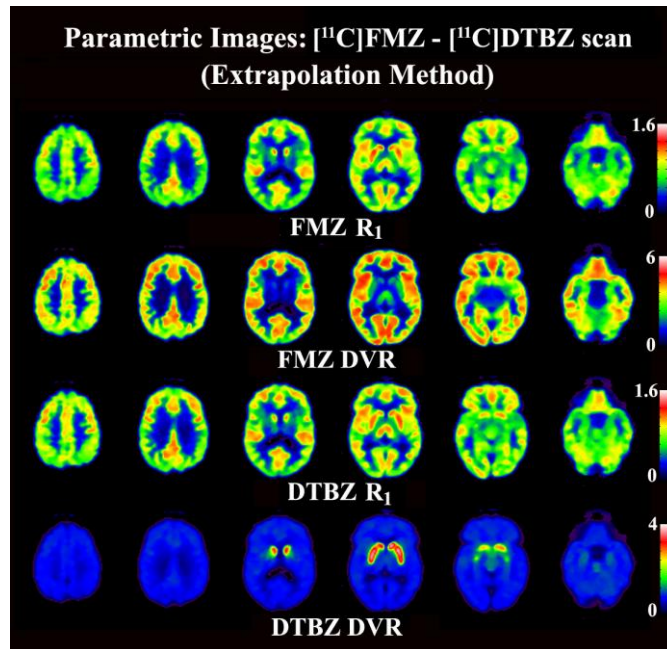


**Figure 6.4:** Parametric images obtained from a [ $^{11}\text{C}$ ]FMZ - [ $^{11}\text{C}$ ]DTBZ study at six brain levels. The parametric images shown are  $R_l$ , equal to the ratio  $K_1 / K_1^{ref}$  (rows 1 and 3), and the distribution volume ratio (DVR= $1+BP_{ND}$ ) (rows 2 and 4) for both tracers.

### 6.5.1 [ $^{11}\text{C}$ ]FMZ - [ $^{11}\text{C}$ ]DTBZ studies

Figure 6.5 (panel A) shows distribution volume ratio (DVR) images of three brain slices for studies with the same 20 min FMZ:DTBZ protocol as in Figure 6.1. The left-most column for each tracer shows the DVR images obtained from a single-tracer scan (ST). The middle and the right-most columns for each tracer show DVR images obtained from the dual-tracer studies using the extrapolation method (EM) and simultaneous fitting method (SM), respectively. Since single-tracer scans were performed using only one of the two tracers used in the dual tracer study, the images seen in the left and right halves of Figure 6.5 (all panels) are from different subjects. The dual-tracer scans analyzed using EM and SM yielded images very close in quality to those obtained from single-tracer scans. Overall image quality of SM was slightly noisier than EM image as SM required the simultaneous estimation of six parameters from an 80 min dual-tracer study. The image quality tended to improve when the two tracers were separated by 30 min instead of 20 min; since increasing tracer separation improves signal separation as was reported for dual-tracer studies using arterial plasma inputs (Koeppel et al. 2001).

The bar graphs in Figure 6.6 (panel A) show the comparison of the means and standard deviations of eight regions-of-interest extracted from both single-tracer and dual-tracer parametric images. On average, the EM method showed a positive bias in DVR for [ $^{11}\text{C}$ ]FMZ as compared to ST which can be primarily attributed to the fact that 20 min of data was insufficient to accurately estimate first tracer's transport and binding parameters. The positive bias was seen in the SM method as well, but to a lesser extent. As would be expected, the slight positive bias in the DVR estimates of FMZ propagate as a slight negative bias in DTBZ estimates. The magnitude of the DTBZ bias is less pronounced because for this tracer combination, the [ $^{11}\text{C}$ ]DTBZ signal is the dominant contributor to the dual-tracer data (see Figures 6.1 and 6.2). The inter-subject variance of the dual-tracers methods for different brain regions was only slightly higher on average than those seen in the single-tracer images, indicating that the image quality did not suffer due to excessive noise propagation in the dual-tracer approach.

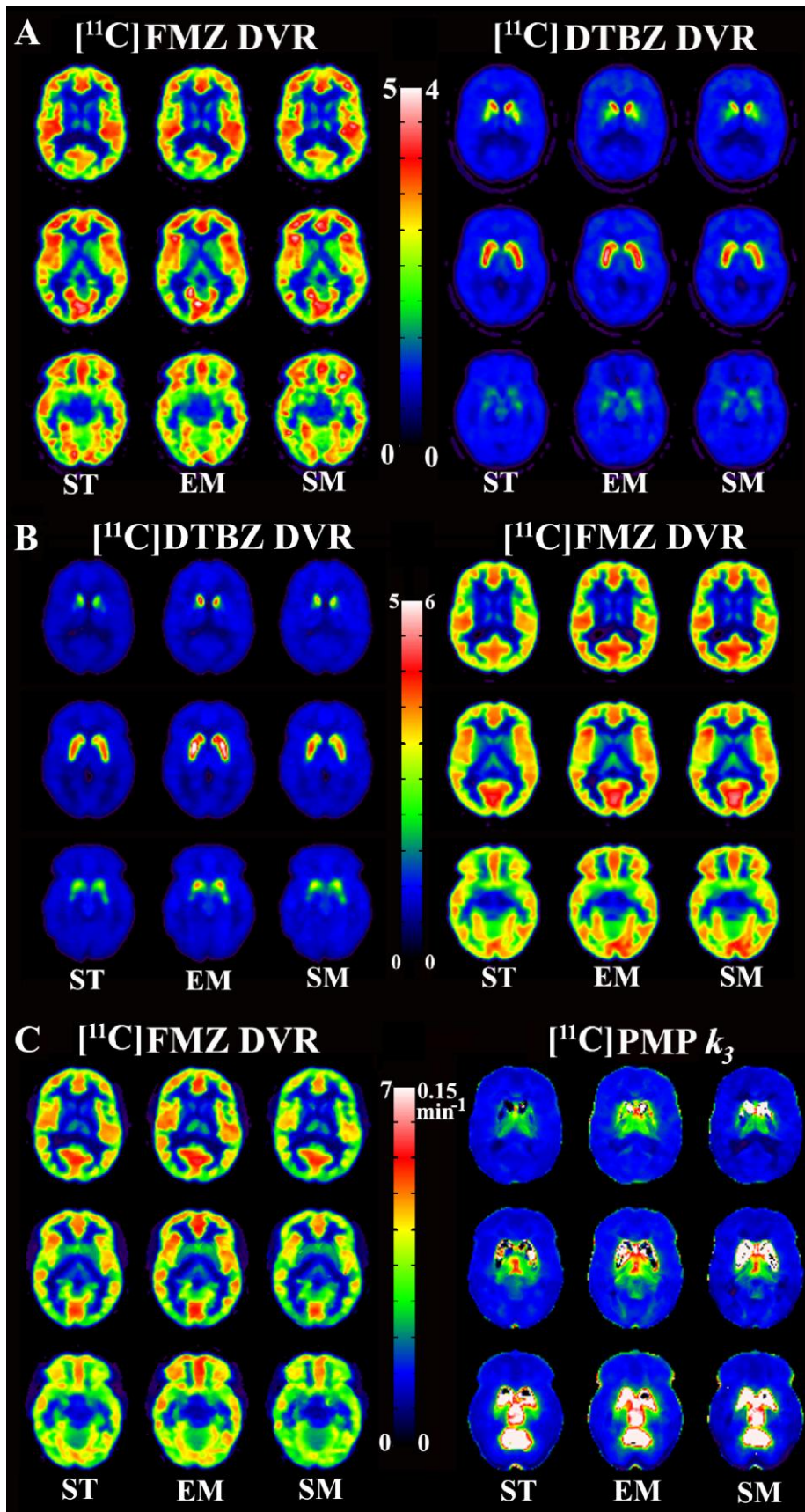


**Figure 6.5:** Comparison of parametric images of three brain levels from dual-tracer with those from single-tracer studies. The left-most column for each tracer is from a single-tracer study (ST) which acts as ‘gold standard’ for comparison of dual tracer results.

Panel A:  $[^{11}\text{C}]\text{FMZ}$  injected 20 min prior to  $[^{11}\text{C}]\text{DTBZ}$ .

Panel B:  $[^{11}\text{C}]\text{DTBZ}$  injected 30 min prior to  $[^{11}\text{C}]\text{FMZ}$ .

Panel C:  $[^{11}\text{C}]\text{FMZ}$  injected 30 min prior to  $[^{11}\text{C}]\text{PMP}$ .

The extrapolation method (EM) and simultaneous fitting method (SM) show image patterns and magnitudes very close to those from the single tracer (ST) studies.

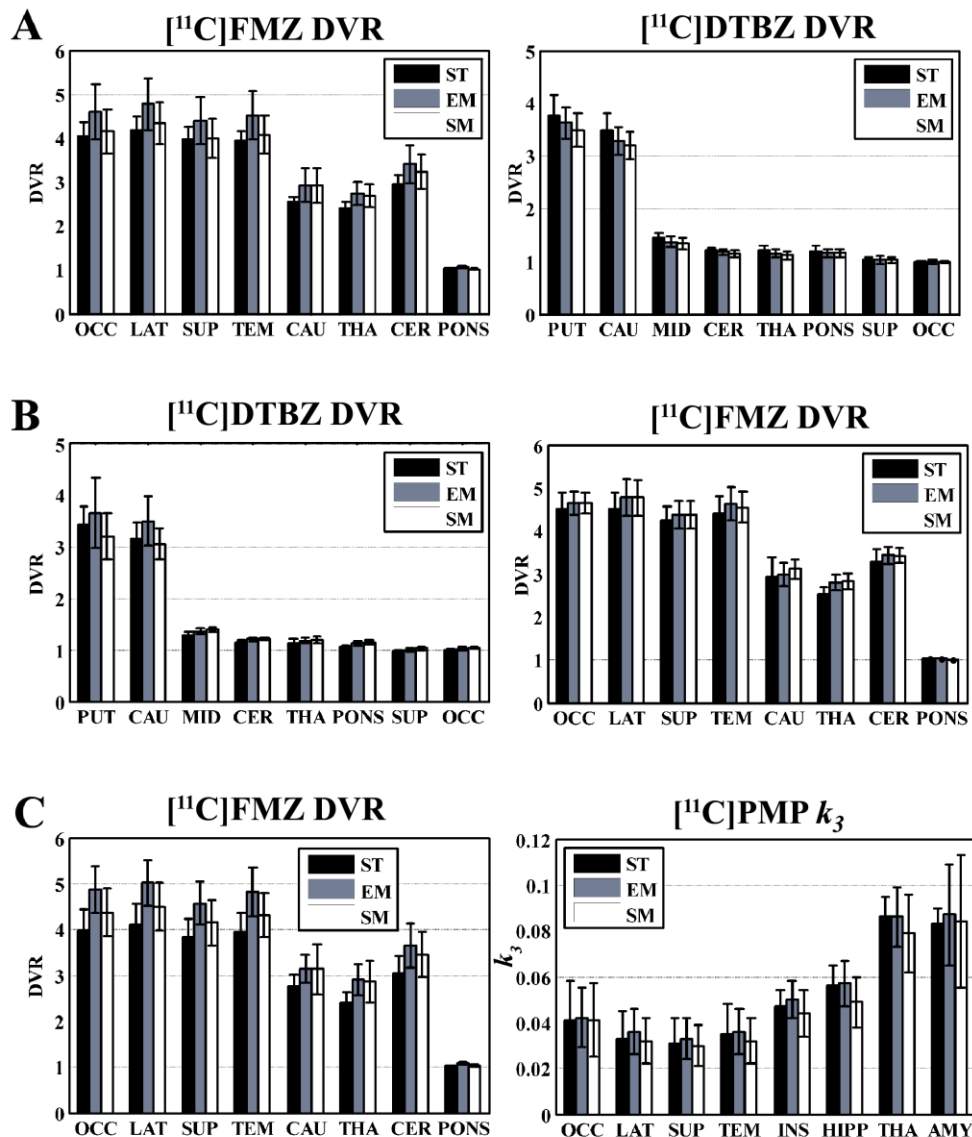


**Figure 6.6:** Comparison of inter-subject means and standard deviations in parametric estimates obtained from single-tracer (ST) and dual-tracer studies analyzed using extrapolation method (EM) and simultaneous fitting method (SM). Results from eight regions-of-interest extracted from parametric images are shown. Panel A: Comparison of dual-tracer [<sup>11</sup>C]FMZ-[<sup>11</sup>C]DTBZ studies (n=12) with single tracer studies (n=6). Panel B: Comparison of dual-tracer [<sup>11</sup>C]DTBZ-[<sup>11</sup>C]FMZ studies (n=6) with single tracer studies (n=3). Panel C: Comparison of dual-tracer [<sup>11</sup>C]FMZ-[<sup>11</sup>C]PMP studies (n=19) with single tracer studies (n=10 for [<sup>11</sup>C]FMZ and n=9 for [<sup>11</sup>C]PMP). The regions-of-interest for FMZ are: OCC: occipital cortex, LAT: lateral frontal cortex, SUP: superior parietal cortex, TEM: lateral temporal cortex, CAU: caudate nucleus, THA: thalamus, CER: cerebellar hemisphere, PONS: pons. The regions-of-interest for DTBZ are: PUT: putamen, CAU: caudate nucleus, MID: midbrain, CER: cerebral hemisphere, THA: thalamus, PONS: pons, SUP: superior parietal cortex, OCC: occipital cortex. The regions-of-interest for PMP are: OCC: occipital cortex, LAT: lateral frontal cortex, SUP: superior parietal cortex, TEM: lateral temporal cortex, INS: insular cortex, HIPP: hippocampus, THA: thalamus, AMY: amygdala.

### 6.5.2 [ $^{11}\text{C}$ ]DTBZ - [ $^{11}\text{C}$ ]FMZ studies

Figure 6.5 (panel B) shows the dual-tracer parametric images from [ $^{11}\text{C}$ ]DTBZ-[ $^{11}\text{C}$ ]FMZ studies where [ $^{11}\text{C}$ ]DTBZ was injected first followed by [ $^{11}\text{C}$ ]FMZ with a 30 minute time difference. As in panel A, the left-most column for each tracer shows the DVR images obtained from a single-tracer scan. The middle and the right-most columns show DVR images obtained from the dual-tracer studies using the extrapolation method (EM) and simultaneous fitting method (SM), respectively. Again, the dual-tracer methods were successful in accurately separating the individual-tracer signals as indicated by the similarity of ST and either the EM and SM parametric images. Similar to the [ $^{11}\text{C}$ ]FMZ-[ $^{11}\text{C}$ ]DTBZ case, the images for EM method have higher values than those in the single-tracer scan, while the same scan analyzed with the SM method yielded results closer to those of the single-tracer scan.

Figure 6.6 (panel B) shows regions-of-interest comparison of the inter-subject means and standard deviations extracted from single-tracer and dual-tracer parametric images. Trends similar to those seen in panel A are seen for this dual-tracer protocol, including the positive bias in EM DVR values for the first tracer, which in this protocol was [ $^{11}\text{C}$ ]DTBZ. As before, the inter-subject region-of-interest variance for dual-tracers methods in most regions was similar or only slightly higher on average than those seen in the single-tracer images, again indicating that image quality in dual-tracer PET is not degraded substantially by propagation of noise.

### 6.5.3 [ $^{11}\text{C}$ ]FMZ - [ $^{11}\text{C}$ ]PMP studies

Figure 6.5 (panel C) shows the parametric images (DVR for [ $^{11}\text{C}$ ]FMZ and  $k_3$ , the trapping constant, for [ $^{11}\text{C}$ ]PMP) for a study protocol where [ $^{11}\text{C}$ ]FMZ was injected 30 minutes prior to [ $^{11}\text{C}$ ]PMP. As in panels A and B of Figure 6.5, the left-most column for each tracer shows the parametric DVR or  $k_3$  images obtained from a single-tracer scan. The middle and the right-most columns show parametric images obtained from the dual-tracer studies using the extrapolation method (EM) and simultaneous fitting method (SM), respectively. The estimation of the trapping constant for [ $^{11}\text{C}$ ]PMP using the

reference-region based linear least squares method (RLS) (Nagatsuka et al. 2001) breaks down for very high values of the trapping parameter due to the assumption of the method that the basal ganglia represents complete trapping, and analysis cannot be done in this region due to the ill-conditioned nature of the operational equation (see Chapter 5). This can be seen in both the single-tracer and dual-tracer  $k_3$  images. AChE activity has a very large dynamic range in the human brain, and since the primary regions of interest for PMP are in the cortex, the images are scaled to better show these values rather than cerebellum (vermis) and brainstem structures which appear as white in the parametric images.

Figure 6.6 (panel C) summarizes the means and standard deviations from the parametric images for eight chosen regions. The bar graphs for [ $^{11}\text{C}$ ]FMZ show familiar features as seen in panels A and B (Figure 6.6); positively biased DVR estimates for EM and a much less pronounced bias for SM-based DVR estimates. The EM-based bias is less for the trapping constant estimation. Estimation of  $k_3$  from signals extracted using SM, on the other hand, is negatively biased for most regions compared to the single-tracer ‘gold standard’ values. The inter-subject region-of-interest variance for EM and SM was similar to that seen in ST images for [ $^{11}\text{C}$ ]FMZ, but higher for [ $^{11}\text{C}$ ]PMP. For [ $^{11}\text{C}$ ]PMP, the variance in the dual-tracer methods was larger than that in single tracer studies for regions such as thalamus and amygdala that have higher AChE activity.

## 6.6 Discussion and Conclusion

This chapter presented the first results of human dual-tracer brain PET studies performed non-invasively using reference tissue approaches, hence not requiring arterial blood sampling and plasma metabolite analyses. The reference tissue based non-invasive dual-tracer methodology used in this work can provide information on two distinct biological systems from a single PET scan without the inconvenience of arterial sampling for both the subject and the investigators. For example, since the various neurotransmitter systems of the brain do not act in isolation but have complex interactions, dual-tracer methods can be particularly useful in ‘challenge’ studies where a pharmacological or behavioral intervention may affect more than a single neuropharmacological system.

The key assumption for this attractive methodology is that for the first radiotracer injected there exists a brain region with negligible specific binding or trapping, and which by an appropriate bolus + continuous infusion protocol can be brought to equilibrium prior to the injection of the second radiotracer. This assumption allows one to know the full time course of the reference tissue curve that acts as an “input function” for the reference tissue model. In general, both reversible as well as irreversible tracers that satisfy the above criterion could be injected first. In this study however, the irreversible tracer [ $^{11}\text{C}$ ]PMP could not be used first since it has no region that is void of AChE. Rapidly equilibrating tracers, such as flumazenil used here or raclopride, would be expected to work well, while more slowly equilibrating tracers such as methylphenidate, carfentanil and many others, would be poor choices for the “first” tracer.

Of the two analysis approaches evaluated, the extrapolation method, though intuitive, was seen to introduce bias in many studies, as parameter estimates derived from only 20-30 min of data can be insufficient for robust parameter estimation. Furthermore, biases in the parameter estimates of the first tracer will propagate as biases in the parameter estimates of the second tracer. The biases in the two tracers, in general, will be negatively correlated, as an error in first tracer’s TAC estimation would be compensated by an opposite error in the second tracer’s TAC, in order for the sum of the individual tracer curves to fit the dual-tracer curve. Thus, to avoid the limitations of the EM approach, a simultaneous fitting method was developed and evaluated. In the majority of cases, an improvement of the simultaneous method over EM was seen in terms of better correspondence of the DVR measures with those of the single-tracer scans. This was achieved by fitting the dual-tracer TACs with a combined reference tissue model, to optimally separate the total PET signal into its two ‘single-tracer’ components. A possible remaining source of bias in the SM approach is that prior to the simultaneous fit, the reference tissue TAC for the second tracer must be determined for which the extrapolation approach was still needed. Once the second reference tissue curve is obtained, the TACs for all voxels can be separated. One aspect of our implementation of the simultaneous method is that after separation of the dual-tracer scan into its two individual tracer image sequences, one can redefine the reference-tissue curves on the separated data sets. This may help in removing some bias as, for example, the slight

variations from true steady-state in the first tracer's reference tissue may be accounted for after curve separation.

One of the primary concerns in any dual-tracer approach is the need to estimate roughly twice as many parameters as compared to a single-tracer PET study. While at first glance, this may seem to be a prohibitive problem, the fact that administration of the two tracers is offset in time provides considerably more 'kinetic' information in a dual-tracer curve than a single tracer curve. However, trying to estimate 6-8 parameters from an 80 min PET session is more challenging than estimating 2-3 parameters from a single-tracer scan, and precision of the parameter estimates is a concern. Thus, we made efforts along three fronts to enhance precision in order to provide more robust results.

First, we reduced the voxel-level noise in the TACs by a simple adaptive smoothing procedure. The choice of the threshold for this step must be made carefully, as too high a threshold would result in little smoothing, hence little improvement in precision, while too low a threshold would result in overly degrading the effective spatial resolution of the parametric images. The success of this approach can be seen in the parametric images shown in Figures 6.4 and 6.5. In all cases, the apparent noise level is nearly as low for dual-tracer studies as for single-tracer scans. In some studies, particularly those involving PMP there was some noticeable increase in noise in the  $k_3$  images.

Second, we fixed the  $k_4$  parameter of the full reference tissue model for both tracers to their respective population average values during the fitting procedure for separating the dual-tracer signal into its individual components. Using the full reference tissue model (4 parameters, for each tracer), yet fitting only 3 parameters per tracer, helped to stabilize the fit while maintaining a model formulation with more realistic shapes for the tracers' time-activity curves. As mentioned earlier, this is because we do not assume that the exchange between free and specific compartments is instantaneous, which could bias the shapes of the tissue TACs.

Third, while reducing the number of fitted parameters improved the ability to extract the single-tracer curves; using the direct parameter estimates to calculate DVR ( $=1 + k_3/k_4$ ) with good precision is still limited. This is similar to single-tracer studies, where more stable estimates of DVR can usually be obtained by methods such as Logan



plots, rather than directly using nonlinear least squares estimates of individual rate parameters for calculation of DVR. Hence in this study, application of the robust linear Logan graphical analysis was used after separation of individual tracer signals to obtain estimates of the parameters of interest, DVR (RLS for  $k_3$ ) and  $R_1$ . Since the separated tissue time-activity curves were obtained as smooth curves, the potential biases in Logan-based DVR estimates due to noisy data are avoided.

There was a mismatch between the bias seen in the EM method in human scans (where positive bias was seen in the DVR estimates) compared to that predicted by the simulation studies in the previous chapter (where negative bias was seen in the DVR estimates). One possible explanation for this is that a reference region tissue model may not be able to accurately simulate all the complexities of an actual human PET scan. Additionally, the noise in the simulations was higher than the levels observed in the human studies after the adaptive smoothing.

As expected, increasing the offset in tracer injection time from 20 to 30 minutes provided an improvement in precision for both EM and SM approaches. However, this is a trade-off that would have to be considered for any dual-tracer application. Minimizing the time difference between the administrations of the two tracers would provide more simultaneous estimation of the tracer parameters, but would decrease the precision of parameter estimates. On the other hand, increasing the time difference between tracer injections, while improving precision in parameter estimates, would increase the chance that the biological or pharmacological state of the subject would change. This may be problematic especially in ‘challenge’ studies where one assumes a variety of biological parameters (blood flow, endogenous neurotransmitter levels, receptor occupancy) are constant over time.

In conclusion, non-invasive dual-tracer methodology has been shown to produce results comparable to single-tracer scans, and promises to be a very useful technique for nearly simultaneous evaluation of multiple brain systems from a single PET acquisition.

## **Chapter 7**

### **Reducing inter-scanner PET image variability**

This thesis so far has concentrated on the estimation of pharmacological properties of neuroreceptor systems. We have seen that the accuracy of the estimated parameters depends upon kinetic modeling steps such as selection of a physiologically relevant yet practical model, handling of the noise in the TACs and appropriate weighting of data. These kinetic modeling steps assume that the reconstructed dynamic PET data provides quantitatively accurate radiotracer concentrations in the image voxels. In other words, inaccuracy of the radiotracer concentration values in the PET image would lead to inaccurate TACs, thus causing inaccuracies in the parameter estimates.

A primary source of signal loss in PET is attenuation of the signal through absorption of the emitted photons by the tissue. Accurate quantification of radioactivity concentration has challenges in addition to the photon absorption. These include count-rate losses due to dead-time of system components, variations in efficiency of detectors and acceptance of unwanted scattered and random coincidences. The ability to accurately correct for these sources of errors, while minimizing the impact on signal-to-noise ratio, largely determines the accuracy of PET images. The handling of these corrections is an ongoing research problem and PET and PET/CT scanner manufacturers implement these corrections differently. These software differences along with hardware differences (crystal types, axial field-of-view, energy windows etc) lead to differences in the images of the same object obtained from scanners manufactured by different vendors. This variability, even if small, can be problematic in multi-center trials. The motivation for the work in this chapter is to minimize the PET scanner model related systematic variability before the multi-center data is pooled together for analysis.

The work in this chapter is part of the ongoing multi-center Alzheimer's Disease Neuroimaging Initiative (ADNI) project, a longitudinal multi-site observational study of

healthy controls, patients with mild cognitive impairment (MCI), and mild Alzheimer's disease (AD) patients. This five year research project aims to study the rate of change of cognition, brain structure and function in 200 elderly controls, 400 subjects with mild cognitive impairment, and 200 with Alzheimer's disease. Data is being acquired from these subjects at multiple time points using magnetic resonance imaging (MRI), [<sup>18</sup>F]FDG PET, urine serum, and cerebrospinal fluid (CSF) biomarkers, as well as clinical/psychometric assessments. PET scans were performed on half of the subjects in each group. The Division of Nuclear Medicine PET Center at the University of Michigan is the coordinating center for all PET data.

The objective of this work is reduction of inter-scanner differences in static FDG scans (single frame scans with no temporal information) obtained from ~50 participating PET centers having fifteen different scanner models. In spite of a standardized imaging protocol, systematic inter-scanner variability in PET images from various sites has been observed due to differences in scanner resolution, reconstruction techniques, and different implementations of scatter and attenuation corrections on the different scanner types. Before the data across centers can be analyzed, it is important to minimize these differences.

The differences in the human scans obtained from the different scanner types were classified into two broad categories: actual anatomic and functional inter-subject variability and systematic scanner related variability. An attempt to reduce the systematic differences between different scanner-types is the focus of this work.

The correction factors to reduce inter-scanner systematic variability were obtained from Hoffman brain phantom (Hoffman et al. 1990) scans acquired at the participating sites. Hoffman brain phantom is a cylindrically shaped phantom that simulates the radiotracer distribution in a normal human brain. The correction factors were obtained by comparison of the phantom scans with a 'gold standard' digital Hoffman brain phantom (i.e. true radioactivity distribution).

The systematic differences in the images from different sites can be classified into two broad categories: high frequency resolution differences and low frequency uniformity differences. Resolution differences are primarily due to differences in crystal sizes, and also to a lesser extent due to detector material (LSO, BGO, GSO and LYSO),

detector crystal axial depths, energy windows, as well as the number of rings, crystals per ring and axial FOV. The low frequency uniformity differences may manifest as differences in contrast (grey-to-white matter ratios), superior-to-inferior and midline-to-lateral gradients. These non-uniformities between scanners are likely to be caused primarily by disparity in the handling of attenuation and scatter. The high frequency correction proposed in this work involves smoothing the data from different scanner types to a common resolution. The low frequency correction involves application of smooth affine correction factors following the high frequency correction. Smoothing kernels for high frequency correction and affine correction factors for low frequency correction were obtained from comparison of phantom scan data with the digital phantom. The correction factors were applied to phantom scans to see the maximum recovery possible using these methods. Subsequently, the corrections were applied to 95 normal subject scans to test their utility in humans.

## **7.1 Multi-center Hoffman brain phantom scan protocol**

### **Phantom Scans**

Hoffman brain phantom scans were obtained from all participating sites using the following protocol:

1. The Hoffman phantom is filled with 0.5-0.6 mCi of  $^{18}\text{F}$  solution and placed in the scanner.
2. The chest phantom is filled with 2.0-2.4 mCi of  $^{18}\text{F}$  solution and placed close to the Hoffman phantom to simulate the effects of out-of-field activity.
3. The 3-D Hoffman phantom is imaged for 30 minutes to obtain high quality images with low statistical noise contribution.
4. The image volume is registered to the digital Hoffman brain phantom to achieve a common orientation and image grid for all scans.

## Pre-processing of phantom scans

Two phantom scans per site were obtained for test/retest purposes. There were fifteen different scanner models used in the ~50 participating sites. All scans passing quality control tests were registered to the digital Hoffman phantom. The voxel-grid for all scanner-types was 160 x 160 x 90 with voxel-size of 1.548 mm. The size of 1.548 was chosen such that the dimensions of the digital phantom matched the physical dimensions of the Hoffman brain phantom. The registered images from each site were normalized using a mask (based on the digital Hoffman phantom) such that the mean of all voxels lying within the mask was unity. The normalized phantom images from different sites having the same scanner-type were averaged to obtain an average image per scanner model. Let this normalized average image for scanner model  $n$  be represented as  $A_n$  ( $A_n \in R^{p \times q \times r}$  where  $p = 160$  (x-dimension),  $q = 160$  (y-dimension) and  $r = 90$  (z-dimension)). High and low frequency correction factors were obtained by comparison of the average image  $A_n$  with the digital Hoffman brain phantom as described below.

## 7.2 Theory of high and low frequency corrections

### 7.2.1 High frequency correction

The high frequency correction is a smoothing operation to bring the images from the different scanner types to as uniform a resolution as possible. The common minimum resolution was determined by estimating the resolution of each scanner type from phantom scans. The digital Hoffman brain phantom was smoothed in all three dimensions with incremental full width half maximum (FWHM) Gaussian kernels to obtain a library of the digital phantom at various resolutions as shown below.

$$\mathbf{D} \otimes k_i = \mathbf{D}_i, i = 1 \text{ mm}, 2 \text{ mm}, \dots, 10 \text{ mm}, \quad - 7.1$$

where  $\mathbf{D}$  is the unsmoothed digital Hoffman brain phantom,  $k_i$  is the smoothing kernel with FWHM of  $i$  mm in all three dimensions,  $\otimes$  is the convolution operator and  $\mathbf{D}_i$  is the

smoothed phantom with  $i$  mm resolution. During implementation of this step, different in-plane (xy plane) and axial (z-axis) smoothing was done; but for brevity it has been represented here to be the same in all dimensions (Equation 7.1). The effective resolution of  $n^{\text{th}}$  scanner model was estimated by determining the smoothed digital phantom ( $D_i$ ) that was closest to  $A_n$  in the least squares sense as shown below.

$$\hat{i}_n = \arg \min_i \left\| \bar{A}_n - \bar{D}_i \right\|_2, \quad - 7.2$$

where  $\bar{A}_n$  and  $\bar{D}_i$  are lexicographically arranged vectors of all the voxels in the three-dimensional image volumes  $A_n$  and  $D_i$  respectively. The coarsest resolution among all the scanner models was found to be between 7 and 8 mm both in plane and axially. The ‘target’ resolution for the average phantom image ( $A_n$ ) for each scanner model was chosen to be 8 mm.

Kernels to smooth each scanner model’s average phantom image to the target resolution were determined as follows. A library for each average phantom scan  $A_n$  was formed by smoothing it with incremental FWHM Gaussian kernels with as shown below.

$$A_{n,j} = A_n \otimes k_j, j = 1\text{mm}, \dots, 10\text{mm} \quad - 7.3$$

Smoothing kernel for each scanner type was selected such that the smoothed image ( $A_{n,j}$ ) matched the ‘gold standard’ digital phantom smoothed to 8mm resolution ( $D_8$ ) in the least squares sense as shown below.

$$\hat{j}_n = \arg \min_j \left\| \bar{D}_8 - \bar{A}_{n,j} \right\|_2, \quad - 7.4$$

where  $\bar{A}_{n,j}$  and  $\bar{D}_8$  are lexicographically arranged vectors of the three dimensional image volumes  $A_{n,j}$  and  $D_8$  respectively. As before,  $j$  was allowed to vary between in-plane and axial smoothing. Let the phantom image for scanner type ‘ $n$ ’ after smoothing to 8mm resolution be represented by  $A_{n,\hat{j}_n}$ . The smoothing kernel for each scanner type ( $k_{\hat{j}_n}$ ) is applied to every the human subject scan ( $I_n$ ) obtained from scanner model  $n$  ( $I_{n,\hat{j}_n} = I_n \otimes k_{\hat{j}_n}$ ).

## 7.2.2 Low frequency correction

High frequency correction is followed by low frequency adjustment to correct for differences across scanner models that are presumed to be primarily due to small but consistent errors in the attenuation and scatter corrections. The following linear model was used for low frequency correction.

$$\mathbf{D}_g = \mathbf{a}_n \mathbf{A}_{n, \hat{j}_n} + \mathbf{b}_n + \boldsymbol{\varepsilon}_n, \quad - 7.5$$

where  $\mathbf{a}_n$  and  $\mathbf{b}_n$  are the low frequency correction terms (multiplicative and additive respectively) to be determined from the high frequency corrected phantom images  $\mathbf{A}_{n, \hat{j}_n}$  ( $\boldsymbol{\varepsilon}$  is the residual term). Note that all terms in Equation 7.5 have the same dimensions and all operations are voxel-wise. The terms  $\mathbf{a}_n$  and  $\mathbf{b}_n$  are smooth functions for  $n^{\text{th}}$  scanner type and are designed as linear combinations of fifth order polynomials as shown below:

$$a_{n,p} = \sum_{m=1}^M \alpha_m \lambda_{p,m}, \quad b_{n,p} = \sum_{m=1}^M \beta_m \lambda_{p,m}, \quad - 7.6$$

where  $a_{n,p}$  and  $b_{n,p}$  are values of the correction factors  $\mathbf{a}_n$  and  $\mathbf{b}_n$  at voxel  $p$ ,  $M$  is the total number of polynomial terms ( $M = 52$  for three dimensional fifth order polynomials),  $\alpha_m$  and  $\beta_m$  are the coefficients of the polynomial term  $m$ , and  $\lambda_{p,m}$  is the value of the  $m^{\text{th}}$  polynomial term at voxel  $p$ . Since the low frequency errors were expected to be symmetric across the midbrain, the non-symmetric polynomial terms (28 in number) were eliminated ( $M = 34$ ). The correction terms  $\mathbf{a}_n$  and  $\mathbf{b}_n$  can be expressed in the vector form as follows:

$$\bar{\mathbf{a}}_n = \Lambda \bar{\boldsymbol{\alpha}}_n, \quad \bar{\mathbf{b}}_n = \Lambda \bar{\boldsymbol{\beta}}_n, \quad - 7.7$$

where  $\bar{\mathbf{a}}_n \in \mathcal{R}^{N \times 1}$  and  $\bar{\mathbf{b}}_n \in \mathcal{R}^{N \times 1}$  vectors are the lexicographical arrangements of the three-dimensional terms  $\mathbf{a}_n$  and  $\mathbf{b}_n$  ( $N$  is the number of voxels in the image volume),

$\Lambda \in R^{N \times M}$  is the polynomial matrix and  $\bar{\alpha}_n, \bar{\beta}_n \in R^{M \times 1}$  are the coefficients of the polynomial terms. We estimated the coefficient set  $(\bar{\alpha}_n, \bar{\beta}_n)$  for the  $n^{th}$  scanner model by the following minimization:

$$(\hat{\bar{\alpha}}_n, \hat{\bar{\beta}}_n) = \arg \min_{(\bar{\alpha}_n, \bar{\beta}_n)} \left\| \bar{D}_8 - \text{diag}(\bar{A}_{n, \hat{j}_n}) \Lambda \bar{\alpha}_n - \Lambda \bar{\beta}_n \right\|_2^2 \quad - 7.8$$

The low frequency correction factors can then be applied to the individual PET images that have undergone high frequency correction ( $I_{n, \hat{j}_n}$ ). The application of low frequency correction for scanner type  $n$  would be:

$$C_{n, \hat{j}_n} = a_n I_{n, \hat{j}_n} + b_n. \quad - 7.9$$

### 7.3 High frequency correction factors from phantom scans

**Table 7.1 :** Scanner models and the FWHM (in mm) of the smoothing kernels to attain a resolution of 8 mm FWHM (in-plane and axial).

Scanner Model	PET or PET/CT	FWHM in-plane (mm)	FWHM axially (mm)
Siemens HRRT	PET	6	6
Siemens Biograph HiRez	PET/CT	6	5
Phillips Gemini TF	PET/CT		
Siemens HR+	PET	5	5
GE Discovery RX	PET/CT	5	4
Phillips G-PET	PET		
GE Advance	PET	5	3
GE Discovery LS	PET/CT		
GE Discovery ST	PET/CT	4	3
Phillips Gemini	PET/CT	3	3
Phillips Gemini GXL	PET/CT		
Phillips Allegro	PET		
Siemens Accel	PET	2	3
Siemens Exact	PET		
Siemens Biograph	PET/CT		



The high frequency correction factors (FWHM or the smoothing kernels) to smooth the images from various scanners to 8 mm resolution are listed in the Table 7.1.

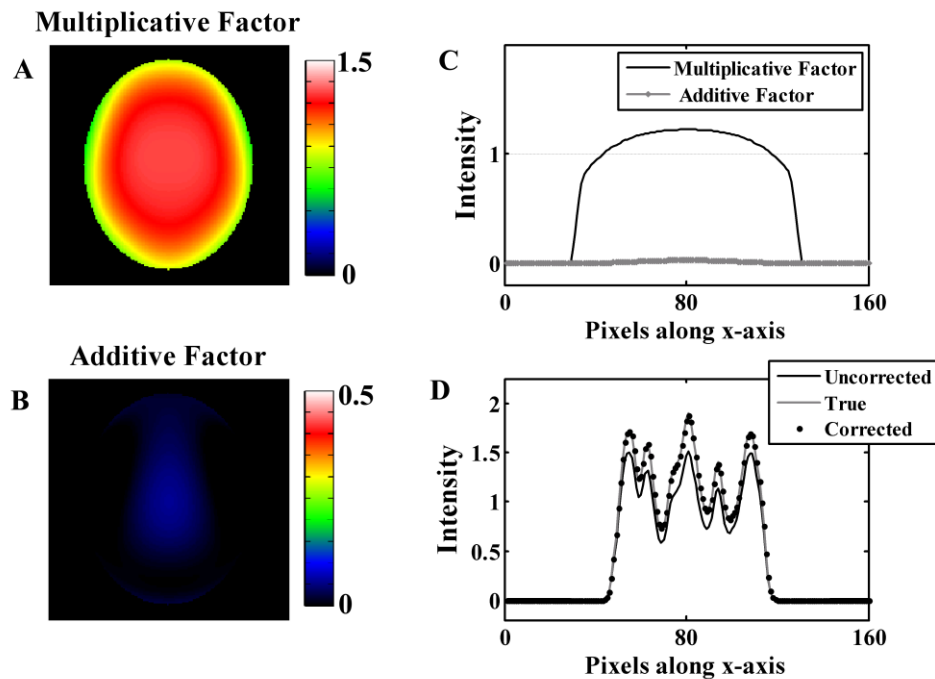
#### **7.4 Assessment of the validity of low frequency correction factors using simulations:**

Simulations were performed to validate the low frequency correction methodology proposed above as well as to get an intuitive feeling for their physical interpretation. The following three scenarios of residual low frequency errors were simulated using a digital Hoffman phantom smoothed to 8mm resolution ( $D_8$ ):

1. Simulation of residual attenuation: The smoothed digital Hoffman brain phantom,  $D_8$ , was forward-projected to obtain its emission sinogram ( $E$ ) and transmission sinogram based on ellipse attenuation ( $T$ ) using ASPIRE software (Fessler 1995). To simulate errors in attenuation correction, the residual attenuation sinogram was chosen to be the transmission scan  $T$  scaled by 0.1. The emission sinogram with residual attenuation was calculated as  $E_A = Ee^{-0.1T}$  (element-wise operations). No noise was added to the sinogram.  $E_A$  was reconstructed using filtered back projection (FBP) to obtain the phantom image with residual attenuation. The proposed low frequency correction methods were applied to test whether they could correct for the attenuation correction error.
2. Simulating residual scatter: The smoothed digital Hoffman brain phantom,  $D_8$ , was forward-projected to obtain its emission sinogram ( $E$ ). The scatter sinogram was approximated by smoothing  $E$  with a Gaussian filter (45 mm width and 15 mm standard deviation). The smoothed sinogram was scaled by 0.15 to approximate a residual scatter sinogram ( $S$ ). The sinogram with residual scatter was obtained ( $E_S = E + S$ ) and reconstructed using FBP to obtain the phantom image with residual scatter. The proposed low frequency correction methods were applied to test whether they could correct for the scatter correction error.

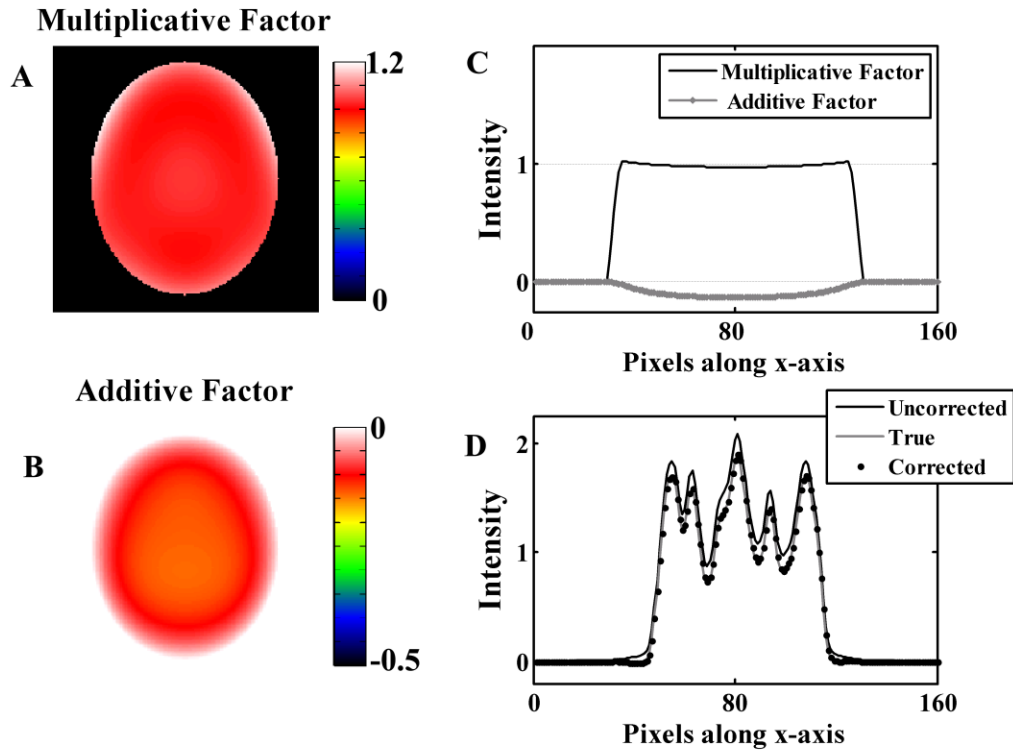
3. Simulation of residual attenuation and scatter: Both scatter and attenuation were simulated in the forward projected digital Hoffman brain phantom as mentioned above and a sinogram with both residual attenuation and scatter was obtained ( $E_{A+S} = E_A + S$ ). The resultant sinogram ( $E_{A+S}$ ) was reconstructed using FBP and the proposed low frequency correction method was used to test its ability to remove the combined residual error.

Figure 7.1 shows image slices of the additive and multiplicative factors obtained from the simulation study where the reconstructed image contains residual attenuation alone. The correction-factors are symmetric due to the symmetry constraint applied to the polynomial basis functions as attenuation errors are primarily multiplicative. The additive factor was very close to zero and the multiplicative factor is the major contributor to the correction. Panel C shows the profiles of the correction factors in the x-axis (medical lateral) for fixed y (anterior posterior) and z (inferior superior) locations. The application of the correction factors removed the attenuation error as seen by the phantom image profiles in Panel D.



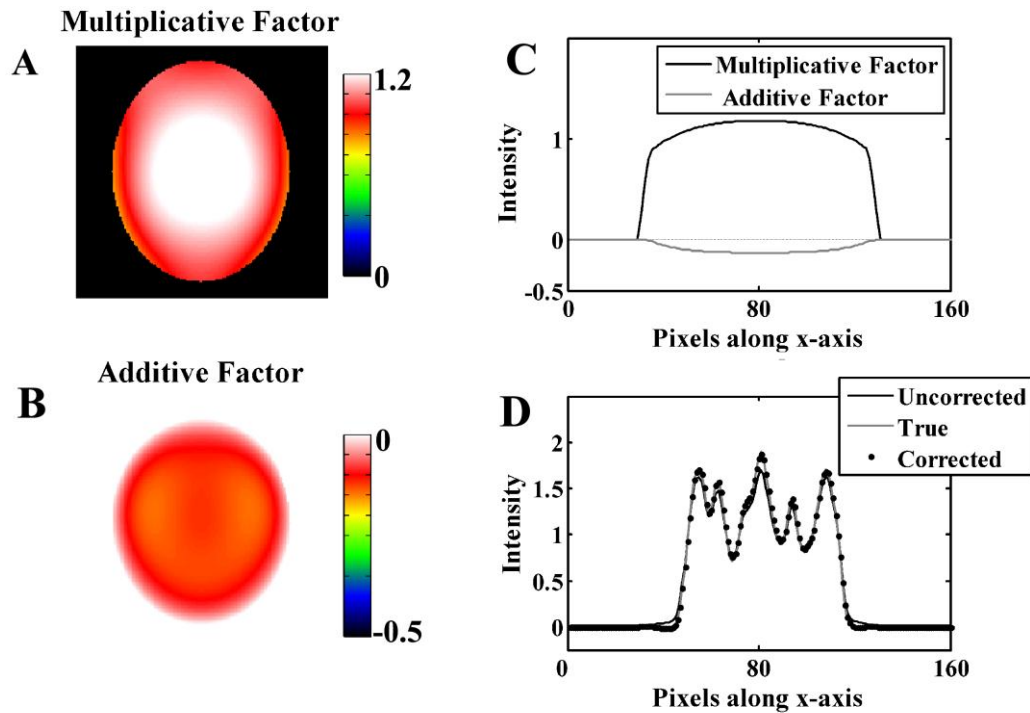
**Figure 7.1:** Low frequency correction factors for simulations with residual attenuation error alone. Panels A and B show the multiplicative and additive correction factors. Panel C shows a sample profile through the 3-D correction factors. Panel D shows the profiles of true (digital phantom), pre-corrected and post corrected phantom image data.

Figure 7.2 shows image slices of additive and multiplicative factors obtained from the simulation study where the reconstructed image contained residual scatter alone. Scatter being primarily though not entirely an additive error, the multiplicative factor was small while the additive factor was the major contributor to the correction. Panel C shows the profiles through the correction factor images. The application of the correction factors removes the scatter error as seen by the image profiles in Panel D.



**Figure 7.2:** Low frequency correction factors for simulations with residual scatter error alone. Panels A and B show the multiplicative and additive correction factors. Panel C shows a sample profile of the correction factors. Panel D shows the profiles of true (digital phantom), pre-corrected and post corrected data.

For the simulation case with both residual scatter and attenuation, both additive and multiplicative factors made significant contributions to the correction (Figure 7.3). Thus, the simulations show that the additive factor primarily encodes the scatter correction while the multiplicative factor primarily encodes the attenuation correction.



**Figure 7.3:** Low frequency correction factors for simulations with both residual scatter and attenuation errors. Panels A and B show the multiplicative and additive correction factors. Panel C shows a sample profile of the correction factors. Panel D shows the profiles of true (digital phantom), pre-corrected and post corrected data.

## 7.5 Application of correction factors to phantom and human image data

### 7.5.1 Phantom scans

As mentioned earlier, human studies have both inter-subject as well as inter-scanner differences. Since the same phantom was imaged at all participating sites, the phantom studies did not have any “inter-subject” type variation. Thus, the differences in phantom scans are primarily due to scanner differences. Since the correction factors were obtained from phantom scans themselves, application of correction factors to these same phantom scans will give a measure of the maximum reduction in variability possible from the methods described in this chapter. Differences in phantom scans were calculated for three groups: phantom scans with no correction, phantom scans after only high frequency correction and phantom scans after both high and subsequent low frequency correction.

The measure of the difference between a phantom image from scanner  $i$  and those from the other scanner types was obtained using the following metric:

$$\%RMSE_i = \frac{1}{N} \sum_{\substack{j=1 \\ j \neq i}}^N \frac{\|\bar{Y}_i - \bar{Y}_j\|_2}{\|\bar{Y}_i\|_2} \quad - 7.10$$

$\bar{Y}_i$  is the vector of lexicographically arranged voxel values of an image from scanner  $i$  and  $N = 15$  is the total number of scanner types. This metric for each scanner type is expected to decrease after the high frequency correction and then further after low frequency correction. The improvement in phantom images by the application of the correction factors can be seen in Figure 3. The 100% line is the variability in the first group (images with no correction). The high frequency correction reduces the variability by 20% – 50% (higher reduction for high resolution scanners). The low frequency correction further reduced the variability by 10% -15%. In spite of these two steps, 40% - 60% residual variability is seen in the phantom scans. This can be attributed to three primary reasons: first, the affine low frequency correction term is a first order correction step and is not a complete model for low frequency variability. Second, a single smoothing kernel for high frequency correction was used for the entire image, which may not be optimal throughout the entire imaging volume. The remaining variability can be attributed to the differences in phantom orientation in scanner, misregistration error, non-uniform mixing of  $^{18}\text{F}$  solution in the phantom and other technical errors.

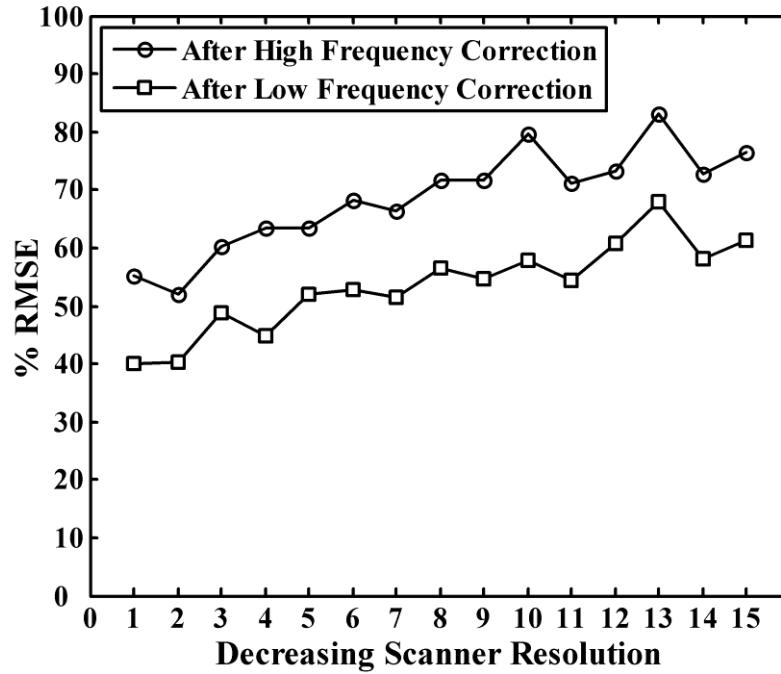


Figure 7.4: Application of the correction factors derived from phantom data to phantom data itself.

### 7.5.2 Human scans (Control subjects)

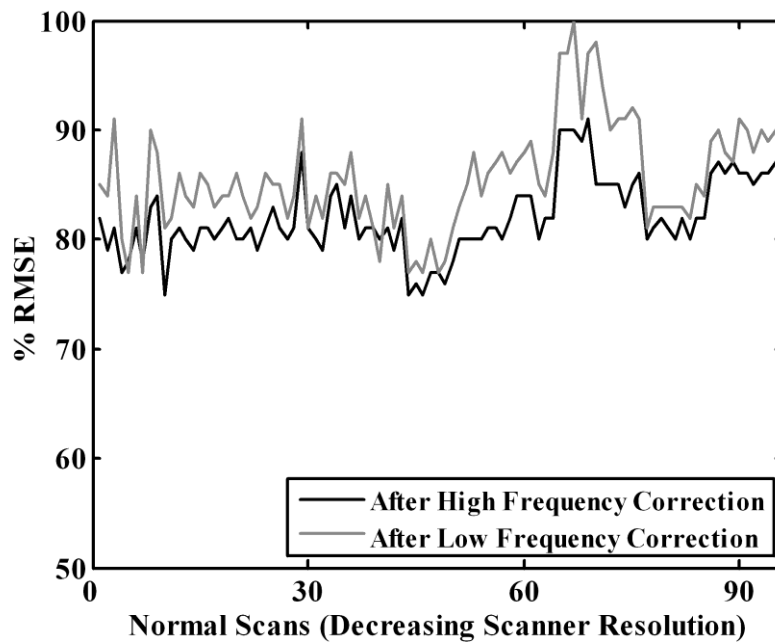


Figure 7.5 Application of the correction factors derived from the phantom data to human normal scans.

For validation of the methods in human studies, the correction factors obtained from phantom scans were applied to a set of 95 normal subject scans obtained from various participating sites. The inter-scanner variability was calculated in the same way as in Figure 7.4 for three groups: normal subject scans without any correction, after high frequency correction alone and after both high and low frequency corrections using the metric in equation 7.10, with results shown in Figure 7.5.

## **7.6 Discussion and Conclusion**

Similar to the results for phantom data, the high frequency correction reduces the variability between the normal control scans. The reduction in variability (15% – 25%) is less than that in phantom studies (Figure 7.4). This was expected as normal subjects, unlike phantom studies, have inter-subject differences. Application of the low frequency correction, however, did not bring about a further decrease in variability thus indicating that the low frequency correction factors obtained from the phantom scans were not appropriate for the human scans.

There are two likely reasons for this result. First, human brains are ellipsoidal in shape while the Hoffman brain phantom on which the correction factors are based is cylindrical. Thus the correction factors based on a cylindrical phantom may well be inappropriate for a human brain scan. Second, human brain sizes are variable and hence a fixed pair of correction factors per scanner model applied to all the human scans was found to be insufficient. Thus, though the high frequency correction factors were found to reduce variability in the human data and are being used for all ADNI scans, more work is required for refining the approach for low frequency correction. The possible steps to attain improved low frequency correction factors are discussed in the final chapter detailing future work in this area (Section 8.2.5).

## Chapter 8

### Summary and Future directions

PET is used for clinical diagnosis and brain research and has been increasingly employed for drug development. The strength of PET is the high sensitivity to changes in *in vivo* pharmacology of biological systems. Success of a PET experiment depends on two primary aspects as we have seen in this thesis; accurate representation of the radiotracer distribution in tissue by the PET images and accurate extraction of pharmacological parameters from a dynamic series of PET images. This thesis contributes improved methods for both of these aspects of quantification.

Traditional PET pharmacological studies involve drawing arterial samples from the subject which can be a major impediment. It is not only invasive for the subjects but also involves substantial additional work, requiring measurement and correction of for the fraction of radiolabeled metabolites in the plasma samples as well as being an additional source of error. The other limitation of traditional PET is the ability to measure only a single aspect of the subjects' pharmacological status in isolation, which may be insufficient to fully characterize their neurological condition. This thesis attempts to extend the existing noninvasive reference region approaches developed for single tracer scans to multiple neuropharmacological PET studies; thus providing a richer spectrum of biological information and making better use of scanner time, while at the same time avoiding arterial sampling.

With an increase in the use of PET in multi-center research trails for studying the progression of neurological diseases and also in the pharmaceutical industry for performing clinical drug trails, the problem of inter-scanner variability has become more important. The quality of the conclusions drawn from these trials will depend on



minimizing this variability. In this thesis we have developed a framework for assessing and reducing the inter-scanner variability.

## 8.1 Summary of results achieved

Statistical noise in PET time-activity curves is a cause of bias in the popular Logan plot method for estimation of DVR. The PCA-based smoothing technique developed in this work (Chapter 3) improved the receptor estimates by reducing bias without increasing variance. In simulation studies, nearly all of the 10% bias observed for TACs with a DVR equal to 5 was removed by the PCA-based Logan plot approach. In addition, there was an accompanying improvement in precision (Figure 3.6).

The PCA-based Logan plot approach was found to be especially valuable in dual-measurement intervention studies (Chapter 4) where bias was reduced in both control and challenge experiments without an increase in variance, demonstrating the method's higher sensitivity and specificity (Figures 4.3 and 4.4) than the original Logan plot as well as the other methods attempting to remove this bias.

In chapters 5 and 6 we developed and validated two reference region based techniques (the extrapolation method and the simultaneous fitting method) for dual-tracer studies where tracers targeting two different pharmacological systems are injected during the same scan. The simulations in chapter 5 showed a bias for extrapolation method estimates, especially for the first tracer due to noise and limited duration of data prior to the injection of the second tracer. The simultaneous fitting method provided an improvement over the extrapolation method in terms of bias in the parameter estimates with a slight decrease in precision (Tables 5.3 and 5.4). For application of the dual-tracer methods in human data, adaptive smoothing of the dynamic PET data (section 6.4) reduced the bias and allowed generation of DVR images for both extrapolation and simultaneous fitting methods that were very close in quality to the 'gold standard' single-tracer images. Both dual-tracer approaches provided parameter estimates with inter-subject regions-of-interest means within  $\pm 10\%$  of those obtained from single-tracer scans without any appreciable increase in variance.

In chapter 7, we proposed correction methods having both high and low frequency components to reduce inter-scanner PET image variability in multi-center

trials. The high frequency and low frequency correction factors were obtained by comparing the Hoffman brain phantom scans to a digital representation of the phantom. The high frequency correction reduced the variability in the phantom scans by 20% – 50% and low frequency correction further reduced the variability by 10% -15%. When the correction factors based on phantom scans were applied to human data from 95 normal controls, the high frequency correction reduced variability by 15-25%. The application of low frequency correction factors, however, did not further reduce the variability but actually increased the variability by ~5%. It is likely that this lack of success in human scans is due to the cylindrical shape of the phantom used to determine the correction factors and insufficient simulation of factors such as out-of-field scatter as well as variable brain sizes and shapes.

Various aspects of the work in this thesis that need improvement or further investigation are discussed next.

## **8.2 Future directions**

### **8.2.1 Noninvasive studies in the absence of a reference region**

The move towards non-invasive reference region based approaches has been a motivation for this work. However, it must be noted that not all radiotracers developed have a brain region with negligible specific binding. In other words, there might be tracers with specific binding in all regions of the brain and hence no appropriate ‘reference region’ exists. There are ongoing efforts in the PET community to move towards noninvasive approaches in absence of an ideal reference region. One of the approaches proposed recently is the image-based measurement of the arterial plasma input function. In this approach, the radioactivity in the internal carotid artery within the image volume is used as a measure of input function (Sanabria-Bohórquez 2003). Exploration of methods along these lines is necessary to find noninvasive ways to analyze tracers that do not have usable reference regions.

## 8.2.2 Weighted PCA for bias reduction in Logan plots

The PCA approach proposed in this work for reduction of bias in graphical Logan analysis uses an integral number of the components for fitting the PET TACs. Figure 3.6 shows the bias variance trade-off based on the number of chosen principal components. This work can be extended to use fractional contributions from various components for fitting the TACs. Altering the contribution from the principal components can be used to trace a continuous bias-variance curve from PCA0 to PCA16 in Figure 3.6 thus allowing the possibility of constructing an improved estimator.

## 8.2.3 Improved weighting for reference region approaches

The weighting used for dual-tracer studies in this work was based on the traditional counting statistics model shown in equation 2.5. This model is based on the noise in the measured target region TACs but ignores the errors in the measurement of the reference region curve. Work on incorporating the errors in the input function for arterial sampling studies has been done in the past (Huesman 1984). It is important to incorporate the errors in the reference region measurements as well. Though the reference regions used in this work were relatively large (in excess of 500 voxels, > 5 ml), there might be cases where reference regions are small and errors in their measurements might introduce errors in the parameter estimates. A recent conference abstract (Normandin and Morris 2008) proposes the following modification to equation 2.5 for the normalized variance of at frame  $j$ :

$$\sigma_j^2 = \frac{y_i(T_j)e^{\lambda T_j}}{t_{end}^j - t_{start}^j} + R_l^2 \frac{y_r(T_j)}{n_r(t_{end}^j - t_{start}^j)}, \quad - 8.1$$

where,  $R_l$  is the transport parameter from the full reference tissue model,  $y_r(T_j)$  is the reference tissue curve and  $n_r$  is the number of pixels that are averaged to get the reference tissue curve  $y_r(T_j)$ . The incorporation of this approach might significantly improve for parameter estimation in tracers with small reference regions.

## 8.2.4 Further improvement of dual-tracer studies

Dual-tracer PET studies can provide information on two different pharmacological systems and have been shown in this thesis to give results very close in overall quality to single tracer PET studies. However, the protocol may be further improved by performing the following studies:

### 1. **Optimal dose split:**

Due to count rate limitations of the scanner and the total radiation dose limit in human subjects, we are restricted in the total number of mCi that can be administered. The studies reported in this work used a protocol where the injected dose was split equally between the two tracers. The present work can be extended by performing optimization studies to determine the optimal split of the total dose between the two tracers to achieve the lowest bias and variance for any given tracer combination. This has been done for arterial sampling approach and was found to be ~50:50 (Koeppel et al. 2001), but the optimal dose may be different for the reference region approach.

### 2. **Tracers with different half lives:**

Both tracers used in this work were labeled with  $^{11}\text{C}$ . Dual-tracer simulation studies of radioisotopes with longer half lives (e.g.,  $^{18}\text{F}$ ) as well as studies with a combination of short and long half life tracers might be useful in further exploring the applicability of the methods proposed here.

The dual-tracer signal from tracers with the same half life can be corrected for decay (See Figure 6.1 and 6.2). However, decay correction is not possible for the dual-tracer signal from tracers with different half lives, since a global correction factor can no longer be applied. Instead, incorporation of the decay constant of each radiotracer into the compartmental model itself will be required (similar to that in (Huang et al. 1982)).

It must be noted that though  $^{18}\text{F}$  tracers might be expected to contribute a smaller noise component to the total dual-tracer signal, the longer half life would limit the injected activity of the  $^{18}\text{F}$  tracer, thus potentially nullifying the advantage of longer half life.

Another aspect needing investigation is the order of injection for tracers with different half lives. The extrapolation method might be a good analysis method for studies where the  $^{11}\text{C}$  tracer is injected first, as higher initial activity is possible due to the shorter half life, thus allowing for better statistics early in the scan. Furthermore, the contribution of the faster decaying  $^{11}\text{C}$  tracer to the total dual-tracer signal decreases over-time thus allowing more accurate extraction of the  $^{18}\text{F}$  curve.

If, however, the  $^{18}\text{F}$  tracer is injected first, the dual-tracer signal will have significant contributions from both tracers following the second injection due to the slow decay of  $^{18}\text{F}$  and the higher injected activity of  $^{11}\text{C}$ . This approach would most likely necessitate the employment of the simultaneous fitting method. Furthermore, this injection order may have the added advantage of allowing the model parameters for both tracers to be estimated from a range of data that has a greater temporal overlap.

## **8.2.5 Improvements in low frequency correction for inter-scanner variability reduction**

### **1. Human-like phantom based correction factors:**

A likely cause for the lack of success in applying Hoffman brain phantom-derived low frequency correction factors in chapter 7 is the cylindrical shape of the phantom (with no skull or neck) which is very different from the ellipsoidal shape of the human brain, which is connected to the rest of the body. Since the low frequency correction factors minimize the residual scatter and attenuation, both of which are geometry dependent phenomena, a more realistic humanoid phantom would allow a better choice for obtaining improved correction factors. At the same time, a more realistic torso phantom should also be used to simulate the out-of-field scatter.

### **2. Adaptation of correction factors to individual brain sizes:**

The inter-subject variability in humans includes differences in brain sizes as well as anatomical aspects of the brain. Since brain sizes are different for different subjects, the extent of attenuation and scatter is also different. Thus, application of the

same phantom-derived correction factors to all the human scans from a particular scanner model is not optimal. Simulation studies need to be performed to study the effect of brain size on the correction factors, with the goal of developing individualized correction factors.

## References

- Barber DC. (1980) The use of principal components in the quantitative analysis of gamma camera dynamic studies. *Phys. Med. Biol.* 25:283-292.
- Black NF, McJames S, Rust TC, Kadrmas DJ. (2008) Evaluation of rapid dual-tracer (62)Cu-PTSM + (62)Cu-ATSM PET in dogs with spontaneously occurring tumors. *Phys Med Biol* 53:217-232
- Carson RE. (1986) Parameter estimation in positron emission tomography. In: *Positron Emission Tomography and Autoradiography: Principles and Applications for Brain and Heart* (Phelps M, Mazziotta J, Schelbert H, eds), New York: Raven Press, p 347–390
- Comtat C, Kinihan PE, Defrise M, Michel C, Townsend DW. (1998) Fast reconstruction of 3D data with accurate statistical modeling. *IEEE Trans Nuc Sci* 45:1083-1089
- Cunningham VJ, Hume SP, Price GR, Ahier RG, Cremer JE, Jones AK. (1991) Compartmental analysis of diprenorphine binding to opiate receptors in the rat in vivo and its comparison with equilibrium data in vitro. *J Cereb Blood Flow Metab* 11:1-9
- Defrise M, Kinihan PE, Townsend DW, Michel C, Sibomana M, DF. N. (1997) Exact and approximate rebinning algorithms for 3-D PET data. *IEEE Trans Med Imaging* 16:145-158
- Endres CJ, Bencherif B, Hilton J, Madar I, Frost JJ. (2003) Quantification of brain mu-opioid receptors with [11C]carfentanil: reference-tissue methods. *Nucl Med Biol* 30:177-186
- Faraway J. (2004a) Principal Components. In: *Linear Models with R*: CRC Press, pp 131-137
- Faraway J. (2004b) Weighted Least Squares. In: *Linear Models with R*: CRC Press, pp 92-94
- Farde L, Eriksson L, Blomquist G, Halldin C. (1989) Kinetic analysis of central [11C]raclopride binding to D2-dopamine receptors studied by PET--a comparison to the equilibrium analysis. *J Cereb Blood Flow Metab* 9:696-708
- Feng D, Huang SC, Wang Z, Ho D. (1996) An unbiased parametric imaging algorithm for nonuniformly sampled biomedical system parameter estimation. *IEEE Trans. Med. Imag.* 15:512-518
- Fessler JA. (1995) ASPIRE 3.0 user's guide: A sparse iterative reconstruction library. In: *Technical Report 293*: Comm. and Sign. Proc. Lab., Dept. of EECS, Univ. of Michigan, Ann Arbor, MI, 48109-2122
- Herholz K, Lercher M, Wienhard K, Bauer B, Lenz O, Heiss WD. (2001) PET measurement of cerebral acetylcholine esterase activity without blood sampling. *Eur J Nucl Med* 28:472-477
- Hoffman EJ, Cutler PD, Digby WM, Mazziotta JC. (1990) 3-D phantom to simulate cerebral blood flow and metabolic images for PET. *IEEE Trans Nuc Sci* 37:616-620
- Holthoff VA, Koeppe RA, Frey KA, Paradise AH, Kuhl DE. (1991) Differentiation of radioligand delivery and binding in the brain: validation of a two-compartment model for [11C]flumazenil. *J Cereb Blood Flow Metab* 11:745-752

- Huang SC, Carson RE, Hoffman EJ, Kuhl DE, Phelps ME. (1982) An investigation of a double-tracer technique for positron computerized tomography. *J. Nucl. Med.* 23:816-822
- Huang SC, Phelps ME, Hoffman EJ, Sideris K, Selin CJ, Kuhl DE. (1980) Noninvasive determination of local cerebral metabolic rate of glucose in man. *Am J Physiol* 238:E69-82
- Hudson HM, Larkin RS. (1994) Accelerated image reconstruction using ordered subsets of projection data. *IEEE Trans Med Imaging* 13:601-609
- Huesman RH. (1984) A new fast algorithm for the evaluation of regions of interest and statistical uncertainty in computed tomography. *Phys Med Biol* 29:543-552
- Ichise M, Toyama H, Innis RB, Carson RE. (2002) Strategies to improve neuroreceptor parameter estimation by linear regression analysis. *J Cereb Blood Flow Metab* 22:1271-1281
- Innis RB, Cunningham VJ, Delforge J, Fujita M, Gjedde A, Gunn RN, Holden J, Houle S, Huang SC, Ichise M, Iida H, Ito H, Kimura Y, Koeppe RA, Knudsen GM, Knuuti J, Lammertsma AA, Laruelle M, Logan J, Maguire RP, Mintun MA, Morris ED, Parsey R, Price JC, Slifstein M, Sossi V, Suhara T, Votaw JR, Wong DF, Carson RE. (2007) Consensus nomenclature for in vivo imaging of reversibly binding radioligands. *J Cereb Blood Flow Metab* 27:1533-1539
- Joshi AD, Fessler JA, Koeppe RA. (2008a) Improving PET receptor binding estimates from Logan plots using principal component analysis. *J Cereb Blood Flow Metab* 28:852-865
- Joshi AD, Koeppe RA, Fessler JA. (2008b) Signal separation and parameter estimation in dual-tracer PET scans using reference region approaches I: Theory and simulations. (submitted to *J Cereb. Blood Flow and Metab.*)
- Joshi AD, Koeppe RA, Fessler JA, Kilbourn MK. (2008c) Signal separation and parameter estimation in dual-tracer PET scans using reference region approaches II: Human Studies. (submitted to *J Cereb. Blood Flow and Metab*)
- Kadrmas DJ, Rust TC. (2005) Feasibility of rapid multitracer PET tumor imaging. *IEEE Trans. Nucl. Imag.* 52:1341-1347
- Koeppe RA, Frey KA, Kuhl DE, Kilbourn MR. (1999a) Assessment of extrastriatal vesicular monoamine transporter binding site density using stereoisomers of [11C]dihydrotetrabenazine. *J Cereb Blood Flow Metab* 19:1376-1384
- Koeppe RA, Frey KA, Kume A, Albin R, Kilbourn MR, Kuhl DE. (1997) Equilibrium versus compartmental analysis for assessment of the vesicular monoamine transporter using (+)-alpha-[11C]dihydrotetrabenazine (DTBZ) and positron emission tomography. *J Cereb Blood Flow Metab* 17:919-931
- Koeppe RA, Frey KA, Snyder SE, Meyer P, Kilbourn MR, Kuhl DE. (1999b) Kinetic modeling of N-[11C]methylpiperidin-4-yl propionate: alternatives for analysis of an irreversible positron emission tomography trace for measurement of acetylcholinesterase activity in human brain. *J Cereb Blood Flow Metab* 19:1150-1163
- Koeppe RA, Frey KA, Vander Borgh TM, Karlamangla A, Jewett DM, Lee LC, Kilbourn MR, Kuhl DE. (1996) Kinetic evaluation of [11C]dihydrotetrabenazine by dynamic PET: measurement of vesicular monoamine transporter. *J Cereb Blood Flow Metab* 16:1288-1299



- Koeppel RA, Holthoff VA, Frey KA, Kilbourn MR, Kuhl DE. (1991) Compartmental analysis of [<sup>11</sup>C]flumazenil kinetics for the estimation of ligand transport rate and receptor distribution using positron emission tomography. *J Cereb Blood Flow Metab* 11:735-744
- Koeppel RA, Joshi A, Frey K, Snyder SE, Kilbourn MR, Fessler J. (2004) Dual-Tracer PET Studies without Arterial Sampling. *NeuroImage* 22:T115-T116
- Koeppel RA, Raffel DM, Snyder SE, Ficaro EP, Kilbourn MR, Kuhl DE. (2001) Dual-<sup>11</sup>C tracer single-acquisition positron emission tomography studies. *J. Cereb. Blood Flow Metab.* 21:1480-1492
- Lammertsma AA, Bench CJ, Hume SP, Osman S, Gunn K, Brooks DJ, Frackowiak RS. (1996) Comparison of methods for analysis of clinical [<sup>11</sup>C]raclopride studies. *J Cereb Blood Flow Metab* 16:42-52
- Lammertsma AA, Hume SP. (1996) Simplified reference tissue model for PET receptor studies. *Neuroimage* 4:153-158
- Logan J, Fowler JS, Volkow ND, Ding YS, Wang GJ, Alexoff DL. (2001) A strategy for removing the bias in the graphical analysis method. *J Cereb Blood Flow Metab* 21:307-320
- Logan J, Fowler JS, Volkow ND, Wang GJ, Ding YS, Alexoff DL. (1996) Distribution volume ratios without blood sampling from graphical analysis of PET data. *J Cereb Blood Flow Metab* 16:834-840
- Logan J, Fowler JS, Volkow ND, Wolf AP, Dewey SL, Schlyer DJ, MacGregor RR, Hitzemann R, Bendriem B, Gatley SJ, et al. (1990) Graphical analysis of reversible radioligand binding from time-activity measurements applied to [<sup>11</sup>C-methyl]-(-)-cocaine PET studies in human subjects. *J Cereb Blood Flow Metab* 10:740-747
- Minoshima S, Koeppel RA, Frey KA, Kuhl DE. (1994) Anatomical standardization: Linear scaling and nonlinear warping of functional brain images. *J Nucl Med* 35:1528-1537
- Minoshima S, Koeppel RA, Mintun MA, Berger KL, Taylor SS, Frey KA, Kuhl DE. (1993) Automated detection of the intercommissural (AC-PC) line for stereotactic localization of functional brain images. *J Nucl Med* 34:322-329
- Mintun MA, Raichle ME, Kilbourn MR, Wooten GF, Welch MJ. (1984) A quantitative model for the in vivo assessment of drug binding sites with positron emission tomography. *Ann Neurol* 15:217-227
- Mueller SG, Weiner MW, Thal LJ, Petersen RC, Jack C, Jagust W, Trojanowski JQ, Toga AW, Beckett L. (2005) The Alzheimer's disease neuroimaging initiative. *Neuroimaging Clin N Am* 15:869-877, xi-xii
- Nagatsuka S, Fukushi K, Shinotoh H, Namba H, Iyo M, Tanaka N, Aotsuka A, Ota T, Tanada S, Irie T. (2001) Kinetic analysis of [(11)C]MP4A using a high-radioactivity brain region that represents an integrated input function for measurement of cerebral acetylcholinesterase activity without arterial blood sampling. *J Cereb Blood Flow Metab* 21:1354-1366
- Normandin MD, Morris ED. (2008) Improved performance of the simplified reference tissue model with a new residual weighting approach. In: *Neuroreceptor Mapping 2008*, p Page T76

- Ogden RT. (2003) Estimation of kinetic parameters in graphical analysis of PET imaging data. *Stat Med* 22:3557-3568
- Pedersen F, Bergström M, Bengtsson E, Långström B. (1994) Principal component analysis of dynamic positron emission tomography images. *Eur. J. Nucl. Med.* 21:1285–1292
- Razifar P, Axelsson J, Schneider H, Långström B, Bengtsson E, Bergström M. (2006) A new application of pre-normalized principal component analysis for improvement of image quality and clinical diagnosis in human brain PET studies—Clinical brain studies using [<sup>11</sup>C]-GR205171, [<sup>11</sup>C]-L-deuterium-deprenyl, [<sup>11</sup>C]-5-Hydroxy-L-Tryptophan, [<sup>11</sup>C]-L-DOPA and Pittsburgh Compound-B. *NeuroImage* 33:588–598
- Rust TC, Kadrmas DJ. (2006) Rapid dual-tracer PTSM+ATSM PET imaging of tumour blood flow and hypoxia: a simulation study. *Phys Med Biol* 51:61-75
- Sanabria-Bohórquez S. (2003) Image-Derived Input Function for [<sup>11</sup>C]Flumazenil Kinetic Analysis in Human Brain. *Molecular Imaging & Biology* 5:72-78
- Sitek A, Di Bella EVR, Gullberg GT. (1999) Factor Analysis of Dynamic Structures in Dynamic SPECT Imaging Using Maximum Entropy. *Trans. Nucl. Sci* 46:2227-2232
- Slifstein M, Laruelle M. (2000) Effects of statistical noise on graphic analysis of PET neuroreceptor studies. *J Nucl Med* 41: 2083-2088
- Talairach J, Tournoux P. (1988) *Co-planar Stereotaxic Atlas of the Human Brain: 3-Dimensional Proportional System - an Approach to Cerebral Imaging*. New York, NY: Thieme Medical Publishers
- Thireou T, Strauss LG, Dimitrakopoulou-Strauss A, Kontaxakis G, Pavlopoulos S, Santos A. (2003) Performance evaluation of principal component analysis in dynamic FDG-PET studies of recurrent colorectal cancer. *Comput Med Imaging Graph.* 27:43-51
- Varga JZ, Szabo Z. (2002) Modified regression model for the Logan plot. *J Cereb Blood Flow Metab* 22: 240-244